INVESTIGATION OF KEY-HOLE WELDABILITY OF LINE PIPE STEEL
GRADE X70M IN TERMS OF FRACTURE TOUGHNESS

A THESIS SUBMITTED TO
THE GRADUATE SCHOOL OF NATURAL AND APPLIED SCIENCES
OF
MIDDLE EAST TECHNICAL UNIVERSITY

BY

MEHMET ÇAĞIRICI

IN PARTIAL FULFILLMENT OF THE REQUIREMENTS
FOR
THE DEGREE OF MASTER OF SCIENCE
IN
METALLURGICAL AND MATERIALS ENGINEERING

JUNE 2017

Approval of the thesis

INVESTIGATION OF KEY-HOLE WELDABILITY OF LINE PIPE STEEL GRADE X70M IN TERMS OF FRACTURE TOUGHNESS

Submitted by **MEHMET ÇAĞIRICI** in partial fulfilment of the requirements for the degree of **Master of Science in Metallurgical and Materials Engineering Department, Middle East Technical University** by

Prof. Dr. Gülbin Dural Ünver
Dean, Graduate School of **Natural and Applied Sciences**　　　_____

Prof. Dr. C. Hakan Gür
Head of Department, **Metallurgical and Materials Eng.**　　　_____

Prof. Dr. C. Hakan Gür
Supervisor, **Metallurgical and Materials Eng. Dept., METU**　　　_____

Dr. Koray Yurtışık
Co-Supervisor, **Weld. Tech. and NDT Res./App. C., METU**　　　_____

Examining Committee Members

Prof. Dr. Cevdet Kaynak
Metallurgical and Materials Eng. Dept., METU　　　_____

Prof. Dr. C. Hakan Gür
Metallurgical and Materials Eng. Dept., METU　　　_____

Assist. Prof. Dr. Mert Efe
Metallurgical and Materials Eng. Dept., METU　　　_____

Assist. Prof. Dr. Sezer Özerinç
Mechanical Eng. Dept., METU　　　_____

Assist. Prof. Dr. Caner Şimşir
Manufacturing Eng. Dept., Atılım University　　　_____

DATE: 21/06/2017

I hereby declare that all information in this document has been obtained and presented in accordance with academic rules and ethical conduct. I also declare that, as required by these rules and conduct, I have fully cited and referenced all material and results that are not original to this work.

Name, Last Name: Mehmet Çağırıcı

Signature:

ABSTRACT

INVESTIGATION OF KEY-HOLE WELDABILITY OF LINE PIPE STEEL GRADE X70M IN TERMS OF FRACTURE TOUGHNESS

Çağırıcı, Mehmet

M. Sc., Department of Metallurgical and Materials Engineering
Supervisor: Prof. Dr. C. Hakan Gür
Co-Supervisor: Dr. Koray Yurtışık

June 2017, 132 Pages

Micro-alloyed and thermomechanically rolled HSLA line pipe steels promise optimum strength and toughness. Their microstructure contains generally globular and acicular ferrite. However, the heat induced by welding during line pipe fabrication alters the microstructure at the proximity of the fusion zone which affects indirectly microstructure of the heat affected zone, consequently the fracture toughness, is governed by the chemistry of the material and the thermal cycles during the welding process. In fabrication generally submerged arc welding (SAW) is applied. The hybrid plasma arc welding (HPAW) might save filler consumption and reduce the heat input of the process. The purpose of this work is to investigate weldability of X70M by using the key-hole based hybrid welding process by focusing on fracture toughness.

Keywords: *Hybrid plasma arc welding; Gas metal arc welding; Submerged arc welding; Keyhole welding; X70M; High strength low alloy steels; Crack tip opening displacement*

ÖZ

X70M SINIFI BORU HATTI ÇELİKLERİNİN ANAHTAR DELİĞİ METODU İLE KAYNAKLANABİLİRLİĞİNİN KIRILMA TOKLUĞU YÖNÜNDEN İNCELENMESİ

Çağırıcı, Mehmet

Yüksek Lisans, Metalurji ve Malzeme Mühendisliği Bölümü
Tez Yöneticisi: Prof. Dr. C. Hakan Gür
Yardımcı Tez Yöneticisi: Dr. Koray Yurtışık

Haziran 2017, 132 Sayfa

Mikro alaşımlanmış ve termomekanik haddelenmiş yüksek dayançlı düşük alaşımlı boru hattı çelikleri optimum dayanç ve tokluk değerlerini kendilerine has mikroyapısal bileşenleri sayesinde karşılamaktadır. Kaynaklı üretim aşamasında kaçınılmaz bir etkisi olan ısı girdisi parça üzerinde oluşan erime bölgesindeki mikroyapısal farklılaşmalara dolaylı olarak etki etmektedir. Bu farklılaşmalara ek olarak, malzemenin kırılma tokluğu değerleri temelde malzemenin kimyasal yapısı ve kaynaklı üretim aşamasındaki ısıl süreçlere bağlı olarak değişmektedir. Boru hatlarının üretiminde genellikle tozaltı kaynağı tercih edilmektedir. Ancak henüz yaygınlaşmamış bir metod olan hibrit plazma ark kaynağı üretim aşamasında sağlayabildiği dolgu malzemesi tasarrufu ve toplam ısı girdisi düşüşü etkenler dolayısıyla tozaltı kaynağının yerine önerilebilir. Bu tezin amacı X70M boru hattı çeliklerinin belirtilen yollarla kaynaklanabilirliğinin malzemenin kırılma tokluğu özelliklerinin üzerindeki etkisini ortaya çıkarabilmektir.

Anahtar Kelimeler: Hibrit plazma ark kaynağı; Gaz metal ark kaynağı; Tozaltı ark kaynağı Anahtar-deliği kaynağı; X70M; Yüksek dayançlı düşük alaşımlı çelik; çatlak ucu açılım deplasmanı testi.

To My Family;

ACKNOWLEDGEMENTS

TABLE OF CONTENTS

LIST OF TABLES

LIST OF FIGURES

xv

LIST OF SYMBOLS

A   Elongation

AF   Acicular Ferrite

γ Austenite

δ_c Critical CTOD Value

GB   Granular Bainite

MA   Martensite-austenite islands

PF   Polygonal Ferrite

$R_{p0.2}$ 0.2% offset yield stress (proof stress)

R_m Ultimate tensile strength

LIST OF ABBREVIATIONS

ASME   The American Society of Mechanical Engineers

ASTM   American Society for Testing and Materials

AWS   American Welding Society

BCC   Body Centered Cubic (lattice structure)

CCT   Continuous Cooling Transformation (diagram)

CE   Carbon Equivalent

CGHAZ   Coarse Grained Heat Affected Zone

CTOD   Crack Tip Opening Displacement

DIN   Deutsches Institut für Normung

EBW   Electron Beam Welding

EDS   Energy Dispersive Spectral Analysis

EDX   Energy Dispersive X-ray Analysis

EPFM   Elastic Plastic Fracture Mechanics

FCAW   Flux Cored Arc Welding

FCG   Fatigue Crack Growth

FCC   Face Centred Cubic (lattice structure)

FGHAZ   Fine Grained Heat Affected Zone

FZ   Fusion Zone (weld metal)

GMAW   Gas Metal Arc Welding

GTAW   Gas Tungsten Arc Welding

GA   Genetic Algorithm

HAZ   Heat Affected Zone

HLAW	Hybrid Laser Arc Welding
HPAW	Hybrid Plasma-Gas Metal Arc Welding
HSLA	High Strength Low Alloy Steel
HV	Vickers Hardness
HVIT	Vickers Hardness Indentation Toughness
IIW	International Institute of Welding
IRCGHAZ	Intercritically Reheated Coarse Grain Heat Affected Zone
ISO	International Organization for Standardization
T_Z	Inter-pass Temperature
LEFM	Linear Elastic Fracture Mechanics
LWS	Linear Welding Speed
MAG	Metal Active Gas Welding
MIG	Metal Inert Gas Welding
PAW	Plasma Arc Welding
T_V	Pre-heating Temperature
PQR	Procedure Qualification Record
PWHT	Post Weld Heat Treatment
SEM	Scanning Electron Microscope
TMCP	Thermomechanically Controlled Processes
TIG	Tungsten Inert Gas Welding
TTT	Time-temperature Transformation (diagram)
UTS	Ultimate Tensile Strength
WFS	Wire Feeding Speed
WPS	Welding Procedure Specification

xx

CHAPTER 1

INTRODUCTION

The energy demand increases day by day due to the population growth in the world. Although the need for clean and renewable energy has a great importance for environmental sustainability, high amount of fossil fuels are still used due to some inevitable industrial applications. Relatively, fossil fuels are transported by using high capacity equipment and techniques. The best way to transfer the fuel is pipelines due to economic and safety concerns.

The construction of the pipeline involves joining sections of spiral or line welded pipes with circumferential welds known as girth welds employing GMAW and FCAW techniques. The welding processes are a rate limiting step in pipeline construction. SAW is preferred technique during line pipe fabrication, whereas GMAW or FCAW are employed for girth welding in the field. These welding techniques are employed due to their high efficiency and high bridging capabilities. New welding techniques have been developed in the past decade to address this issue with regards to long pipeline construction projects. The application of tandem and multiple arc welding procedures have been advanced for evaluation as welding methods for some recent pipeline projects. The weldability of the steel should be improved with a new welding techniques.

API 5L X70M is one of the most favourable line pipe steel in construction projects, such as Trans Anatolian Pipeline Project, namely TANAP, is under construction using API 5L X70M (PSL2) in the main line. The steel has relatively superior properties compared to production costs of other high strength low alloy line pipe steels, i.e. X80 and X100. Its optimum mechanical properties are obtained due to improved fabrication techniques, i.e. thermomechanically controlled processes.

TMCP provides the formation of finer microstructural constituents, using small amount of micro-alloying elements, compared to conventional steel fabrications. The formed smaller acicular and polygonal ferrite yield high toughness values. Although the welding process cause a variations in fusion and heat-affected zone microstructure, the initial material properties are tried to be maintained using proper welding techniques. One of the relatively new welding method is hybrid plasma arc welding. HPAW is used for only key-hole based welding processes, due to its narrow and deep penetration characteristics [1]. The method yields better weldability with lower operational cost compared to conventional GMAW and FCAW.

Conventional welding fabrication codes specify maximum tolerable flaw sizes and minimum tolerable Charpy energy, based on good workmanship, i.e. what can reasonably be expected within normal working practices. These requirements tend to be somewhat arbitrary, and failure to achieve them does not necessarily mean that the structure is at risk of failure. The failure risk might be limited and eliminated by determining the material behavior under certain circumstances. The material toughness affects the behavior primarily and it is used to benchmark the applicable fabrication and construction welding methods. The suitable fracture toughness measurement methods for X70M grade steel path dependent crack tip opening displacement and path independent J-integral due to the steel obeys elastic-plastic fracture mechanics approach.

The toughness behavior of the material varies due to the differences in material and processes. The welding processes are mainly affect the microstructural variations in FZ and HAZ. The complex structure in HAZ downgrades the toughness of the line pipe steels [2]. The lowest toughness values are obtained due to the local hardened points, which are determined according to weakest link models [3]. The retained austenite based morphologies, such as martensite-austenite islands, caused the detrimental effect on the desired mechanical properties [4].

2

The aim of this study, is to investigate key-hole weldability of X70M in terms of fracture toughness and to analyse the reasons behind toughness variations on the basis of physical and mechanical metallurgy. The hypothesis is based on the investigation of effects of six phenomena,

- Welding techniques, SAW, GMAW, and HPAW,
- Welding parameters, such as weld bevel design and applied power,
- Single- and multi-pass welding,
- Chemical composition of filler metals,
- Coupon thickness, and
- Local weakest points, such as MA formations in IRCGHAZ.

CHAPTER 2

THEORY

2.1. General

Theory chapter is divided into 4 main sections. Firstly, brief overview on pipelines and their common properties are given. Secondly, the properties of API 5L X70M steel and its production road are mentioned in detail. Thirdly, the fabrication route of line pipe steels and the effects of each different processes on material properties are discussed. Finally, the basis of this thesis, fracture toughness properties in accordance with common fracture mechanic approaches and applicable test method, CTOD, are stated.

2.2. Pipelines

The most of the fossil energy sources are transferred from one place to another by pipelines. Various kinds of line pipe materials are produced according to ASME, API, and ISO standards. The widely used line pipe materials are generally produced in accordance with API standards. The most popular one, API 5L [5] specifies requirements for production of welded and seamless steel pipes, which are mainly used in natural gas and petroleum industries. This specification consists of two kinds of production specification level (PSL) and various types of line pipe steels, with grades from X42 to X120M.

PSL 2 defines the mandatory minimum and maximum values for two material properties (notch toughness and carbon equivalent, CE), in addition to the minimum values of tensile strength, yield strength and notch toughness given in PSL 1. The other major difference between these specification levels is the type of pipe-ends.

The steels can be manufactured with belled-end, threaded-end and plain-end for PSL 1 or with only plain-ends for PSL 2 [6].

Table 1. Classification of line pipe steels according to API 5L [5].

PSL	Delivery Condition	Pipe Grade
PSL1	As-rolled, normalized, normalizing formed	A
	As-rolled, normalizing rolled, thermomechanical rolled, thermo-mechanical formed, normalizing formed, normalized, normalized and tempered or if agreed Q&T SMLS only	B
	As-rolled, normalizing rolled, thermomechanical rolled, thermo-mechanical formed, normalizing formed, normalized, normalized and tempered	X42, X46, X52, X56, X60, X65, X70
PSL 2	As-rolled	BR, X42R
	Normalizing rolled, normalizing formed, normalized or normalized and tempered	BN, X42N, X46N, X52N, X56N, X60N
	Quenched and tempered	BQ, X42Q, X46Q, X56Q, X60Q, X65Q, X70Q, X80Q, X90Q, X100Q
	Thermomechanical rolled or thermomechanical formed	BM, X42M, X46M, X56M, X60M, X65M, X70M, X80M
	Thermomechanical rolled	X90M, X100M, X120M
	The suffice (R, N, Q or M) for PSL2 grades, belongs to the steel grade	

In the designation of the steel grades, the digits after X symbol indicates the minimum yield strength in terms of ksi rounded down to the nearest integer, and the letter refers delivery condition. The letters R, N, Q, and M mean as-rolled, normalized, quenched and thermomechanically rolled in a given order. For instance,

API 5L X60N (PSL2) means that the steel is in the normalized condition, and has 60 ksi (415 MPa) yield strength.

In many pipeline projects thermomechanically rolled or formed line pipe steels are used due to their superior mechanical properties. All API 5L specified line pipe steels are listed in (Table 1).

General application of thermomechanical processes is based on sequential forming processes. Thermomechanical controlled process (TMCP) containing hot deformation and cooling rate, also plays an important role in microstructure formation. In addition to the alloying content, the technical parameters of TMCP such as soaking temperature, rolling temperature, finishing temperature, cooling rate and cooling interrupt temperature are significant for the final microstructure [7].

TMCP is a two-stage process (Figure 1) compared to the traditional hot rolling operation and, the time delay is introduced between roughing and finishing. This allows the finishing operations to be carried out at temperatures below the recrystallization temperature, which results in the formation of fine pancaked austenite grains and transformation to a fine-grained ferrite structure. The process is greatly facilitated by the addition of carbide-forming elements. In particular, it was shown that the addition of about 0.05% Nb causes a marked retardation in recrystallization which allows controlled rolling at significantly higher temperatures [8].
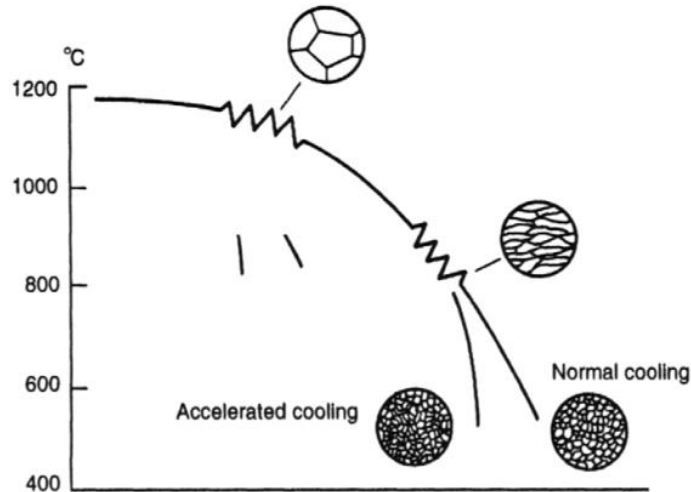
Figure 1. Schematic representation of thermomechanically controlled process (TMCP) [8].

The micro-alloying additions, when in solution, control the transformation of austenite to ferrite. Generally, micro-alloying elements increase the temperature where complete recrystallization occurs and retard the recrystallization of austenite below this temperature. The precipitate particles of these micro-alloying additions restrict the grain growth of austenite by retarding the grain boundary movement through pinning them. This leads to a highly deformed, fine austenite grain structure. Since the initial austenite grain size is smaller, the resulting ferrite grain structure after the γ to α transformation is finer. The typical TMC processes and their effects on the microstructure can be seen in (Figure 2 and Figure 3).
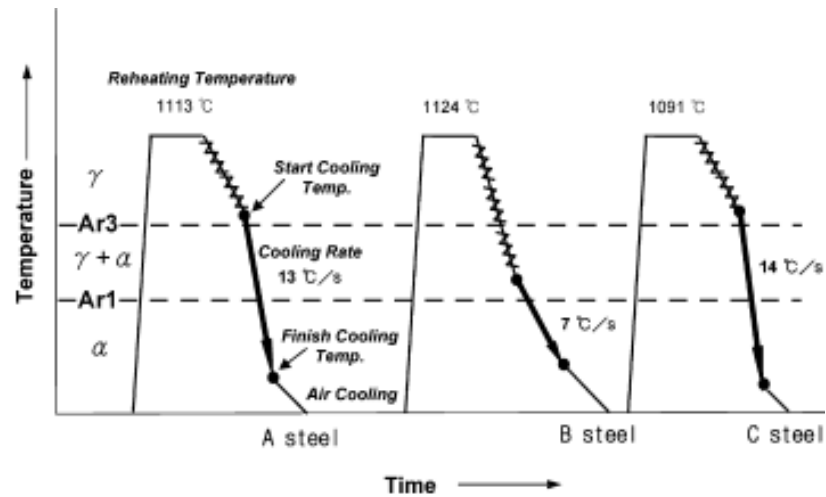
Figure 2. Different kinds of TMCP applications on API X70 and X80 grade line pipe steels [9]
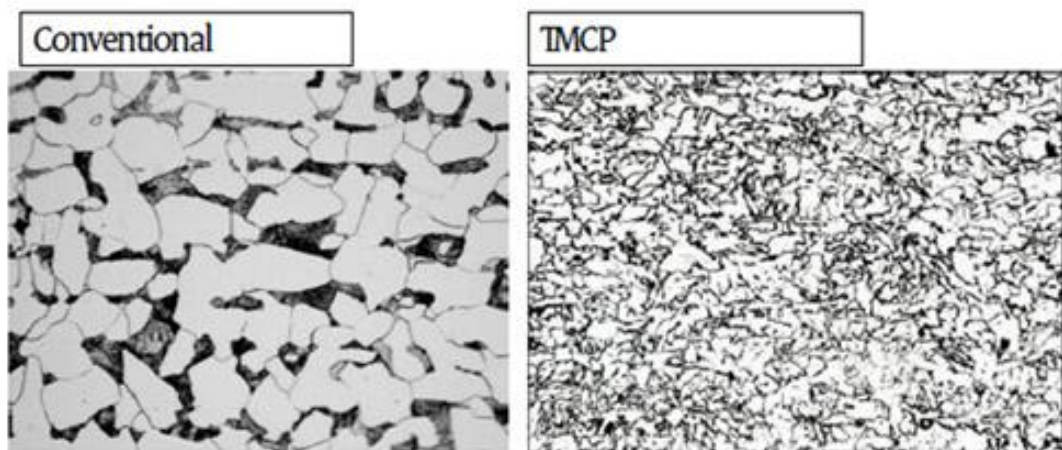
Figure 3. The effects of TMCP on morphological formations in microstructure [10]

Additional constituents cause variations in carbon equivalent. This term helps to indicate crack sustainability and material hardenability during welding. These constituents in small amounts will directly change the microstructure and mechanical properties of welded steels. The major micro-alloying elements are Nb, Ti and V. The effects of micro-alloying elements on steels are summarized in Table 2.

Table 2. Effects of micro-alloying elements [11].

Elements (Wt%)	Effect of Addition
C (0.03‾0.10)	• Matrix strengthening (by precipitation hardening)
Si (up to 0.6)	• Improvement in strength (by solid-solution hardening).
Mn (1.6‾2.0)	• Retard austenite decomposition in accelerated cooling process. • Matrix strengthening by substitutional solid-solution hardening. • Lowering DBTT. • Promoting fine grained lower bainite. • Higher Mn content cause centerline banding in hot-rolled steels.
Nb (0.03‾0.06)	• Retard recrystallization between rolling passes by reducing temperature range • Limiting austenite grain growth
Ni (0.2‾1.0)	• Improves low-temperature toughness without losing weldability of low-C steels • Eliminates undesired local brittle zone formations and increases toughness in contrast to Ni, Mg and Mo
Mo (0.2‾0.6)	• Improves hardenability and promotes lower bainite.
Ti (0.005‾0.030)	• Suppresses austenite grain growth by TiN formation. • Maintains hardenability by fixing free Ni • Strong ferrite strengthener.
V (0.03‾0.08)	• Matrix strengthening during tempering by precipitation hardening • Strong ferrite strengthener.

In order to increase the efficiency of the pipeline, the gas flow rate should be increased. This can be achieved by increasing the operating pressure and outside pipe diameter which necessitates the use of stronger materials. By increasing steel strength, the wall thickness, hence the overall weight, and the cost of the project can be reduced. However, if high strength accompanies with a decrease in toughness, the risk of reduction in crack propagation resistance and formability [12, 13]. The former may result in catastrophic failures, especially at low operating temperatures, whereas the latter makes the productivity complicated and difficult. Hence, the main aim is to acquire the combination of strength and toughness. The line pipe steels require high yield strength, low ductile to brittle transition temperature and sufficient absorption energy [14]. This requirement can be satisfied using HSLA or specifically produced, TMCP, line pipe steels. Although the minimum requirements to have HSLA steel are 275 MPa (40 ksi) yield strength, the line pipe steels could be named as HSLA after X70M and X80 grade due to the chemical composition limits given by ASM International [15]. Besides, both HSLA and TMC processed steels have good corrosion resistant performance beyond owning great mechanical properties. It can be possible when the alloying elements cause the formation of desired microstructural constituents, i.e. ferritic structure rather than pearlitic one.

2.3. The Material, API 5L X70M

API 5L X70M (PSL 2) is the primary option in pipeline construction due to its optimum cost-benefit ratio compared to other HSLA and PSL 2 line pipe steel. Thermomechanically forming and shaping processes give higher chance to compete with other common line pipe steels, such as API 5L X65 and X80 grade steels. Although these three grades have average mechanical properties to be used in off-shore and on-shore pipeline construction projects, API 5L X70M grade is widely used due to its availability advantage.

The mechanical properties of X70M grade line pipe steel are specified as 485 to 635 MPa yield strength, 570 to 760 MPa tensile strength and minimum 17% elongation

[5]. The chemical composition limits are given in Table 3 [5]. Chemical composition has a great effect on the desired mechanical properties by altering the microstructural features. Therefore, fraction of alloying elements may vary to meet the mechanical requirements.

Table 3 Chemical composition constraints of API 5L X70M grade line pipe steels [5]

	Mass Fraction (% maximum)								Carbon Equivalent (% maximum)	
	C	Si	Mn	P	S	V^1	Nb^1	Ti^1	Other[2,3]	CE_{IIW}	CE_{Pcm}
X70M	0.12	0.45	1.70	0.025	0.015					0.43	0.25

The strength of the micro-alloyed steels is increased dramatically by adding micro-alloying elements for grain refinement and/or precipitation strengthening. The main roles of important alloying elements are given in Table 2. Combination of alloying elements and processing method result in different microstructures, which usually consist of

- polygonal ferrite (PF),
- quasi-polygonal ferrite (QF) or massive ferrite,
- granular bainitic ferrite (GB or GF),
- bainitic of acicular ferrite (BF or AF)

[16, 17]. The microstructural constituents of the X70M steel can easily be visualized via the micrographs given in Figure 4, Figure 5, and Figure 6.

---

[1] Nb + V + Ti ≤ 0.15 %
[2,3] Cu, Ni, Cr, and Mo ≤ 0.50 %; B ≤ 0.001 %
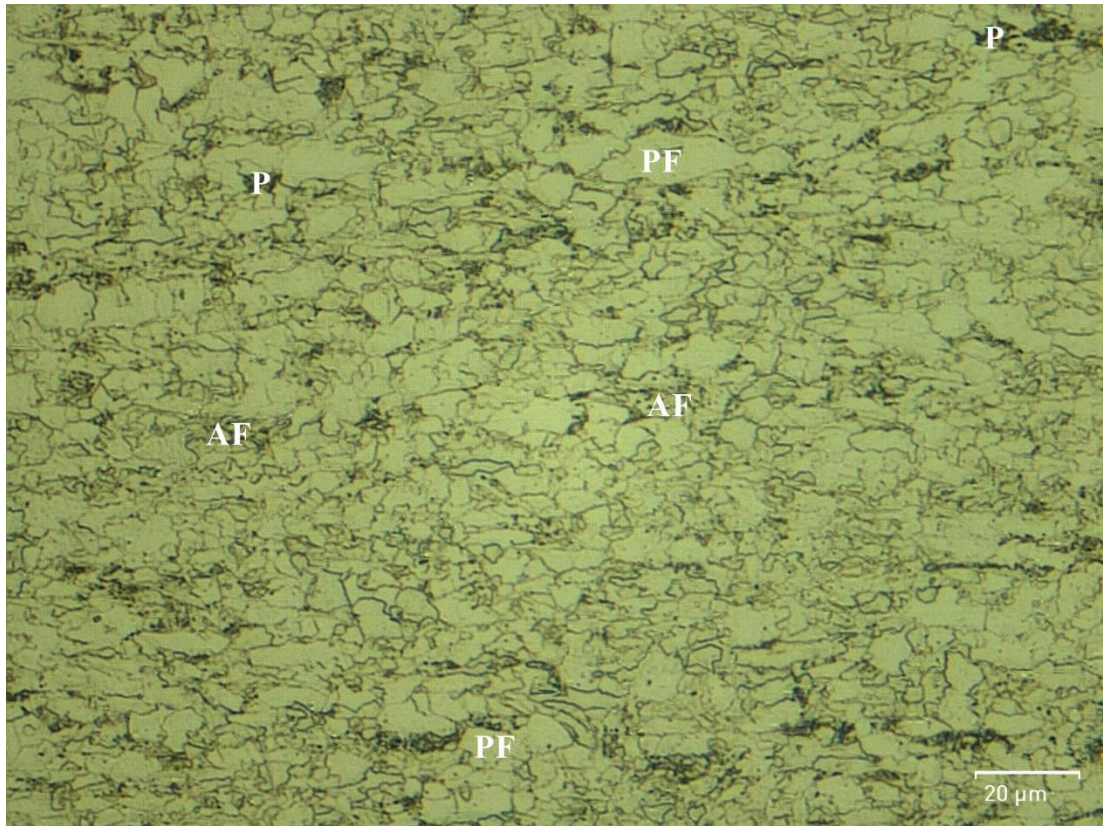
Figure 4. LOM micrographs of API X70M steel, consisting three different morphological formations. PF: polygonal ferrite, P: pearlite, AF: acicular ferrite.
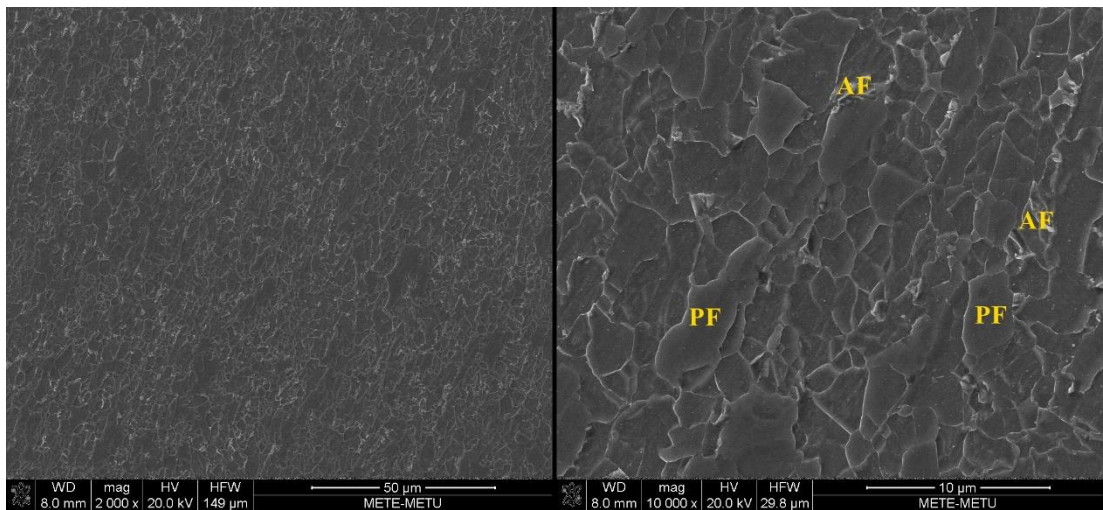
Figure 5. SEM micrographs of API X70M steel, consisting two different morphological formations. PF: polygonal ferrite, AF: acicular ferrite.
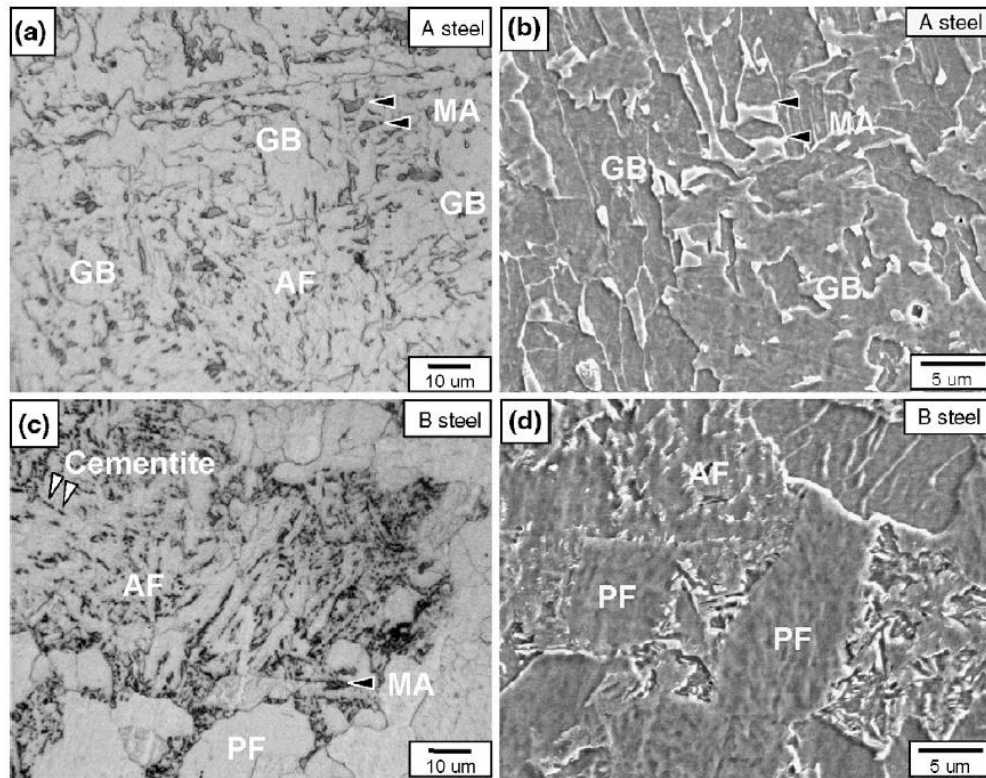
Figure 6. LOM and SEM micrographs of API X70 and X80 grade line pipe steels [17]. AF: acicular ferrite, GB: granular bainite, MA: martensite-austenite constituent, PF: polygonal ferrite, UB: upper bainite.

The high toughness and strength of the HSLA steels are due to acicular ferrite in the structure. By controlling the fineness and the amount of this phase during rolling the desired mechanical properties can be obtained. Shin et.al. [9] have worked over X70 and X80 steels with different chemical compositions and rolling conditions (Figure 3), namely A, B and C. Tensile and Charpy V-notch impact tests were performed between -196 and +20°C. The results are presented in (Table 4), together with chemical compositions and microstructural phases.

Table 4. Mechanical properties of variously processed (TMCP) API X70 and X80 grade line pipe materials in terms of their microstructures [12].

	C	Si	Mn	Ni + Mo	Microstructure	V	a	Y/U	USE	ETT	FAT
	Wt.%					%	μm		J	oC	
A	.06	.31	1.56	.20	AF, GB, (MA)	3	9	.81	244	-79	-90
B	.05	.30	1.56	.37	PF-AF, UB, (MA & cementite)	2	8	.81	194	-99	-101
C	.07	.23	1.76	.56	AF, UB, (MA)	5	6	.79	200	-97	-99
V	Volume fraction of second phases										
a	Effective grain size										
Y/U	Yield strength / tensile strength ratio										
USE	Upper shelf energy										
ETT	Energy transition temperature										
FAT	Fracture appearance transition temperature										

Kim et al. reported the tensile properties, upper shelf energy and ductile-to-brittle transition temperatures for four chemical compositions and three different rolling routes (Table 4) [14]. Hashemi et al. reported that the transition temperature of X70 steels is around -50°C with having upper shelf Charpy energies of 128, 145 and 222 J respectively for FZ, HAZ and base metal. They showed that BM and HAZ exhibit bainite and acicular ferrite structure with HAZ having various but coarser grain sizes, while FZ is composed of acicular and Widmanstatten ferrite [12].

In addition to S, high Mn and Si concentration makes the steel susceptible to HIC. HIC tests of X60 and X70 grades demonstrated that the zone at the thickness centre

has a high concentration of manganese, silicon, and sulphur, and cracks mostly nucleate around this zone [18]. However, it was also shown that the microstructure of the modern TMCP line pipe steels is the principal factor determining HIC resistance, where bainite and martensite are susceptible but AF is resistant[19].

Additional micro-alloying element, Nb, low carbon content and combining advantages of TMCP, weldability of X70M (PSL 2) grade line pipe steels may be considered to be good. The decrease in the amount of existing elements, except Fe, always increases the weldability. Therefore, X70M could be categorized as HSLA steel, and its lower alloying element content helps it to have good mechanical properties and weldability at the same time. The weldability of materials and their microstructural alterations mainly depends on the cooling rate. These variations could be determined via continuous cooling transition diagrams. The CCT diagram of X70M steel is given in Figure 7.
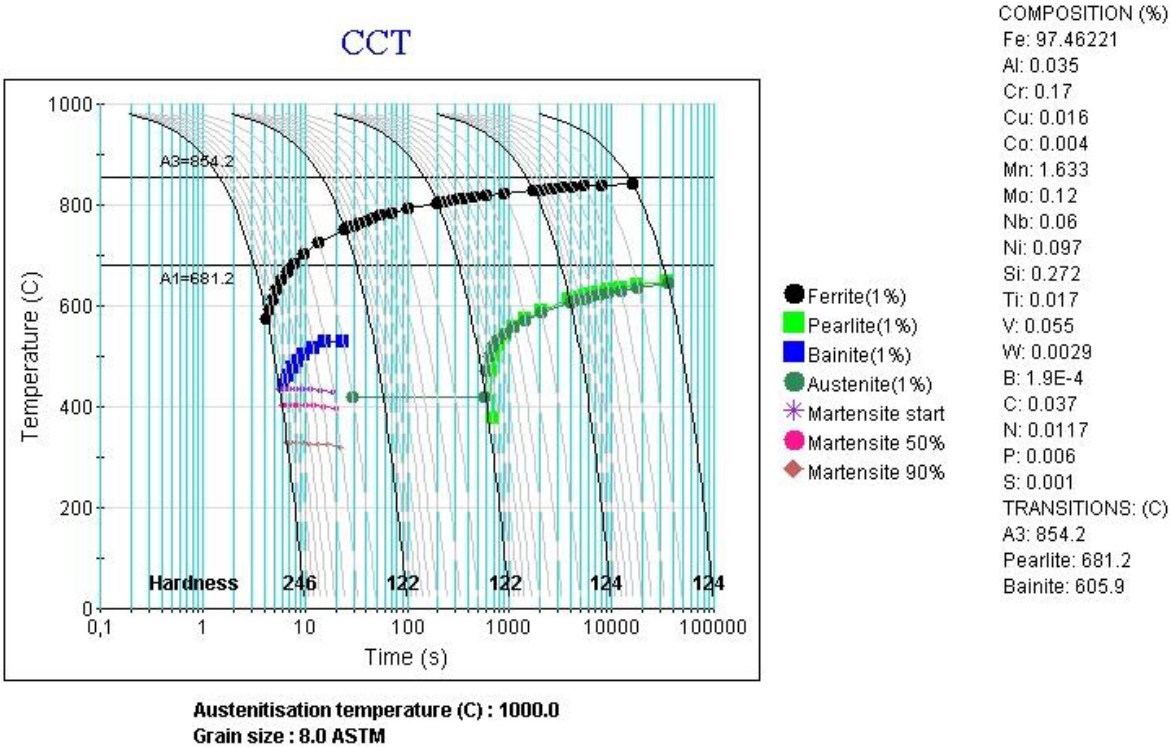
Figure 7. CCT of API 5L X70M, [20].

2.4. The Process, Fabrication of Line Pipe Steels

Fusion welding is an indispensable process during construction of the pipelines and usually fabrication of the line pipes. Seamless pipes are available for ordering; however, the welded steel pipes for the use of a large diameter pipeline in the transportation of petroleum and natural gas are generally preferred. As it can be seen in the Table 5, longitudinal or helical (spiral) sub-merged arc welding can be employed for fabrication of all types and grades of line pipes.

Table 5. Employed welding method in accordance with line pipe types.

Type of Pipe	PSL 1			PSL 2	
	Grade A	Grade B	X42 to X70	B to X80	X80 to X100
SMLS	✓	✓	✓	✓	✓
LFW	✓	✓	✓		
HFW	✓	✓	✓	✓	
LW			✓		
SAWL	✓	✓	✓	✓	✓
SAWH	✓	✓	✓	✓	✓

SMLS – Seamless, (without weld)

LFW – Low frequency welded pipe, <70 kHz

HFW – High frequency welded pipe, >70 kHz

SAWL – Submerged-arc welding (longitudinal weld)

SAWH - Submerged-arc welding (helical weld)

2.4.1. Fusion Welding, Energy Sources and Welding Zones

The fusion welding is a proper joining process for materials which have similar melting points and microstructures. The weld pool is formed by inducing heat to melt the parent materials. The heat sources can be a lame, a beam, an electric resistance and an arc.

Figure 8 represents temperature vs. distance profiles during string bead welding at a constant welding speeds. As the torch, the heat spot, moves from the initial welding points, the parent and molten metal starts to cool down to the pre-heat or room temperature rapidly. Hence, the obtained temperature gradients during fusion welding operations are higher compared to casting processes.

The fusion welding can be operated by using filler metal or conducted by melting the parent materials without any filler addition. In former case, the welding process must be designed according to parent metal and corresponding microstructure. The additive filler metal leads to dilution between parent and filler material. Consequently, the chemical composition differences between the parent and the filler material become significantly important. The microstructural features in FZ and HAZ are directly affected from this factor. In latter case, the welding is defined as autogenous. The applied heat melts the parent material and lead some thermal cycles to the adjacent regions of the FZ. The thermal cycles changes in accordance with the distance from the FZ and the heat source. The heat transfer conditions caused a microstructural alterations in the subjected materials. The heat transfer conditions can be determined according to the filler wire, the parent material and the concentration of heat input.
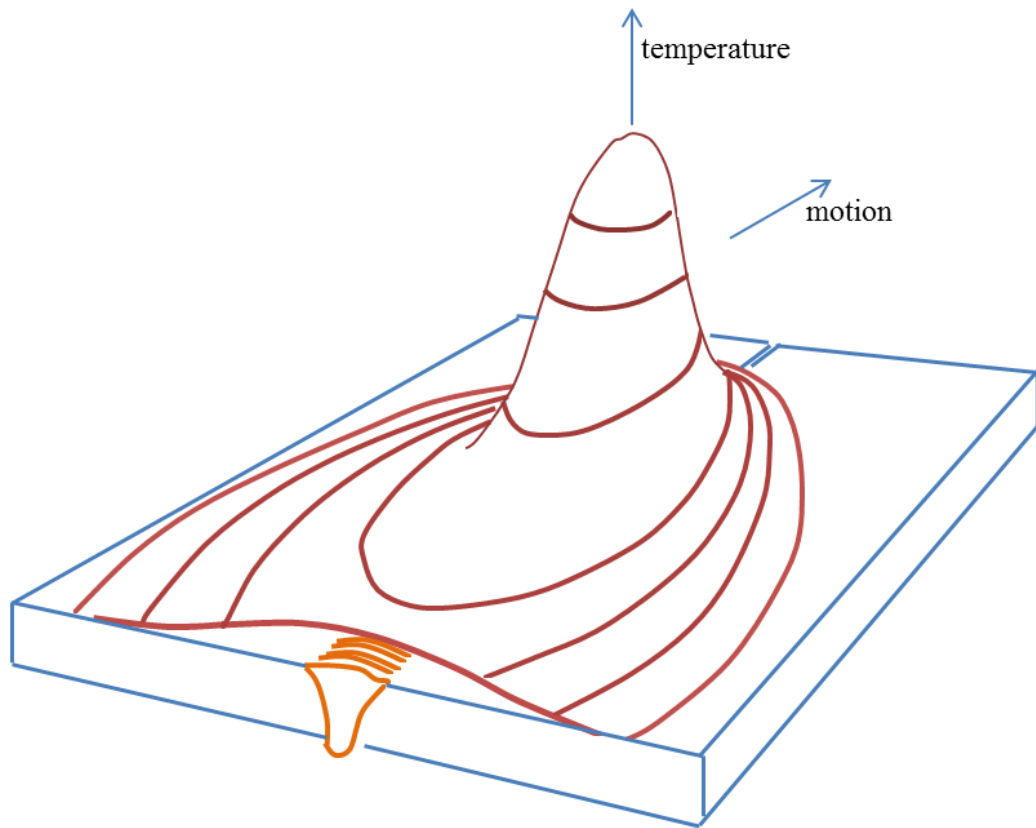
Figure 8. Schematic view of the fusion welding with temperature gradient profile [1].

Common microstructural features obtained by fusion welding are given in Figure 9. The regions that reaches a temperature, higher than the melting point of the material, is named as fusion zone. The crystals can exist with the molten metal in the thermodynamic equilibrium when the fusion line is subjected to heat that employs the melting temperatures. Actually, this thinner zone is named as partially melted zone (PMZ). Microstructure of the materials is altered within the HAZ because of the applied thermal cycles. The coarse grained microstructure is observed in the overheated or slowly cooled regions, adjacent to the fusion line. The grain size reduces along the parent metal, as the induced heat decreases, and the fine grained HAZ is subjected to normalization. The partial grain refinement exists in the zone, where temperature is below the melting temperature

International Organization for Standardization (ISO) defines weldability as: "Metallic material is considered to be susceptible to welding to an established extent with given processes and for given purposes when welding provides metal integrity by a corresponding technological process for welded parts to meet technical requirements as to their own qualities as well as to their influence on a structure they form."
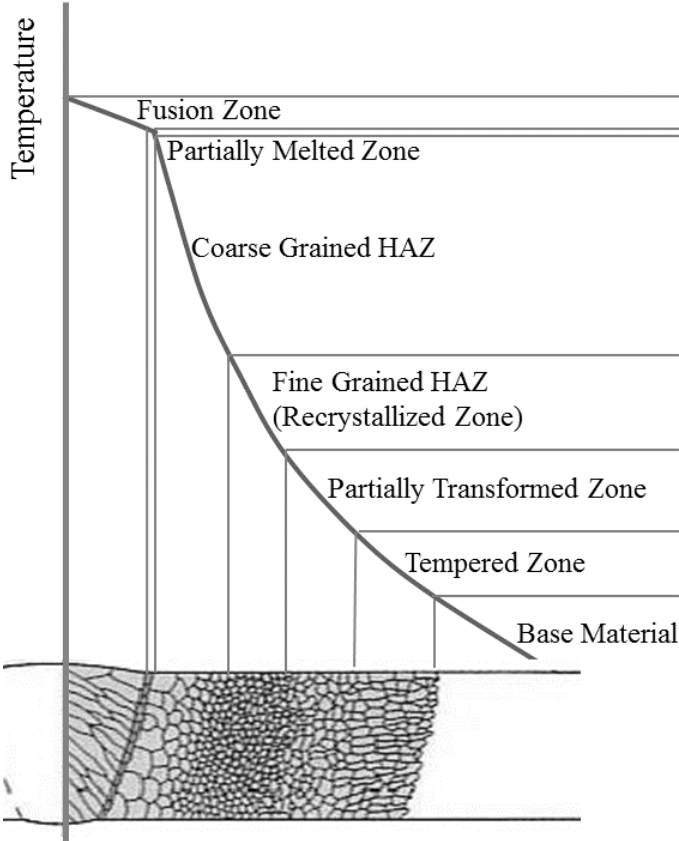
Figure 9. Microstructural variations between fusion zone and base material.

The weldability of the materials is influenced equally by four main factors, process, material, purpose, and design. The material based factors can be classified as; physical characteristics, microstructure and chemical composition. The chemical composition variations is typically responsible for the ageing, the hardenability and the convections in the weld pool. The microstructural features are responsible for grain formations, phase transformations and segregation within the fusion zone.

Mechanical and physical properties of the material, i.e. toughness, strength, and thermal expansion coefficient, have a significant role upon shaping the material characteristics.
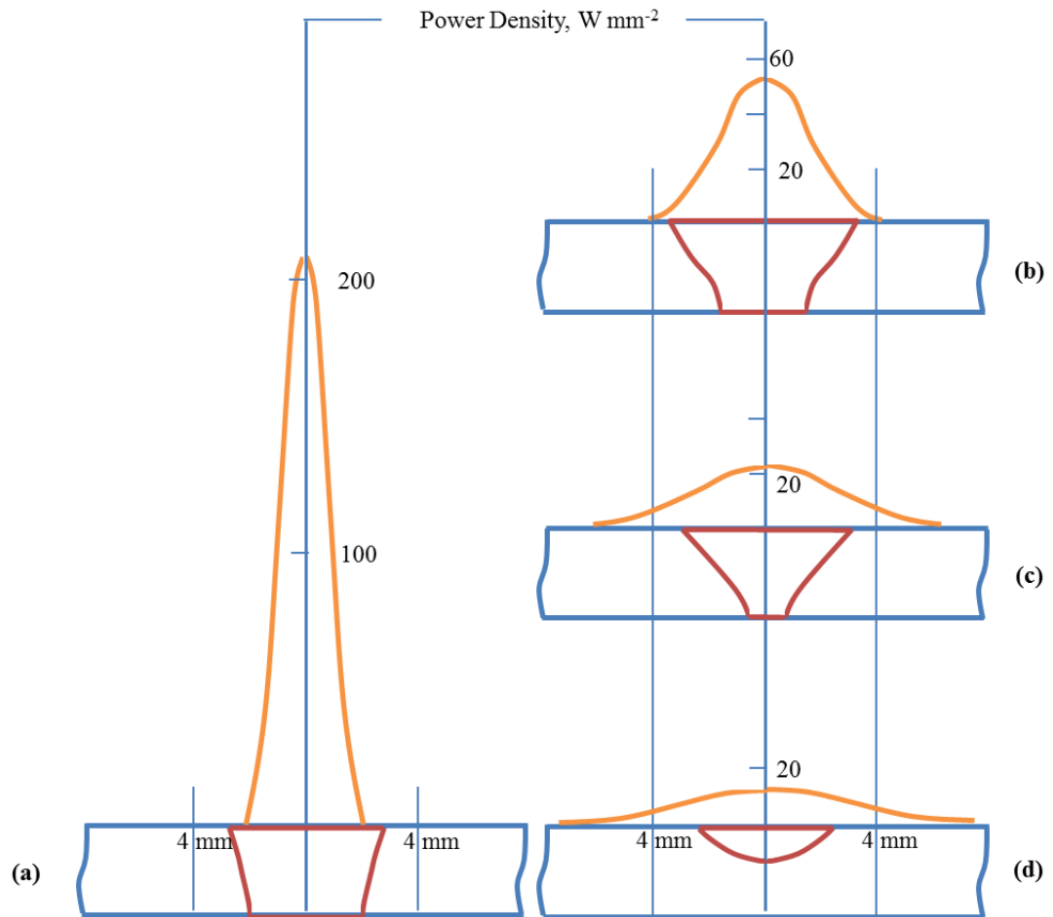
Figure 10. Representative view of the effect of power density on depth of weldments [1].

Weldability of the materials also depends on the design of the welding operations. Dimensions, level, type, strain rate, arrangements of the joints and distribution of the applied load affect the design factor. Environmental variables, e.g. temperature and humidity, are other important parameters for welding operations. The process based parameters can be listed as follows:

- Welding method,
- Joint type and bevel design,

- Filler type and chemical composition,

- Auxiliary consumables,

- Specific point energy,

- Pre-heat (inter-pass and pre-heating temperature),

- Post-weld treatments,

- Heat input.

Finally, the purpose factor is defined according to physical, mechanical and chemical properties.

Fusion welding is typically operated in two modes; key-hole or melt-in (conduction) mode. In the key-hole mode, the heat is localized on having an incident power density. The focused heat leads to have a columnar vapor cavity within the molten material. Effect of the high power density, 200 W/mm^2 that forms the key-hole, can be seen in Figure 10, in which depth of penetration and the bead form are illustrated (Figure 10a). However, power density decreases as the penetration depth increases. This change occurs for constant interaction time and welding power (Figure 10 b, c and d).
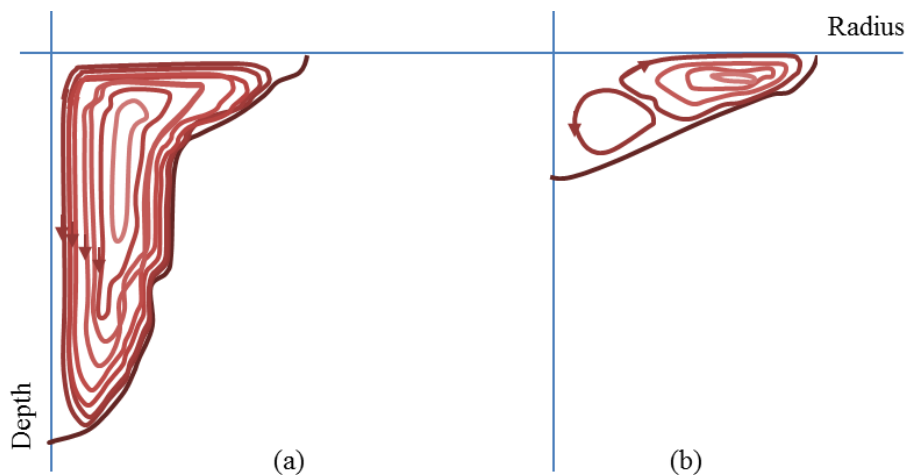
Figure 11. Weld pool illustrations (a) the reversed Marangoni effect and (b)the Marangoni effect [1].

The key-hole is maintained during operations, which depends on the equilibrium between the forces created by vapor pressure and those exerted by the surrounding molten material, where the gradient of the surface tension of the weld pool is turned from negative to positive which is normally positive to negative in the conduction mode of welding (Figure 11b) [21, 22]. This effect leads to a reversed and more intensive turbulence, towards the centre of the weld pool (Figure 11 a) [23].

2.4.2. Weldability of Material

Weldability of HSLA and some of the line pipe steels, such as API 5L X70M, X80, X100, and X120, are identically better than lower grade line pipe steels because of their material properties as illustrated in Section 2.2. The weldments create the new regions, namely fusion zone (FZ) , and change the regions, namely heat affected zone (HAZ), by fusion and thermal cycles. Thermal cycles exist only if the weld bevel or the gap between two base (parent) metals were filled in two or more pass. The representative view of multi-pass weldments is shown in (Figure 12).
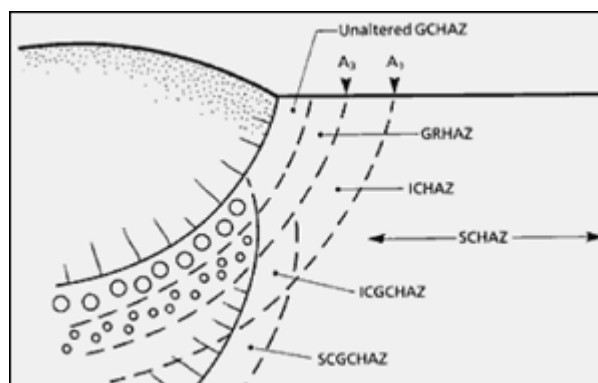
Figure 12. Illustration of heat-affected zone with abbreviations [24].

The success of welding procedure can be controlled by HAZ investigations because this region is the weakest location in terms of material properties. The microstructure of the HAZ is altered due to heat input and diffusion of welding consumables. Normally, the cooling rates is directly related to heat input. In other words, if there is no external parameter or applications on weldments, the cooling rates oppositely

proportional to the amount of heat input. From a metallurgical point of view, as heat input increases or cooling rate decreases, the grains within HAZ are enlarged. The width of HAZ also increases so the microstructure in these regions changes as seen in Figure 9.

The deteriorative effect of heat on microstructure is directly seen in CGHAZ and IRCGHAZ. In these regions, enlarged grains include many kinds of morphological formations, which have diversified chemical and mechanical properties. The typical example is the formation of martensite-austenite islands in some line pipe steels, like X70M and X80. In IRCGHAZ, results in high strength and lower toughness [2, 4, 25, 26]. The amount of some micro-alloying elements, Ni, V, Nb and Ti, directly affect the amount of phases. If the filler wire includes high amount of austenite promoter elements and the enough diffusion time is given, for low cooling rates various kinds of austenitic phase exist in CGHAZ and IRCGHAZ.

The cooling rate after welding also affects the width of HAZ. Lower cooling rates cause increasing growth rate during solid-state diffusion in HAZ. The fine grained structures shift towards the base metal till the phases become completely transformed or stable. The partially-transformed HAZ morphologies can be changed depending on the above mentioned parameters. The stable structure in these regions becomes unstable when exposed to enough amount of heat. The mechanical properties of these regions are deteriorated compared to those of the parent metals.

Furthermore, welding techniques applied on various metals cause different microstructural and mechanical features depending on the fabrication parameters.

2.4.3. Arc Welding Techniques (SAW, GMAW, FCAW, PAW)

Arc welding is a fusion welding process which employs heat of an electric arc between the parent metal and the electrode to fuse parent and filler metals. Welding electrodes can be in different types, non-fusible or fusible. Fusible welding electrodes have complementary chemistry as the parent metal and are employed as filler to bridge the joint gap; hence they are consumed. Non-fusible welding electrodes are made of metal alloys, which have high-melting points, such as tungsten with oxide additives and pure tungsten. In technical manner, tungsten electrodes are not fused during welding operations, except for a very small region at the electrode tip. Therefore, they are also called as non-consumable welding electrodes.

The fusion or molten zone should be protected from the atmosphere to control the zone's metallurgy. All atmospheric gases, like oxygen, hydrogen, nitrogen, carbon-oxides, can react with the molten metal, causing bad metallurgy or defects that weaken the weld and the material, during any arc welding operations. Flux or shielding gas is used to protect the weld pool and the HAZ from atmosphere. The basis of the arc welding classification is defined by the way of shielding and the structure of an arc.

The basic and conventional arc welding techniques are given in Figure 8 with their standard codes and formal names as per both European norms and American codes. International Standardization Organization abbreviates the welding techniques with both numerical and alphabetical codes.

Shielded metal arc welding (SMAW), is typically a manual arc welding process that consumes a fusible welding electrode coated in flux to lay the weld. This welding method is also known as manual metal arc welding (MMA). The technique is invented before the other arc welding methods. "As the weld is laid, the flux coating of the electrode disintegrates, giving off vapors that serve as a shielding gas and

providing a layer of slag, both of which protect the FZ and HAZ from atmospheric contamination [1]" The coating flux may have rutile, cellulosic, or basic character according to quality requirements and the application.

Figure 13. Classification of arc welding methods according to the standards [1].

Gas Metal Arc Welding (GMAW) and Submerged Arc Welding (SAW) methods require a mechanical consumable fed of tubular (flux cored) or solid wire electrodes. Haughton was proposed mechanical feeding in 1928 (Figure 13). HAZ and FZ are protected from the atmospheric contamination via "submerged" under a blanket of the granular fusible flux consisting of silica, lime and other ceramic compounds in the SA welding operation, whereas GMA welding uses a gas or a gas mixture in order to shield the weld zones. Shielding gas or molten flux forms plasma columns which provide a path for stable arc between the parent metal and the wire electrode.
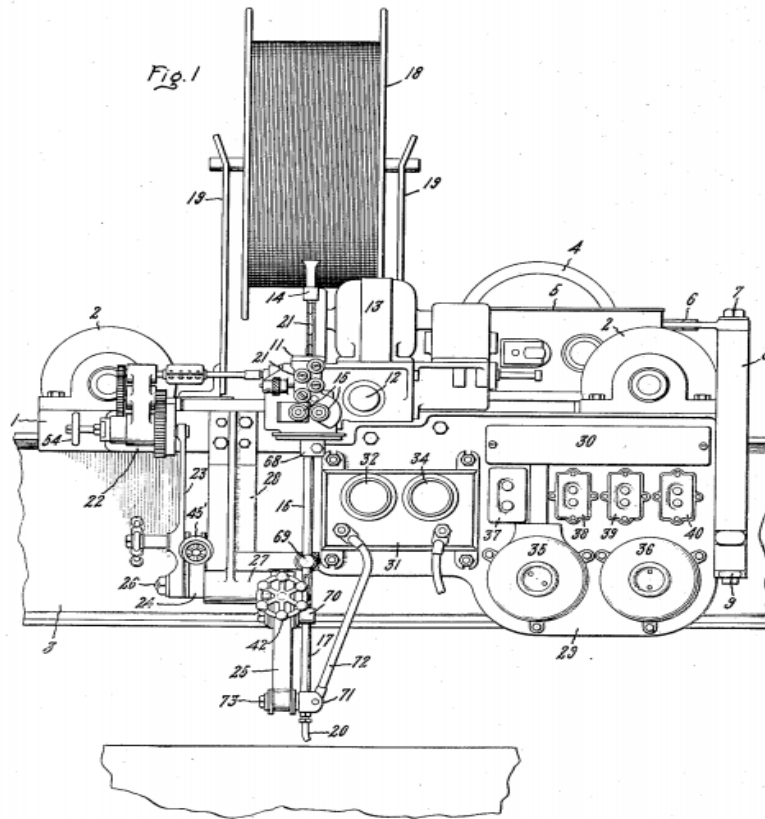
Figure 14. Representation of first invented automatic-arc welding machine [27].

The Plasma Arc Welding (PAW) and its predecessor, GTAW, use non-fusible tungsten electrodes rather than a fusible welding electrodes to form the arc. The filler wire can be or cannot be employed during PAW and GTAW operations. The short arc length of GTA welding needs a great care to prevent contact between the parent metal and the welding electrode. It provides the possibility to obtain high precision works. PA welding was developed from GTA welding. PAW affords a condensed arc by the help of a small orifice. Constricting the arc yields high power density; hence, a deeper penetration can be attained compared to conventional arc welding methods.

The essential function of the shielding gas or the flux is to protect the molten metal from atmosphere and the imperfections due to the contamination. Moreover, each gas and flux has unique physical features, which cause variations on penetration, linear welding speed, seam appearance and form, dilution and arc stability. During arc welding operations, the atmosphere between the parent metal and the electrode, and surfaces of the electrode and the parent metal are dissociated and ionized to receive charged particles, i.e. ions and electrodes. The required energy to remove one electron from the atom is called ionization energy. Some examples for the ionization energy during welding processes are represented in the Equations 1, 2, 3, 4, and 5 [28]:

$$CO_2 = CO + \frac{1}{2} O_2 \tag{1}$$

$$H_2 = H + H; H = H^+ + e^- \tag{2}$$

$$N_2 = N + N; N = N^+ + e^- \tag{3}$$

$$Al = Al^+ + e^- + 4.0 \ eV \tag{4}$$

$$Fe = Fe^+ + e^- + 4.8 \ eV \tag{5}$$
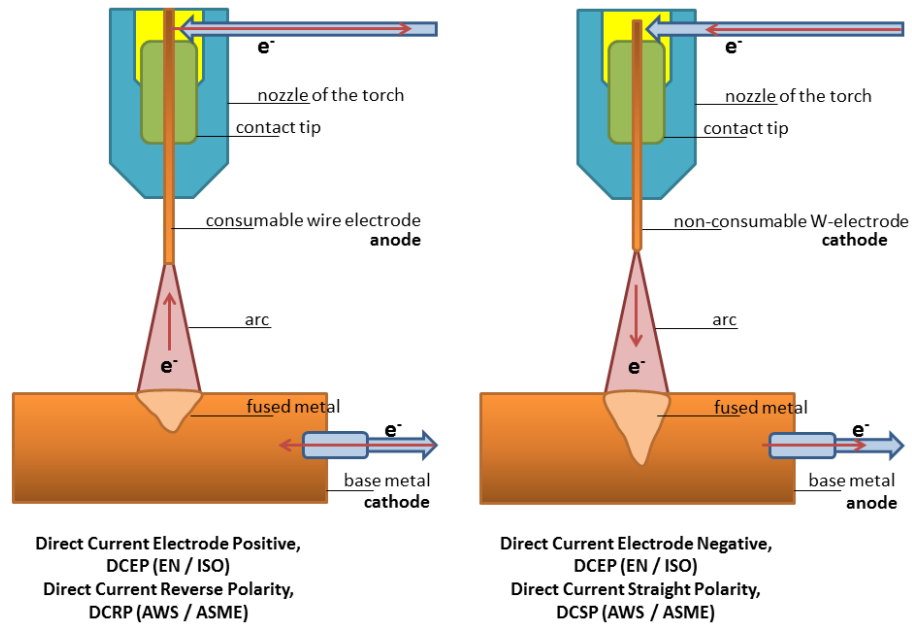
Figure 15. Schematic view of direct current polarization types existed until the end of arc welding operations [1].

High temperatures are obtained during arc welding processes. The arc temperature reaches maximum 6000°K during conventional arc welding operations. High-density plasma arc in the PA welding process, the temperature is about 30000°K [28]. Charged particles are removed directly from the metal lattice similarly the electrode surface and the parent metal at high temperatures. The electrostatic field of the welding potential, between the cathode and the anode, is responsible for the moving direction. Collision and movement of the ionized particles form the welding arc.

The anode temperature is generally higher than the cathode temperature for the conventional gas-shielded arc welding processes. The polarity is determined by using the temperature differences. Two different direct current polarization methods during arc welding operations are shown in Figure 15.

While the arc welding operations, i.e. PAW and GTAW, use direct current electrode negative to provide a fusing priority to the parent metal, GMAW presents reverse polarity to let the wire melt simply to have a high metal deposition.

2.4.3.1. Submerged Arc Welding (SAW)

The heat, produced via electric arc existing between the work-piece and bare electrode / wire, is used to join the plates each other using wire-flux mixture. One of the major constituents of SAW method is flux, which helps to cover all the weld pool during operations. Some of the flux and molten metal are mixed due to generated heat, and it forms a slag on the surface of weldments. The slag protects the weld pool and arc zone from atmospheric contaminations and avoids metal spatter. Complete slag cover on the weld pool prevents smoke during welding. Additionally, the slag layer reduces cooling rate of FZ and HAZ. Therefore, weld bead becomes smoother, and the cracking tendency on the weld bead and intersections of FZ and HAZ reduces.

SAW is a widely used method to join thick plates with high welding speeds and deposition rates due to its high welding current, even greater than a thousand amperes. Obtaining high currents is possible because of slag covered molten metal, fusion zone, eliminated spatter tendency and larger consumables, which are bare wires. SAW has also a great tendency for multi-wire feeding applications because of acquiring high welding currents. The schematic view of SAW system is shown in Figure 16.
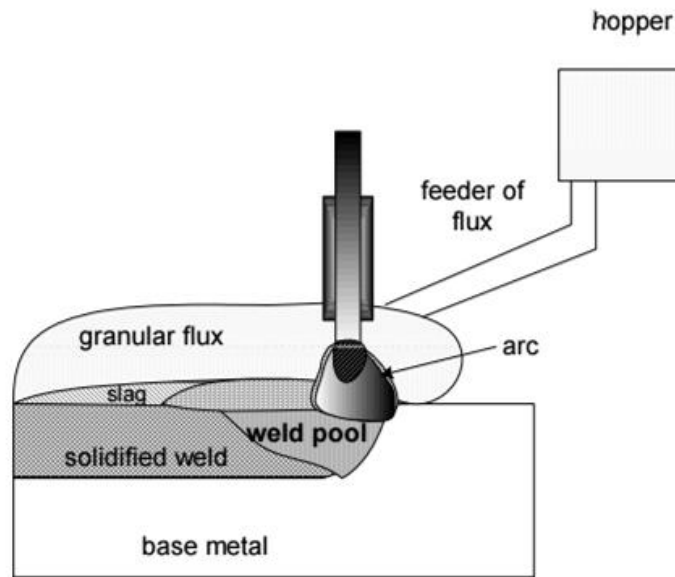
Figure 16. Illustration of SAW system.

The main advantages of SAW method are high productivity, continuous wire feeding, un-interrupted heavy-duty welding, high penetration capacity, smooth weld bead finish; almost no spatter and smoke. However, there are some limitations of SA, such as limited operation capacity on thinner plates, invisible welding arc, and flux retentivity difficulty on differently shaped sections.

The alignment of plates becomes an important issue due to the invisible welding arc. Columnar flux and arc are fully covered during welding hence the weld metal deposition could not be checked precisely. In other words, the alignment of each pass and the location of deposited metals might vary and dynamic motion of plates upon subjected to high heat input. These factors also limit the application of SA welding. The plates, thinner than 5 mm, cannot be joined by this method because of burning risk. The smaller diameter pipes could not be welded circumferentially due to falling tendency of granular flux.

From a metallurgical point of view, high heat input causes enlargement of grains, which are located just near the intersections of FZ and HAZ. Enlarged grains form regions, namely coarse-grain heat-affected zone (CG HAZ). The formation of CG

31

HAZ could also be investigated in detail. The increased growth rate and decreased nucleation rate due to lowered cooling rates promote grain growth. The larger grains cause reduction of mechanical properties of weldments, especially toughness of materials are deteriorated. To compensate the undesired effects of SAW, some post-weld treatments could be applied. For example, weldments are subjected to normalizing heat treatment to obtain finer grains in HAZ, and thus, higher toughness.

SA welding method is applied to a variety of materials, such as pressure vessels, structural components, pipelines (large diameter ones), etc. The techniques might be butt welding, key-hole welding, girth welding and fillet welding. Additionally, SAW is used for cladding purposes. SAW applications should be done in closed and controlled fabrication areas. The un-controlled areas sometimes contain moisture, which causes porosity in the weld metal, FZ. The girth weld operations are progressed by rotating the line pipe sheets without flawing of flux [29].

2.4.3.2. Gas Metal Arc Welding (GMAW)

GMA welding technique is mostly useful for vertical, inclined and overhead welds, with high speed and deposition rate. The welding electrode is fed over the tubular copper contact tip, which is placed in the welding torch, which has a nozzle surrounding the tip (Figure 18). The shielding gases include active and/or inert gases, which are mixed according to the material types. Gas mixtures consisting active gases (O_2 and CO_2) and inert (He and Ar) might be utilized for shielding of the steels, whereas only inert gases might be applied during titanium, aluminum, and magnesium alloy welding.

The electrical current passing over the contact tip to the wire electrode produces the arc. Therefore, the heat melts the end of the welding electrode. Molten electrode metal fills the gap between pieces by dropping molten metal.

Figure 17. Flowchart of welding processes and their outputs.

Dynamic forces of multiple origins, e.g. surface tension, electromagnetic fields, vapor pressure and gravitation, affect the detachment of molten metal droplet from the electrode tip [30]. There is a metal vapor on the weld pool. Vaporized metal creates pressure to the metal droplet, which is formed at the electrode tip. The pressure acts over the welding wire and tries to keep the droplet at the electrode tip. Gravitation effect depends upon the welding position. While gravitation helps the droplet fall down to the pool at the flat position, it tries to keep the droplet at the tip of the wire at the overhead position. Electromagnetic field and the surface tension of

the metal droplet are the dominating factors on the metal transfer regime which determine the size of the droplet and its transfer mode.
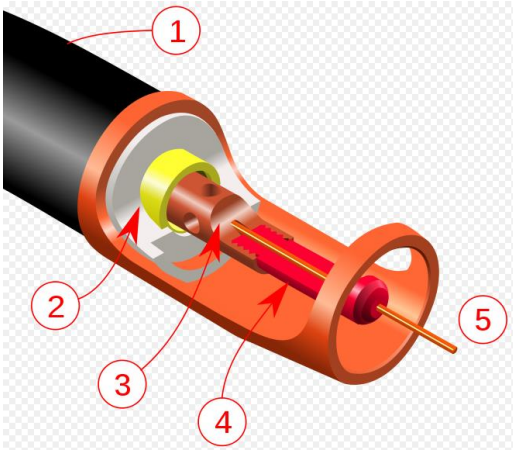
Figure 18. GMA welding torch nozzle cut away illustration; (1) Torch handle, (2) Threaded metal nut insert (yellow)and Moulded phenolic dielectric (shown in white), (3) Shielding gas diffuser, (4) Contact tip, (5) Nozzle output face [31].
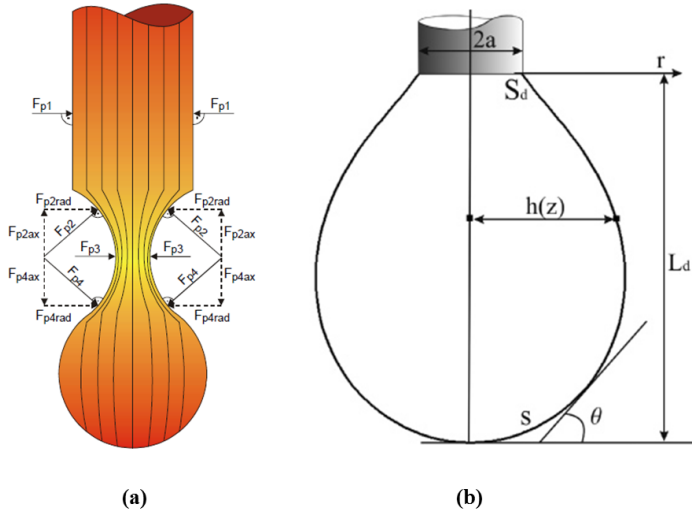
Figure 19. Existing Lorenz forces, a, and surface tension, b, on the metal droplet [32].

"Lorenz-force," which is provided by an electromagnetic field, is also termed as pinch-force since it creates a pinch effect on the neck of the droplet. The pinch

(Lorenz) force, F_P, is proportional to the square of the current amplitude, as given in Equations 6;

$$F_P = k \, \frac{P^2}{a},$$ (6)

where a is the cross-sectional area of the wire and k is a constant. If other factors are considered to be constant, increasing welding power leads to an increase in the number of droplets that fall into the weld pool per unit time.

Welding power is not only responsible for the pinch forces, but also for the viscosity of the metal droplet. An increase in the temperature of the metal droplet due to a high welding power decreases the viscosity of the metal droplet, which provides a lower surface tension of the droplet. The shielding atmosphere is another factor that determines the surface tension Figure 19. Using small amounts of active gasses as an addition to inert gases $(2 - 5\%)$ enhances the arc stability and reduces the surface tension of the molten metal droplet. It is possible to obtain small droplets by using gas mixtures that involve active constituent up to 25% due to this surface tension effect. Such gas mixtures are utilized for spray transfer welding of steels. Further increase in active gas content leads to higher surface tension and consequently the formation of bigger droplets.
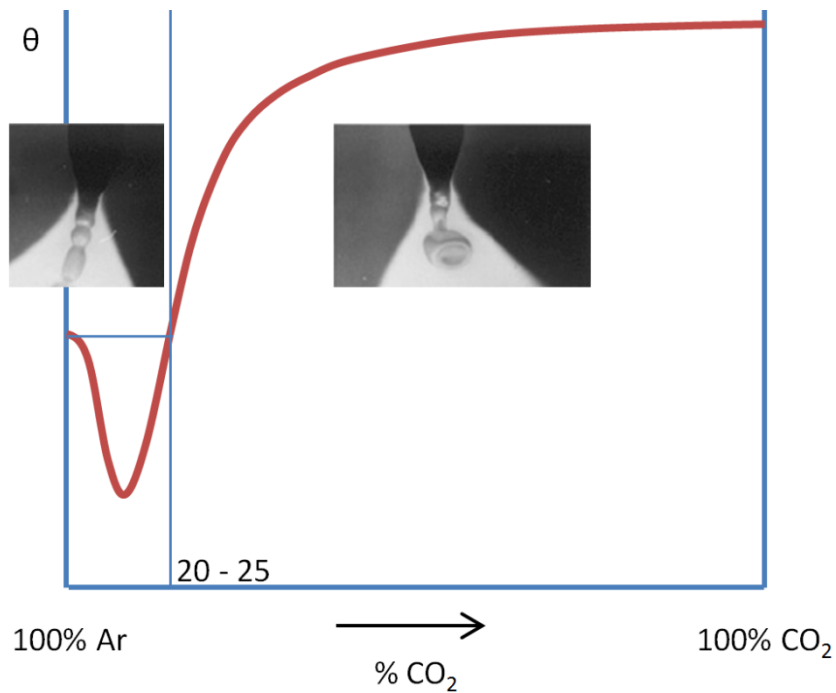
Figure 20. Illustration of shielding gas effect on metal transfer mode.

GMA welding power suppliers have the quasi-constant potential static characteristic. The output voltage remains almost constant due to this characteristic during the welding operations (Figure 20). Therefore, any change in the arc length leads to large current amplitude changes, and so, the welding power. The shorter arc length causes a decrease in the arc resistance, welding power and higher current amplitude, which employs the wire electrode melt in high rates, and thus, restore the original arc length in milliseconds. On the contrary, longer arc length leads to less current amplitude, higher arc resistances, and welding power, which causes the electrode melt in slower rates, and thus, restores the original arc length (Figure 21). The welder can keep the arc length steady during operations by the help of the process.

Torch

Wire Feeding Speed, m/min	5.6	5.6	5.6	5.6	5.6
Current Amplitude, A	200	150	200	250	200
Melting Rate, m/min	5.6	4.3	5.6	6.8	5.6

Current Amplitude

Time

Potential

200 A

150 A

250 A

Current Amplitude
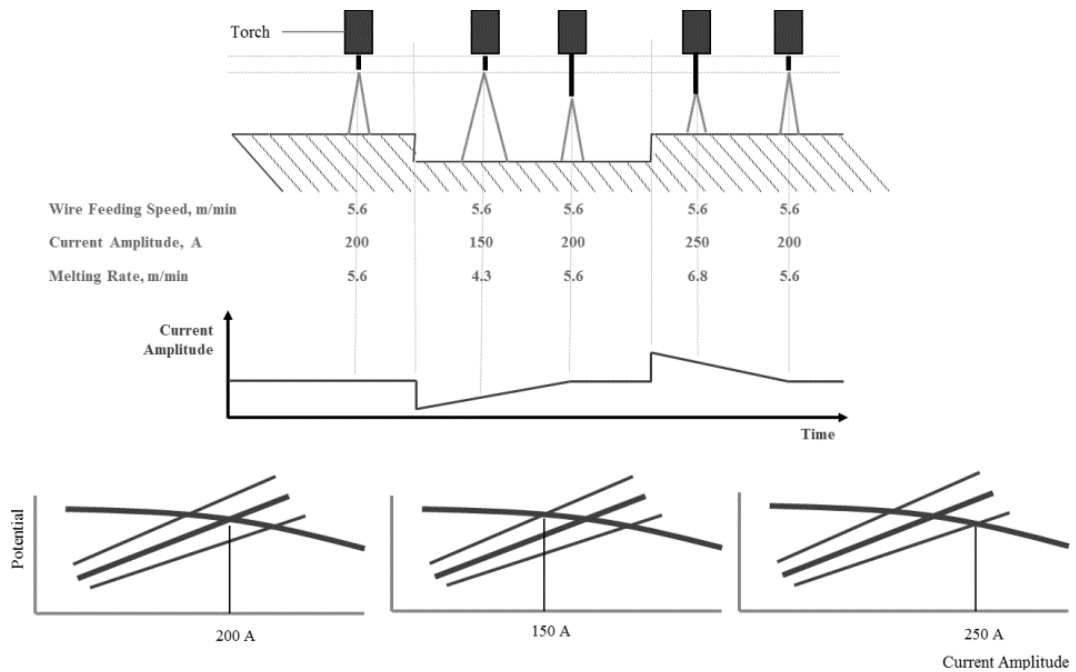
Figure 21. The self-correction of an arc length in GMA welding [1].

2.4.3.3. Flux Core Arc Welding (FCAW)

In the flux-cored arc welding (FCAW), the arc exists between the workpiece and tubular electrode or wire, which is fed continuously. This arc creates the sufficient amount of heat to melt the material. Shielding is generally obtained by shielding gas or flux, which exists in tubular electrode or wire.

Although there are similarities between GMAW and FCAW, this method has additional advantages for some applications. For example, high deposition rates can be obtained by FCAW. FCA welding is used to have good weldments in ferrous metals commonly. High currents are obtained without losing the control of the existing arc in comparison to GMAW applications. This method allows welders to see the weld pool clearly and to remove the slag, during welding. On the other hand, there are metal spatters and smoke because of nature of FCAW. The electrode or filler wire transfer occurs through the existing arc.

37
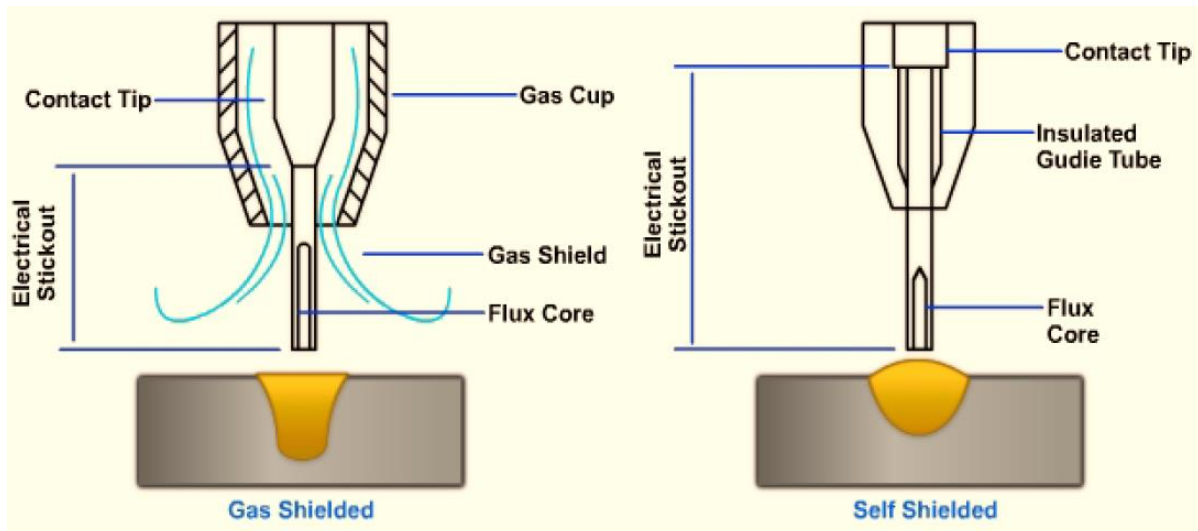
Figure 22. Schematic view of two different shielding types in FCA welding.

FCAW needs to be protected from atmospheric contaminations by a shielding gas. There are two sources, which are external shielding gas and self-produced shielding gas. Self-produced gas means that the gas could be generated from used consumables via decomposition of implicit gas-forming matters. Such consumable wire is a type of a flux-cored electrode and named as self-shielding electrodes.

Moreover, the slag layer slows down the cooling process, however, requires post-removing with manual equipment, like clipping hammer or wire brush. The self-shielding electrode usage simplifies the welding operation because of eliminating additional equipment, shielding gas tubes. These electrodes are mainly developed for stainless steels and low-alloy steels, but they can be used in mild steels too. FCA welding is generally applied after pre-heating. Pre-heating of flux-cored electrodes, especially self-shielding ones, increases burn-off efficiency and deposition rate; and decreases penetration depth.

There are some disadvantages of FCAW method, with self-shielding electrodes. The most critical one is that the weld metal might have poor metallurgical quality. The ingredients of the self-shielding electrode are highly denitrifying and deoxidizing agents. For example, these electrodes generally include aluminum as a primary

38

element inside the core. This causes lowering impact toughness and ductility of weld metal in fusion zone although it neutralizes the undesired effects of oxygen in the arc zone. The external shielded electrodes are used for critical applications to compensate these negative effects. External gas shielding allows having deeper penetration during welding and protecting the molten metal from detrimental effects of atmosphere without additional elements in the self-shielding electrode. The deeper auxiliary gas shielding during FCAW enables this method to be applied on low-alloy steels without losing mechanical properties due to better metallurgical quality in the fusion zone. Another advantage of the external gas shielding during FCAW operations is the achievement of higher currents and deposition rates via auxiliary gas shielding. Globular and spray transfer is possible with this type of FCAW applications.

2.4.3.4. Plasma Arc Welding (PAW)

Relatively new plasma arc welding technique was developed by modifying GTAW to improve the productivity of the method [33, 34]. This new method has some advantages which are higher LWS, lower heat input, and better root contour compared to conventional arc welding methods.

Generally, key-hole based technique is preferred, in which complete penetration is obtained, for PAW operations. A continuous hole is formed through the end of welding processes (Figure 23). Lower arc divergence can be obtained compared to GTAW arc by condensed plasma arc, hence arc length variations can be tolerated in a wide range. High aspect ratio can be attained due to high power density by PAW, which operated in key-hole mode. Tomsic and Jackson have been investigated the relations between process parameters of PAW and energy distribution, welf form and melting efficiency in detail[35]. The PAW can also be operated in melt-in (conduction) mode of welding.

Figure 23. Real illustration of key-hole based HPA welded steel.

It is stated that concentrating the plasma within a narrow jet yields high power density. Additional copper nozzle, which has smaller orifice compared to common equipment, allows to have constricted plasma jet. Contrary to the conventional arc welding techniques, two different shielding gases are blown in main gas nozzle. The interior gas, namely plasma or orifice gas, is completely inert to eliminate the oxidation problems on tungsten electrode. The shielding gas, which might be active or inert depending on the joined material, is blasted through the outer nozzle. The tungsten electrode, located inside the nozzle, has consistently negative polarity as in GTAW.

2.4.4. Welding Parameters (Welding Power, Specific Point Energy, Heat Input)

Theory of action of the arc has been discussed extensively. A typical arc potential curve is shown in Figure 24. Ayrton has shown that the relation between the current, I, flowing through the arc and the potential difference, U, across the arc can be expressed by the equation[36];

$$U = \alpha + \beta/I + [\![(\gamma + \delta/I)]\!]^2, \tag{7}$$

where 'α', 'β', 'γ' and 'δ' are constants. However, this definition can be applicable for the smaller arcs, few millimetres, air gap, and with low current amplitudes.

Ohm's law is used in current potential and amplitude relationship for the welding arc. The law states that the potential difference is directly proportional to the current amplitude across these two points. It means that the amplitude of the welding arc current increases with decreasing resistance (Figure 25), and vice versa, under constant potentials, according to Equation 8:

$$V = I R, \tag{8}$$

where 'I' is the amplitude of the arc current, 'V' is the arc potential, and 'R' is the arc resistance. If the arc length varies, the arc resistance changes in accordance with Equation 9 during the arc welding processes;

$$R = \rho L / A, \tag{9}$$

where 'ρ' is the resistivity of the arc, 'A' is the cross-sectional area of the arc, 'R' is the arc resistance, and 'L' is the arc length. In Figure 25, RS, RL, and RM stand for corresponding electrical resistances which are the shortest possible, the longest possible, and medium arc lengths, respectively. If the electrode tip goes further away, the arc might be distinguished due to that the maximum possible potential difference will not be enough to keep the arc alive. Moreover, if the electrode tip gets too closer than the shortest arc length, then the arc will be distinguished because of the contact between the work-piece and the electrode, which causes short circuiting.
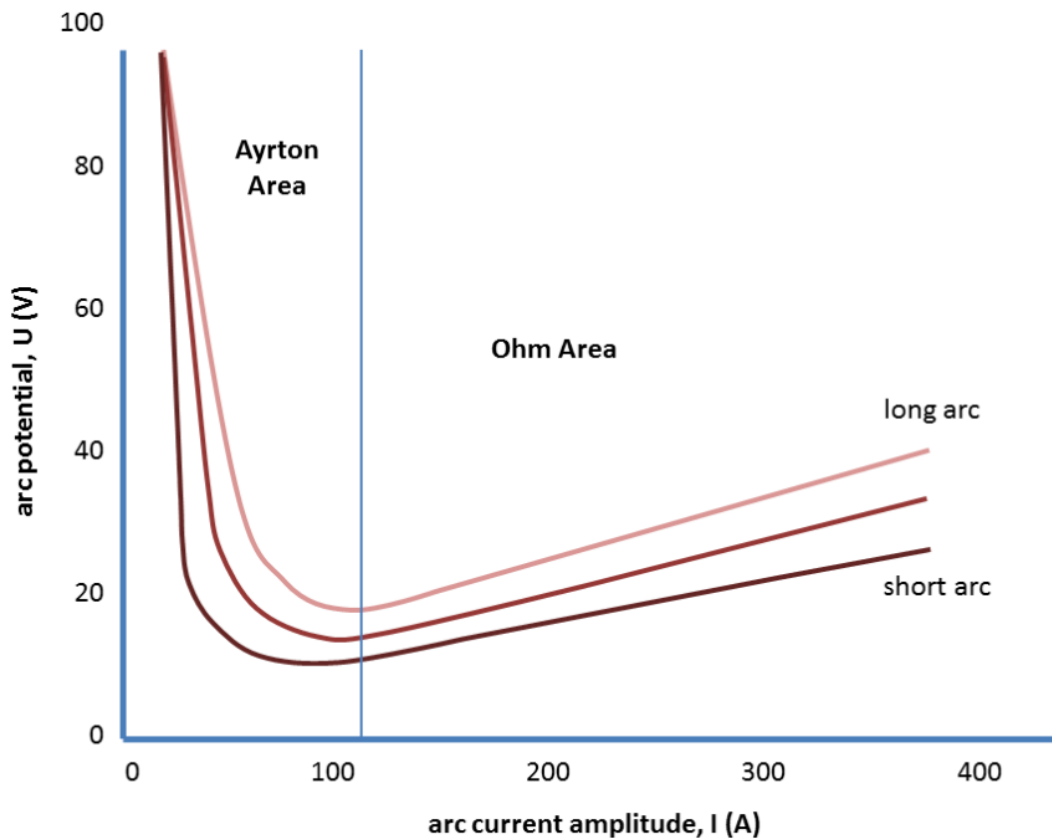
Figure 24. Variation of arc potential with current amplitude.

RC welding needs a power supplier, which should mainly be designed according to the welding technique. The power suppliers commonly have a transformer which rises the current amplitude and decreases the high voltage of the network, and the rectifier that transforms the alternating current to the direct current.

The power suppliers are designed in two different potentials versus current amplitude characteristics; constant current (droping) characteristics and namely constant potential (flat) (Figure 26). Actually, they are quasi-constant characteristics, developed via microcontrollers. Quasi-constant current power suppliers are chosen for manual welding methods, i.e. SMAW and GTAW, due to keeping the current amplitude almost constant is the principle concern to provide welder a short-term opportunity to fix what is wrong (position, welding power, linear welding speed, etc.) during the operation.   Since the power supplier provides a relatively small

42

change in the current amplitude, and consequently, arc power for the corresponding relatively large change in the arc potential or arc length, it is named as a constant current power supplier.
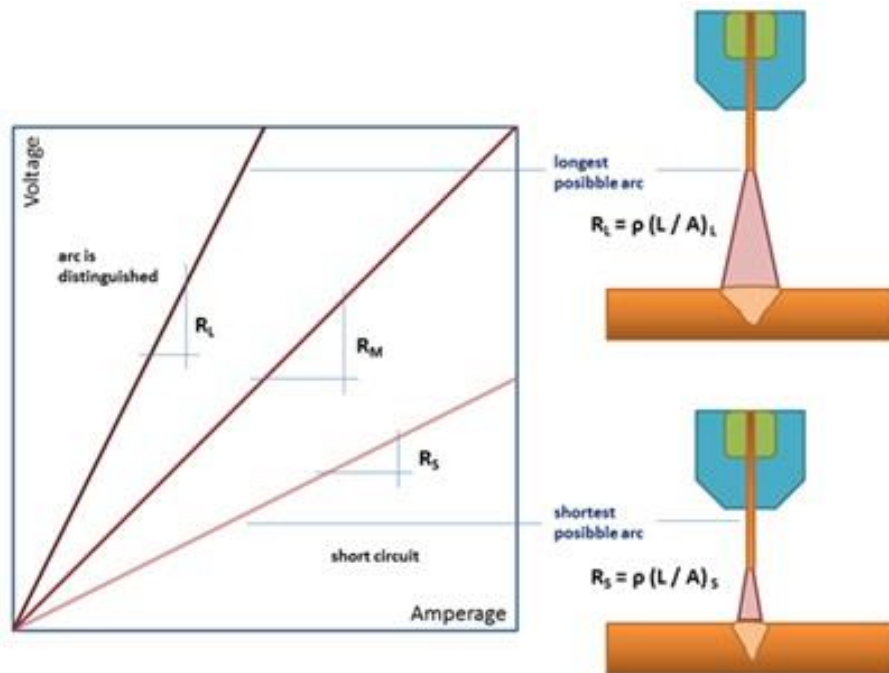
Figure 25. The graphical illustrations of potential difference variations with respect to current amplitude, with possible arc length relations.

Figure 25 shows a proposed diagram, which illustrates the welding process variations and the consequences of the applied welding parameters in physical and metallurgical senses. Moreover, interaction time, t_i, is an key parameter, which defines the weld pool convection, and so the heat transfer conditions and the penetration depth. The two major welding metrics, namely specific point energy and heat input can be determined by these welding parameters [37].

The specific point energy, E, can be calculated based on the Equation 10;

$$E = \rho A t\_i \qquad (10)$$

where 'A' is the area of the existing arc, 'ρ' is the power density, and 't,ɪ' is the interaction time, which is calculated according to Equation 11.;

$$t_i = \phi/_{LWS} \tag{11}$$

where ϕ is the diameter of the arc and LWS is linear welding speed.
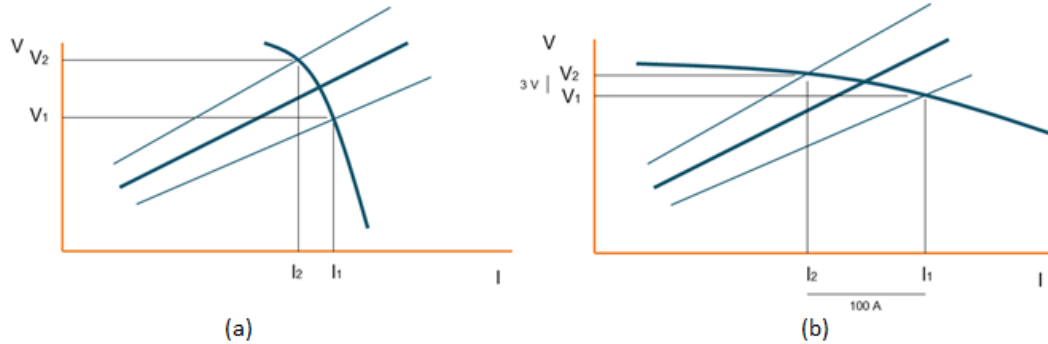
Figure 26. Graphical representations of two different purposes in static characteristics of welding power; a) quasi-constant current and b) quasi-constant potential.

The material based effective factors are geometry of the workplace and the heat transfer coefficient of the material. The process centered factor, the cooling rate, is mainly determined by the heat input during conduction mode of welding. The process based heat input, H, can be determined according to Equation 12;

$$H = \frac{p}{LWS}\eta \tag{12}$$

where 'η' is the efficiency factor and 'P' is the welding power for a specific welding method. 'η' is generally assumed 0.80-0.85 for GMAW and 0.60 for PAW [38-42].

2.4.5. Hybrid Plasma Arc Welding

The weldable thick materials can easily be joined in a single pass with higher linear welding speeds due to the advantageous characteristics of plasma arc. The plasma arc welding method is more suitable compared to laser beams in industrial applications because its high bridging capacity and wider spot size. The better microstructural properties might be obtained by combining the wire arc and the plasma arc. The combination improves the weldability of high-alloyed steels.

The high deposition rate and deep penetration capabilities are combined in HPA welding. This method is a combination of GMA and PA welding techniques. The capability of deep penetration allow to complete the joining in a single-run. The single-pass welding requires less consumables compared to the conventional techniques. Moreover, HPA welding provides less residual stress and less distortion in as-welded materials.

The principal advantages of the HPA welding:
- Does not require any special operational preparation,
- Small spot size,
- Deep penetration,
- Moderate power-density.

Although HPA welding employs such advantages, the welding parameter optimization and design are still significant to have proper material properties, which might be microstructural, mechanical and chemical. Especially, the high alloyed steels require much attention to be joined by HPAW due to their operational sensitive material characteristics. The applied heat input and power density might affect the microstructural evaluations imprudently.

1. Work piece
2. Plasma jet
3. Metal vapor column and surrounding molten metal
4. Orifice nozzle and Tungsten electrode
5. Consumable wire electrode
6. Wire-arc current direction
7. Plasma-arc current direction
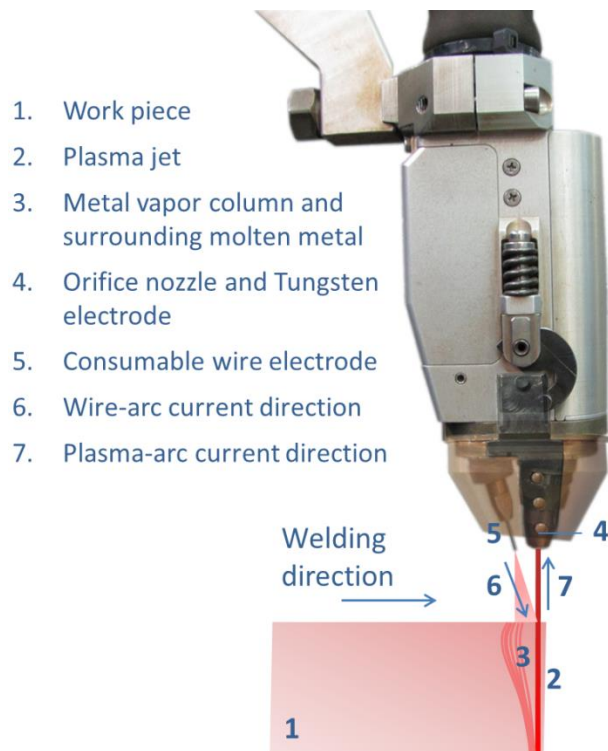
Figure 27. The schematic representation of HPA welding system, SuperMIG, designed and produced by Igor Dykhno and Georgiy Ignatchenko[43].

The hybrid-plasma arc welding method previously used during works completed by Yurtisik et al., Tolunguc, B. and Okan, K. [1, 44-47].

2.5. The Property, Elastic Plastic Fracture Mechanics and Fracture Toughness

The pipelines are subjected to different loads in industrial applications, such as oil or petroleum transportation and water transportation. The pipelines are designed according to the service pressure. The pressure is due to internal or external factors. In gas transportation pipelines are categorized as intermediate-pressure pipes. Although both internal pressure and external loads are almost similar, there could be large-scale axial plastic loads due to earthquakes or any other unexpected variations on the earth surface. Therefore, all the existing and suddenly emerging loads are modelled and investigated to eliminate any catastrophic failure in service condition.

The investigations are mainly performed to reveal fracture mechanisms which depend on material and application.

Conventional welding fabrication codes specify the maximum tolerable flaw size and the minimum tolerable Charpy energy, based on good workmanship, i.e. what can reasonably be expected within normal working practices. These requirements tend to be somewhat arbitrary, and failure to achieve them does not necessarily mean that the structure is at risk of failure.

Fitness-for-purpose analysis, or Engineering Critical Assessment (ECA), which is based on fracture mechanics principles, has been emerged in modern codes to assess whether a given flaw is safe with respect to brittle fracture, fatigue, creep or plastic collapse under the specified loading conditions. For such an analysis of a known flaw at the weldment, the following information is needed:

- Size, position, and orientation of the flaw,
- Stresses acting on the region containing the flaw, and
- Toughness and tensile properties of the material containing the flaw.
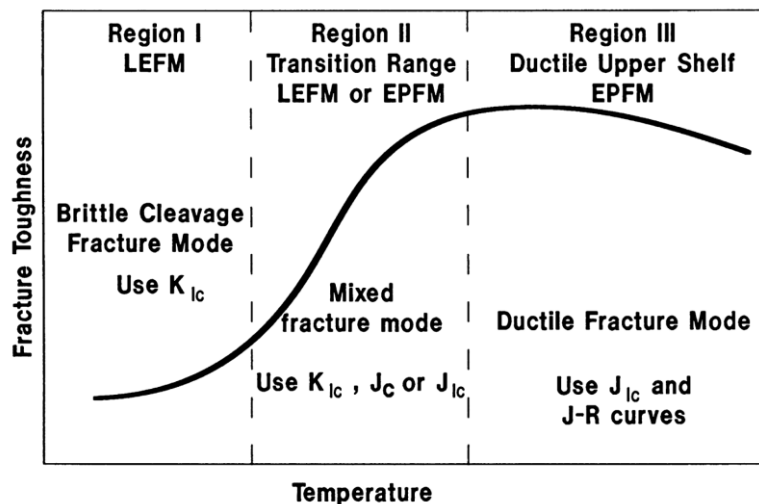
Figure 28. Dependence of fracture mode on temperature.

Fracture mechanics is categorized in two main theories based on crack tip plasticity, namely LEFM and EPFM, (Figure 28). In LEFM approach, the yielding at crack tips is assumed as small, so the material behavior correlates with plane strain conditions. The second theory is structured on non-linear material behavior, which could not be investigated via LEFM. Tough and ductile materials, work under plane stress condition and slow loading rates. The approximate yielding conditions for these fracture mechanic approaches are shown in Figure 29.
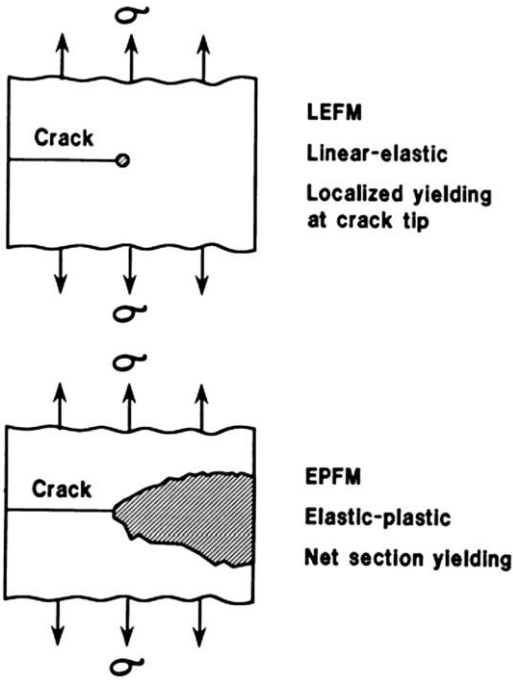
Figure 29. Illustration of yielding conditions of cracked bodies based on common fracture mechanics, LEFM and EPFM.

Some investigations have been done about the correction of the K factor for the plastic zone existing at the tip of the advancing crack. The plastic zones are evaluated to characterize the deformation before severe crack propagation. There are some local conditions adjacent to the crack tip affecting the material behavior. These local conditions can be analyzed via some EPFM parameters, such as J-integral, crack opening displacement, crack opening angle, crack tip work, crack tip force and failure assessment diagrams. Fracture behavior of a material can be the described

using fracture toughness, which could be represented as values of K, J, and δ. This term, fracture toughness, is used to define the resistance of materials to the crack propagation [48].

K, stress intensity factor, is used to describe elastic materials' resistance to crack extension when singularity zone is larger than the plastic zone at the crack tip. K value strictly depends on the crack size and existing stress. The plain-strain fracture toughness, KIC, can be measured if there is no plastic-zone at the crack tip. The additional requirement to define KIC is slow loading rate under linear-elastic conditions.

$$\sigma_{ij} = \frac{K_I}{\sqrt{2\pi r}} f_{ij}(\theta) \tag{13}$$

$$r_y = \frac{1}{2\pi} \left(\frac{K_I}{\sigma_{ys}} \right)^2 \tag{14}$$

Pipelines are usually subjected to a large-scale axial plastic load. The applied load causes plastic deformation at the crack tip where the materials are categorized as elastic-rate-independent materials. Fabricated line pipe steels and welded ones need to be characterized according to the elastic-plastic fracture mechanics (EPFM). The fracture toughness of these materials can be idetermined by CTOD or J-integral methods.

The j-integral method is generally used when the material and applied load are not suitable for the linear elastic fracture mechanics (LEFM) approach. The non-linear fracture behavior of materials, under the condition that there is strong plastic deformation at the crack tip in service conditions, can be determined by the help of plasticity theory. This theory requires a new measurement method and term J-integral. The formulations could be seen in EQs 15 and 16.

$$J = \oint_r \left(wdy - T_i \frac{\partial u_i}{\partial x} ds \right) \tag{15}$$

$$J = \left[\left(\frac{S}{W}\right)\frac{F}{(BB_N W)^{0,5}} g_1\left(\frac{a_O}{W}\right)\right]^2 \left(\frac{1-v^2}{E}\right) + \left[\frac{2U_p}{B_N(W-a_O)}\right]\left[1-\left(\frac{\Delta a}{2(W-a_O)}\right)\right]$$

(16)

Wells proposed a new fracture mechanics parameter, CTOD, and it is represented by a symbol δ [49]. This approach is used to extend LEFM to EPFM by the help of well-known estimations and proposals, such as Irwin's plastic zone size determination for the infinite plate and Dugdale's plane stress yield model for totally plastic materials [50]. CTOD examination is used to find engineering fracture parameters in an easy way. The δ values could be used as J or K in practice equivalently [48]. Some of CTOD measurement formulas with respect to the applications or material types, such as elastic or plastic materials, could be seen in EQs 17-22 .

$$\delta_J = \frac{J}{m\dfrac{R_{p0,2} + R_m}{2}}$$

(17)

$$m = A_0 - A_1\left(\frac{R_{p0,2}}{R_m}\right) + A_2\left(\frac{R_{p0,2}}{R_m}\right)^2 - A_3\left(\frac{R_{p0,2}}{R_m}\right)^3$$

(18)

$$A_0 = 3,18 - 0,22\frac{a_i}{W}$$

$$A_1 = 4,32 - 2,23\frac{a_i}{W}$$

$$A_2 = 4,44 - 2,29\frac{a_i}{W}$$

$$A_3 = 2,05 - 1,06\frac{a_i}{W}$$

(19, 20, 21, 22)

Fracture toughness value depends on the material, fabrication process, environment and loading rate. The most important factor is the material which includes chemical composition, production method, microstructural constituents and fabrication method. Various methods can be applied to construct large objects. For example change in welding, the parameters change the microstructural evolution of materials entirely. Heat input is a major concern and effective parameter during welding. It adjusts the heating and cooling cycles during welding and states the final material properties. The cooling rate alters the microstructure directly. For example, increasing cooling rate reduces the average grain size and, generally, improves mechanical properties. Sometimes, the entrapped elements due to high cooling rates cause local detrimental effects. If the entrapped elements are too strong compared to both filler and base metals, the hard morphological formations will negatively influence toughness and ductility. They possess stress concentration regions and deteriorate the soundness of microstructure.

X70M (PSL2) steel is produced by TMCP which results in a very fine grained microstructure. Its fracture toughness values, δ, is around 1.2 mm at -10 °C, which is critical test temperature for on-shore gas transportation pipeline construction projects. In addition, the impact toughness values should be more than 27 J [5].

CHAPTER 3

EXPERIMENTAL STUDIES

3.1.   General

In this chapter, firstly, the base and the filler metals are specified with respect to technical standards. Next, the welding procedures with measured and calculated welding parameters are described. Inspection and testing methods, which were employed during welding integrity assessment and procedure qualification, are then addressed. It is followed by the sections describing the methodology and procedures for characterization of the parent metal and the weldments in terms of microstructure and mechanical properties. The last section describes the main focus of the thesis, i.e. the fracture toughness of parent and as-welded materials. Experimental techniques, standards, and the investigated material zones are tabulated in Table 6.

Table 6. Summary of the experimental investigations.

		Reference Standards	PM	FZ	HA
Elemental constituents	OE	ASTM E350	▓	▓	
	EDX	ASTM E1508	▓	▓	▓
Microstructural constituents	XRD	NBS Standard XRD patterns & ASTM E82	▓		
	OM	ASTM E112	▓	▓	▓
	SEM	ASTM E766	▓	▓	▓
Integrity	MT (MPI)	ISO 17638 & ISO 23279		▓	▓
	RT	ASTM E1742, ASTM E2007 & ASME BPV Code		▓	▓
	Macro-section	ISO 17639		▓	▓
	SB	ISO 5173		▓	▓
	CWT	ISO 4136		▓	▓
Hardness	HV	ISO 6507 & ISO 9015	▓	▓	▓

	Nano-indent	ASTM E2546 & ISO 14577			
Strength		ASTM E8 & ISO 6507			
Fracture toughness	CVN	ASTM E23 & ISO 9016			
	CTOD	ISO/DIS 12135&ISO 15653			

3.2. Parent and Filler Materials

The parent metal, 19.45-mm thick API grade line pipe steel, was delivered in the plate form (POSCO, South Korea), lot number SP48904) and conformed to API 5L Grade X70M PSL2 per the qualification report HRB132860 by the supplier.

The plate was sectioned for material verification and welding fabrication as well. Employing optical emission spectral analyses, elemental constituents of the parent metal was investigated and found to be consistent with the material certificate as per the standard EN 10204 type 3.1 (Table 3). The material was also verified in terms of its mechanical properties specified by the [5].

Mild steel solid and cored filler wires and a wire-flux combination were introduced to the weld bevels during welding operations. Welding wires and the flux were delivered from ESAB, company. Trade names and standard codes of the fillers are as follows:

- OK Flux 10.71 and 3.2 mm-diameter OK Autrod 12.24 wire (lot number PV442016287) combination, which is specified in the standards SFA/AWS A5.23 F8A2-EA2-A4, was introduced during SAW operations.
- 1.2 mm-diameter SFA/AWS A5.18 ER70S-6 (lot number PV534031289B), and
- 1.4 mm-diameter SFA/AWS A5.18 E70C-6M H4 (lot number PV3471022), were transferred during GMAW and HPAW operations.

The chemical compositions of the filler wires and the wire/flux combination are tabulated in Table 11.

3.3. Welding Procedures

Two conventional welding methods, SAW and GMAW, and a non-conventional hybrid welding method, HPAW, were used to produce the as-welded coupons in the laboratory. Besides, some coupons welded in the field were investigated for benchmarking. All coupons were coded with respect to the welding technique, location of production and the filler type (Table 7).

Table 7. Coupon designations.

	In-field		**In-laboratory**				
Purpose	Fabrication		Fabrication			Construction	
Application	Both-sides	Single-side	Both-sides			Single-side	
Method	SAW	GMAW	SAW	HPAW		GMAW	
Filler	F8A2-EA2-A4	ER70S-6	F8A2-EA2-A4	E70C-6M		ER70S-6	
Thickness	19.45 mm		16.00 mm			12.00 mm	
Code	SF	GF	SL	HC	HS	HL	GL

Standard welding procedures

Helical welding during line pipe fabrication is typically operated with a linear welding speed (LWS) of $1.0 - 1.5$ m/min via tandem method, which is adopted on SAW equipment. Two power sources, AC and DCEP, are utilized for two wire feeders to reach these operational rates. Wires are generally 4.0 mm-diameter under DCEP polarity, and 3.2 mm-diameter under AC polarity.

55

GMAW is preferred during construction girth welding operations. In GMAW applications, generally, the LWS is typically between 0.5 and 1.0 m/min for each welding pass. Transferring 1.0 mm-diameter filler wires, 19.45 mm-thick full-section girth welds could be joined in 10 to 12 passes. Contrary to fabrication, multi − pass welding is necessary during girth welding because rotating pipes during the process is not possible. The welding torches should be operated in over-head and vertical positions, as well as flat position, and therefore mass and fluidity of the weld pool should be carefully controlled.

Standard line pipe fabrication with SAW and girth welding with GMAW bevels are namely double-Y and J types, respectively (Figure 30). Standard and developed beveling and welding parameters are tabulated in Table 8.

Table 8. Welding procedures, parameters of joint geometries and average values of the process parameters (wire feeding speed, and linear welding speed, are in m/min).

	Joint geometry				Process						
	t, mm	α,°	a, mm	b, mm	Polarity	U_w, V	WFS	I_w, A	I_p, A	U_p, V	LWS
SF	19.5	30	2.0 ± 1.0	8.0 ± 1.0	DCEP	29	-	1100	-	-	1.20
					AC	31	-	550	-	-	
GF		5	0.0 + 0.5	1.5 ± 0.5	DCEP	29	10	250	-	-	0.75
SL	16.0	15	0.5	3.0 ± 1.0	DCEP	32	-	650	-	-	0.70
HC			1.5 ± 0.5		DCEP/N	29-31	8-10	400	190	15	
HS					DCEP/N		10-12	370	190		
HL		-		-	DCEP/N	31	16	400	160		0.50
GL	12.0	45	2.0 ± 0.5	0.0 + 0.5	DCEP	29	8.5	270	-	-	0.40

IN -FIELD WELDING OPERATIONS
FABRICATION (SAW)   CONSTRUCTION (GMAW)

IN -LABORATORY WELDING OPERATIONS
IN WELDING BOTH-SIDES   IN WELDING SINGLE-SIDE
SAW & HPAW   HPAW   GMAW
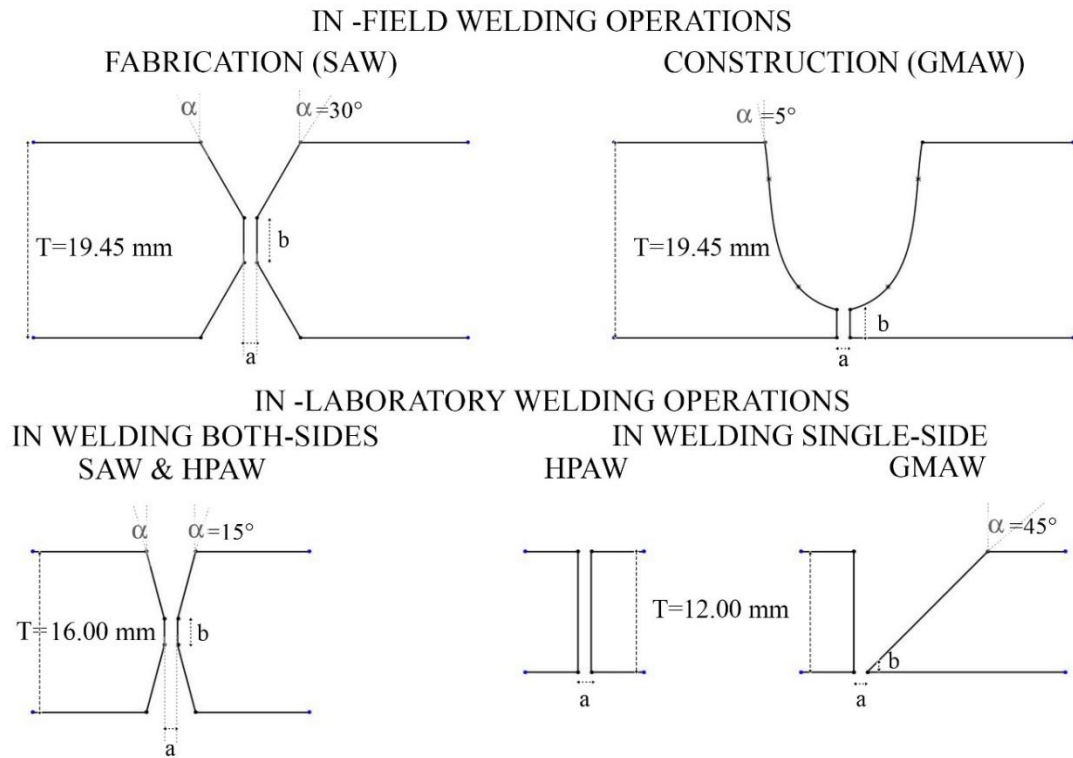
Figure 30. Parameters of the joint geometries.

Welding process optimization

In order to get uniform coupon geometries, the plates were first sectioned and ground down to 12.0 mm and 16.0 mm in thickness, for single-side and both-sides welding operations in the laboratory. Square-groove butt and beveled joints were employed for full-penetration welding operations. Whereas in-field production joints were obtained by standard sub-merged and gas metal arc welding procedures, in-laboratory welding procedures were optimized in terms of bevel geometry and process parameters.
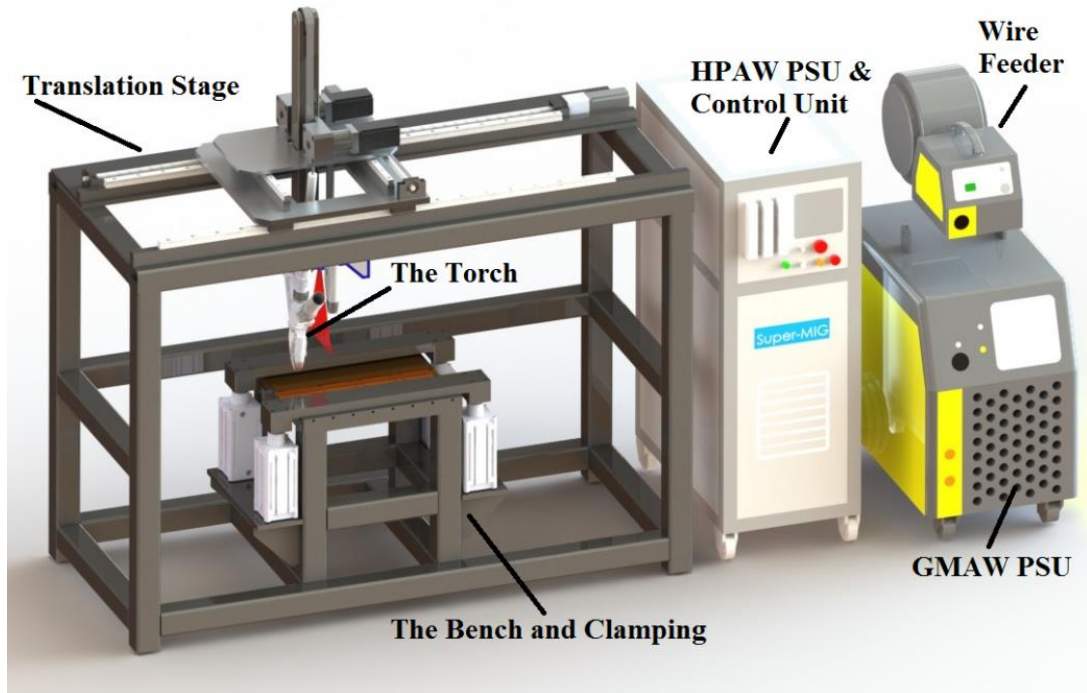
Figure 31. The 3-axis CNC welding manipulator.

The plates were located at the flat position and then joined by SAW, GMAW, and HPAW. These plates were aligned on the platform manually and clamped by the help of pneumatic cylinders. After clamping, the mechanized torch was driven along the machined bevels. Schematic welding set-up is given in Figure 31.

The shielding gases were used during GMAW and HPAW operations to protect the weld pool from atmospheric contamination. The shielding gas mixture was Argon-18% CO_2. In addition to the shielding gas, high purity (99.99%) Argon was used as orifice gas to cool down and consequently condense the plasma arc in HPAW. Shielding and orifice gas flow rates during the operations were about 14 to 18 lt/min and 4 to 5 lt/min, respectively.

While a single arc exists between the welding wire electrode and the work-piece in SAW and GMAW, two different arcs exist simultaneously in HPAW; namely a straight polarity (electrode negative) direct current (DCEN) between the work piece and tungsten electrode and a reversed polarity (electrode positive) direct current

(DCEP) between the welding wire electrode and the work-piece. Lanthanated tungsten electrodes, 2.4 and 3.2 mm in diameter, were employed to obtain the plasma arc. 2.4 mm-dia electrode provided higher power density at constant power values than the one provided by 3.2 mm-dia electrode, as expected.

HPAW and GMAW were employed for single-side welding applications. 1.2 mm-diameter SFA/AWS A5.18 ER70S-6 filler wire was introduced to the bevel in both welding techniques. HPAW was applied on the square-groove butt joint, and the gap was kept narrow in order to stabilize the condensed plasma arc, which requires equilibrium between the pressures of the orifice gas and the metal vapor through the keyhole. In order to ensure side wall fusion, half V-groove was preferred for the GMAW operation. While HPAW process was completed with a single pass, 5 successive GMAW passes were needed to complete the 12.0 mm-thick weldments.
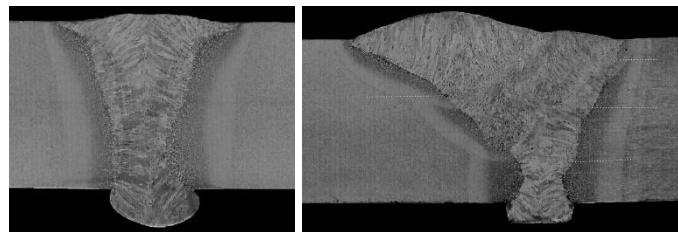
Figure 32. Macro-sections of single-side HPA and GMA weldments.
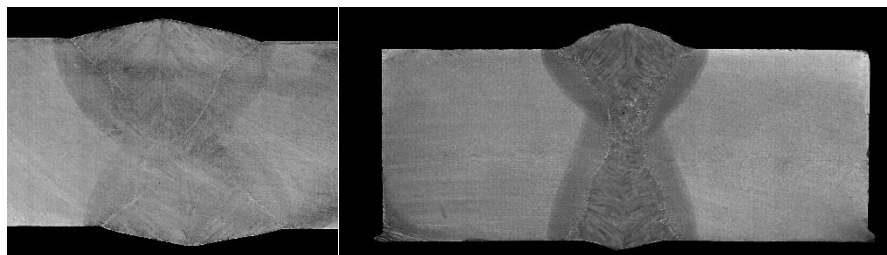
Figure 33. Macro-sections of double-side SA and HPA weldments.

HPAW and SAW were employed for double-sided welding applications. OK Flux 10.71 and 3.2 mm-diameter OK Autrod 12.24 wire combination, which is specified in SFA/AWS A5.23 F8A2-EA2-A4, was introduced during SAW. HPAW was

performed with two different filler wires; 1.2 mm-diameter SFA/AWS A5.18 ER70S-6 and 1.4 mm-diameter SFA/AWS A5.18 E70C-6M H4.

3.4. Integrity Assessment

Integrity assessments and procedure qualifications of the weldments were executed in accordance with the requirements of the standards API 5L and API 1104 [5, 51], including both non-destructive testing (NDT) and destructive testing (Table 6).
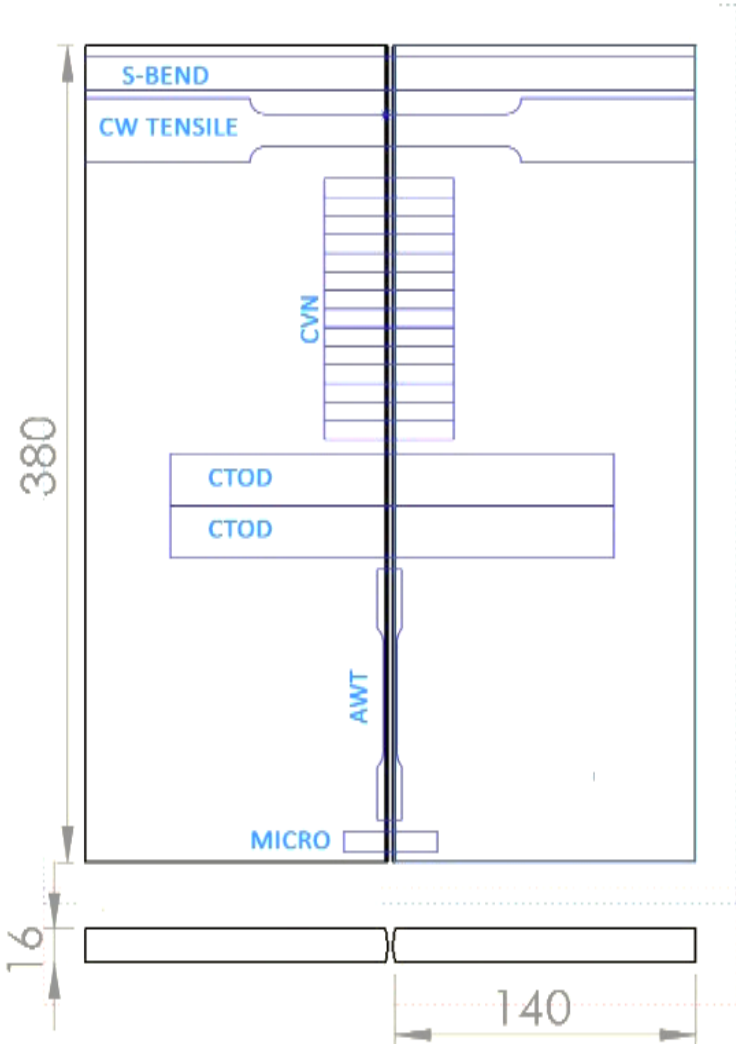
Figure 34. Sectioning plan for destructive tests of the welded plates.

Magnetic particle testing was applied to support the visual inspection and to examine possible weld surface discontinuities. The integrity of the weldments was confirmed

using radiographic inspection by X-ray, and the images were recorded on the digital radiographic films. Phosphorous imaging plate (IP) was used to record X-ray examination results instead of using conventional radiographic films due to its advantages, such as high image quality and reduced exposure / process times. The test was done according to ASTM E2007 [52], and ASTM E1742 [53], and films were evaluated as per the requirements and definitions in ASME BPV Code Section IX [54]. The quality level employed for radiography was 2 % (2-2T using hole type IQI).

Welded plates were then sectioned and tested according to the reference standards that are tabulated in Table 6.

Bend tests were done to ensure the soundness of the welded sections by 180° bending of the specimen in accordance with ISO 5173 [55]. This well-known integrity test generally reveals existing linear defects under the face of weldments.

The location of the fracture and the ultimate tensile strength at the location were determined during the transverse (cross-weld) tension test. Tension test was conducted at room temperature according to ISO 4136 [56] and API 1104 [51]. The schematic representation of the CWT specimen is given in Figure 35.
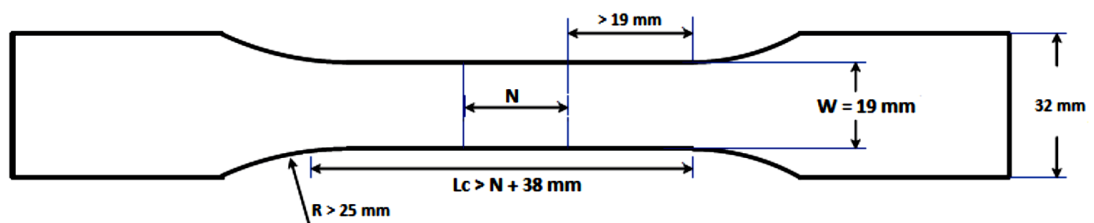
Figure 35. Illustration of the transverse tensile test specimen.

Macro-examination was done to determine the general structure of the welded joints by using 10% Nital reagent in accordance with ISO 17639 [57].

3.5. Mechanical Characterization

After macro-section examination, the specimens were subjected to macro-hardness examination using Vickers indenter (Shimadzu HSV-20). The applied load was 98N (HV10), and the diamond pyramid had applied load for 15 sec in each indentation according to ISO 6507-1 [58]. The distance between each indentation was 0.5 mm in HAZ and at least 0.5 mm in PM and FZ. Macro-hardness measurements were done on the weldments that were produced by using different welding parameters to control the weld integrity. The specimens examined through 3 rows; one 2 mm below the surface of the specimen at weld cap side, one 2 mm above the surface of the specimen at weld root side, and one approximately at the mid-wall thickness of the specimen. The base material and the HAZ at the both sides of the weld joint and the FZ were examined by 3 hardness indentations. Totally, 45 indentations and measurements were done on each specimen. The schematic representation of indentations can be seen in Figure 36. The macro-hardness calculations were done by using Equation 23, F represents applied load on the surface and d represents the length of diagonals.

$$HV = 0.102 \; \frac{2 \, F \, \sin {136°}/_2}{d^2} = 0.189 \; \frac{F}{d^2} \tag{23}$$
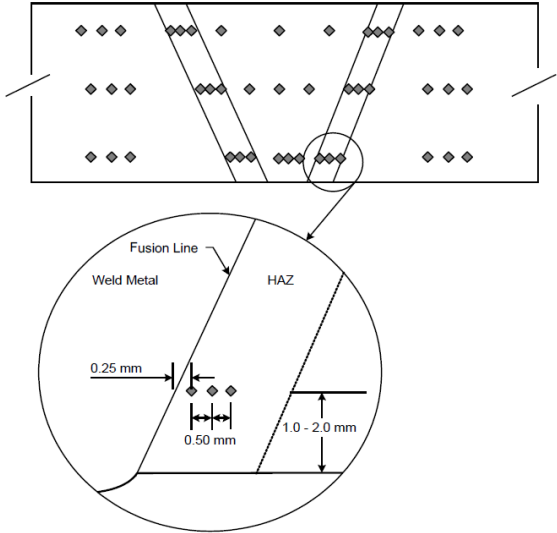
Figure 36. Schematic representations of the hardness indentations according to API 1104[51].

Macro-hardness surveys were then followed by micro / nano-hardness examinations on specific locations in the parent metal and weldment. Hardness variations between FZ and HAZ were investigated by CSM nano-indenter. The Berkovich nano-indentations were applied in each phase, in the base metal and HAZ, using a sharp 3-sided indenter. The loads were chosen as 10, 20 and 100 mN for the regions, CG HAZ, BM and FZ-HAZ transition respectively. The loads were applied for 15 sec, and each indentation had been completed in 6 min, with 2 min indenter stabilization duration. The inter-indent spacing was at least 2 μm in order to measure micron-sized microstructural formations, i.e. MA islands.

Strength and ductility values of the parent and filler metals were determined by uniaxial tensile testing, in accordance with ISO 6892-1 [59]. The test specimens were of the circumferential cross section with reduced width at the mid-length. Oblique view of the specimens is given in Figure 37.
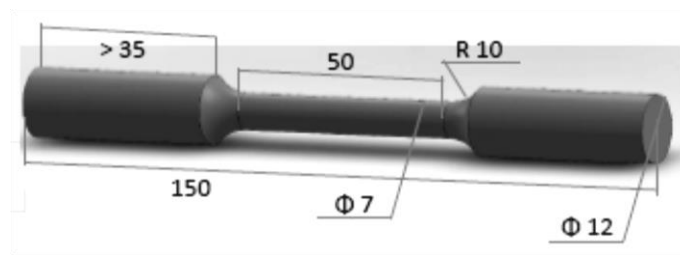
Figure 37. Oblique view of the tensile test specimens.

The specimens were tested with a speed of 0.6 mm/min, up to the yielding point, and then, with a speed of 5 mm/min by Zwick/Roell Z250.

Six temperature within the range of -30°C to -78°C were selected to assure DBTT behavior of the base metal for impact toughness tests. Other Charpy specimens were prepared as at least two sets, which contains three FZ and three HAZ specimens, and tested at -10°C. All specimens were machined to the dimensions of 10x10x55 mm^3, and notches were located at fusion lines (in HAZ) and weld metal (in FZ). The notch locations are shown in Figure 38.
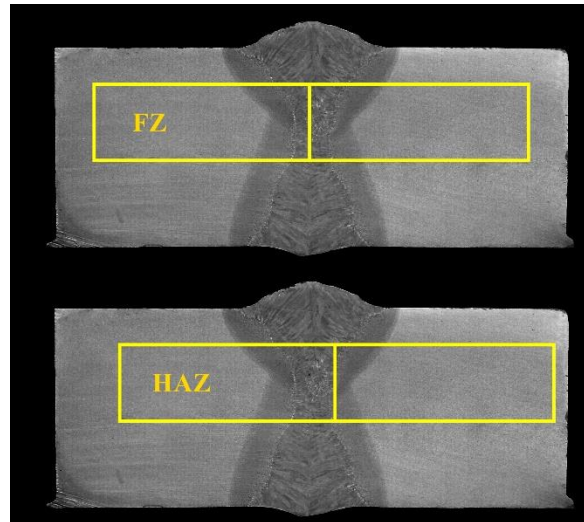
Figure 38. Schematic representations of notch-locations on the impact toughness
specimens.

Charpy impact tests of welded joints, by SAW, GMAW, and HPAW, had been completed at sub-zero temperatures in accordance with ASTM E23 [60]. Two sets (FZ and HAZ) of specimens were tested at -10oC. The specimens were machined to the dimensions of 10x10x55 (mm3) with their 2 mm V-notches transverse to the weld direction, perpendicular to the plate surface and centered at the weld metal and fusion lines at 4 mm below the weld top. The temperature of specimens was stabilized by digitally controlled refrigerator at least 10 minutes before testing. The dimensions of the samples were checked by Vernier calliper and certified GO / NO GO gauge. Experiments were conducted via Zwick/Roell RKP 450. The schematic representations of specimen placement inside the equipment could be found in Figure 39.
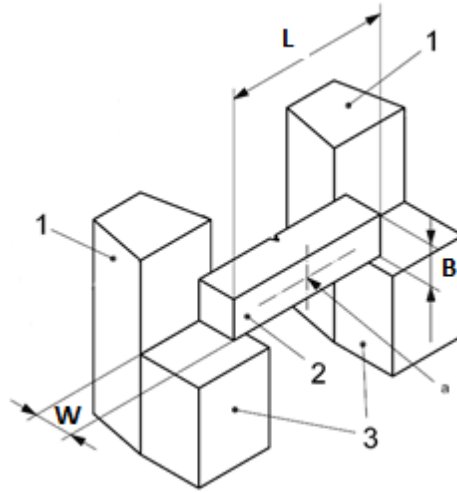
Figure 39. Schematic view of Charpy-impact toughness test setup [60].

Fracture toughness values depend on the crack plane orientation and the direction of crack extension in relation to the principal directions of mechanical working, grain flow, and other anisotropy. For testing of the as-welded samples, cracking will occur through the centerline of the fusion zone, P denotes the direction that is parallel to the welding direction, N and Q denote normal to weld and weld thickness directions, respectively. Therefore, NP orientation was chosen to complete the CTOD tests. In the first trials by SAW, the specimens were machined to the dimensions of 17x34x170 (mm3, B-2B specimens). The other two experiments, 12 mm-thick plates joined by GMAW and HPAW; specimens were machined to the dimensions of 11x22x110 (mm3, B-2B specimens). Other specimens, from 16 mm-thick joined plates by SAW and HPAW, were machined to the dimensions of 15x30x150 (mm3, B-2B specimens). The notches were machined in accordance with ISO 12135 [61] and ISO 15653 [62] via wire-cut electric discharge equipment. The 0.25 mm-dia wires were used during this operation. Notch locations were marked and recorded by photographs before machining via pre-test metallography methods. Pre-tests were conducted just after giving final dimensions by using 10% Nital reagents. The chemical compositions of used reagents are given in Table 9. Notch locations can be seen schematically in Figure 40.
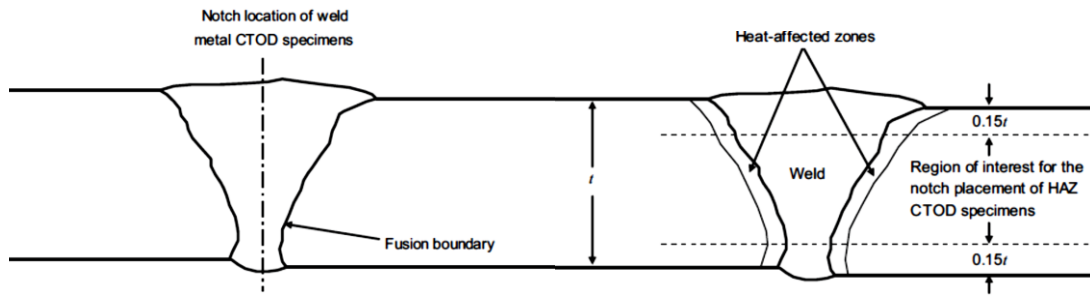
Figure 40. Schematic view of the notch locations on the CTOD specimens [61].
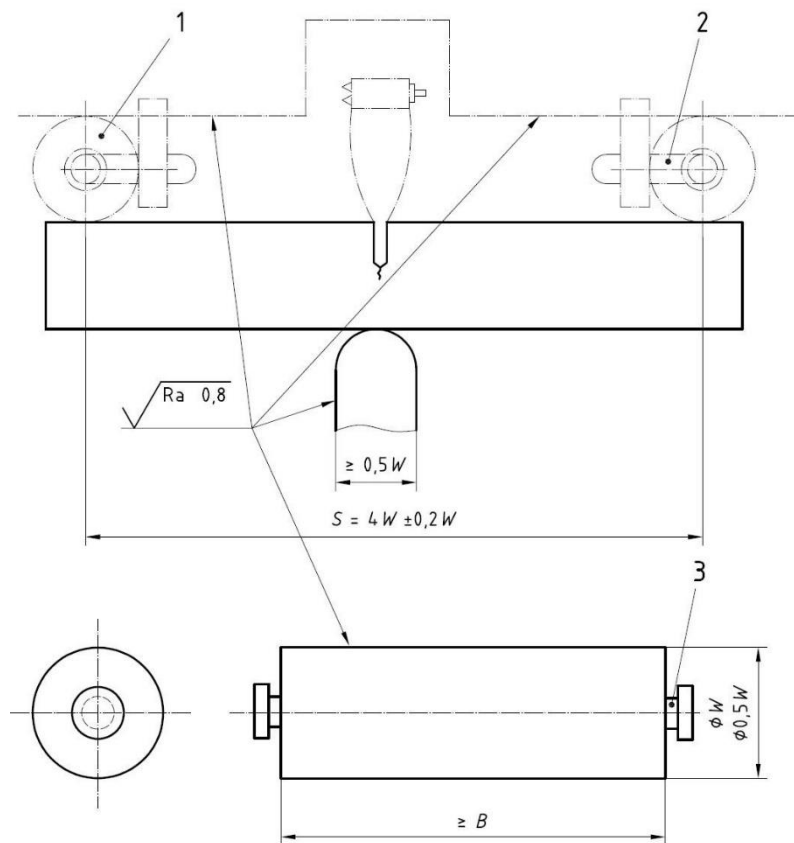
Figure 41. Schematic view of the CTOD test set-up [61].

The specimens were subjected to local compression before fatigue pre-cracking operations. Fatigue pre-crack loads were chosen according to tensile test results of each weldment. This operation was carried out by using MTS servo-hydraulic dynamic testing equipment, and all data was recorded to detect any equipment- or operator-related errors during pre-cracking. The final crack lengths were checked

continuously in order not to excess the limits given in ISO 12135 []. After fatigue pre-crack, the specimens were tested in accordance with same standards and the COD data were collected via KYOWA model gauge. The COD gauge was located at the top of the notch Figure 41.

Next, the crack lengths were measured on the broken surfaces by nine point method Figure 42 to calculate δ values.
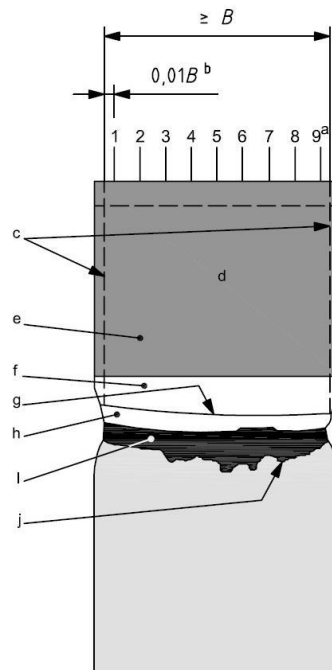
Figure 42. Illustration of the fracture surface, used for crack length measurements [61].

Furthermore, the CTOD experiments were conducted at -10°C and their temperature records were kept via calibrated thermocouples. At least six specimens were tested for each weldment, and the results were tabulated. The fractured surfaces were investigated (section 3.6.).

3.6. Metallography and Fractography

Microstructural characterization part was carried out using metallography, X-ray diffraction analysis (XRD), energy dispersive X-ray spectroscopy (EDS) and fractography. The reagents used to reveal the microstructures are given in Table 9.

Table 9. Various reagents used for metallographic investigations.

Reagent	Composition	Application	Aim
2% Nital	2 wt% Nitric Acid (HNO_3) 98 wt% Ethanol (C_2H_6O)	10-15 sec etching after 1 μm diamond colloidal polishing	Microstructural Investigation
10% Nital	10 wt% Nitric Acid (HNO_3) 90 wt% Ethanol (C_2H_6O)	15-30 sec etching after 1000 grid SiC abrasive paper grinding	Macro-observations
LaPera	1 wt% Sodium-meta-bisulfite Na2S2O5 4 wt% Picric acid C6H2(NO2)3OH 46 wt% Ethanol (C_2H_6O) 49 wt% Demineralized water	15-30 sec etching after 1 μm diamond colloidal polishing	Selectively distinguish between phases (ferrite, pearlite/bainite/cementite, and martensite/retained-γ)

Base metal was characterized after sectioning the received plates in accordance with the methods listed in Table 9. For instance, one of the sectioned plates were

powdered by manual filing for XRD analysis. XRD analysis was employed only for the base metal using 2° /min was a scanning rate, 30° to 100° 2θ range, and CuKα radiation. Another one was subjected to detailed metallographic investigation. Three faces of the sectioned plate were examined. The plates, which were joined by SAW, GMAW, and HPAW were segmented transverse to the weld direction. The sectioned weldments were examined under LOM and SEM.

All metallographic specimens were subjected to a preparation procedure, which includes grinding and polishing. Small specimens were also mounted into Bakelite to eliminate surface skewness.

Macro-etch examinations for structural integrity purposes were done by using 10% Nital reagent after grinding with water-resistant SiC papers, from 80 to 1000,. The cross sections of the weldments were examined to ensure that there is no lack of fusion, inclusion or porosity.

Micro-etch specimens were prepared by grinding with 1600 grade SiC paper and polishing using 3 and 1 μm Diamond colloidal. The specimens were etched with 2% Nital, to observe general structure, and with LaPera reagent to reveal the specific morphologies such as retained austenite. LaPera reagent created a contrast between austenitic and ferritic phases under a light-optical microscope (LOM). No difference in the microstructure was detected by scanning electron microscope (SEM). Thus, it had been tried to observe any morphological differences on un-etched specimens by backscattered imaging methods via SEM.

The grain size measurements were done in accordance with ASTM E112 [63] using LOM and SEM. The elemental differences on different microstructural features at FZ and HAZ were examined by energy dispersive spectroscopy (EDS), in accordance with ASTM E1508 [64].

Post-test metallography was applied to ensure the accuracy of crack propagation direction and its initial machining location. The specimens were sectioned after CTOD experiments at temperatures below the DBTT of X70M by using dry ice or liquid nitrogen. The fracture surfaces have almost shiny surfaces, which is helpful for determining the accurate crack sizes and revealing any non-observable impurities inside the broken surfaces. The fracture surfaces were segmented for crack measurements and fractographic evaluation. The schematic view of the sectioning plan for post-test metallography can be seen in Figure 43.
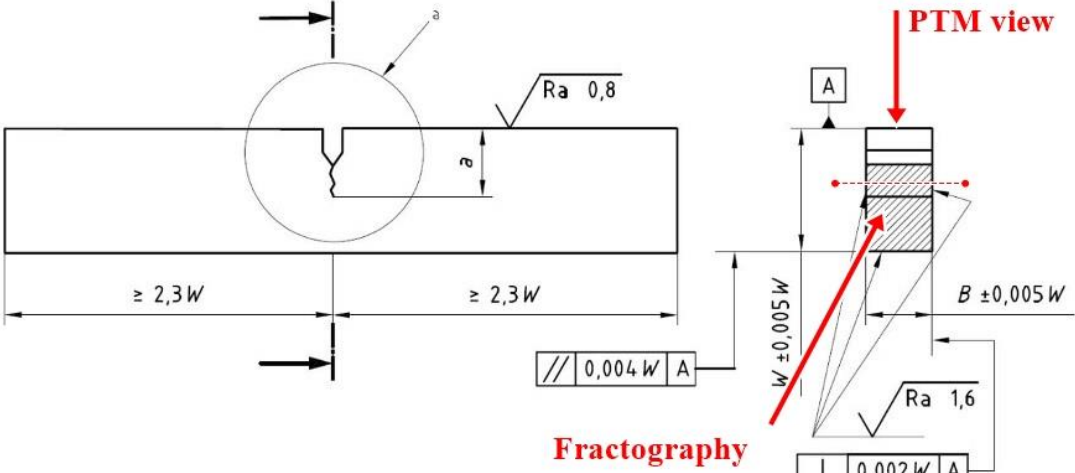
Figure 43. Schematic view of the specimen sectioning plan for further investigations.

Fractography was employed to reveal the microstructural reasons behind the toughness variations. The metallographic preparation steps were grinding, with different grade SiC papers from 80 to 1600, and polishing, with 1 μm Diamond colloidal. Some specimens were etched by 2%Nital to see different microstructural constituents along the fatigue pre-crack direction and the fracture surfaces.

CHAPTER 4

RESULTS AND DISCUSSION

4.1. Welding Process Optimization and Procedure Qualification

Crack propagation resistance of a welded material depends on integrity of the weldment, as well as its microstructural condition. Welding process parameters play a significant role in determining the integrity (soundness) of the joint. The first goal of this study is to set near optimal settings for the welding process parameters in HPAW, which had not employed before to weld thermomechanically rolled HSLA steels. During the study, set of dimensional values of welding form and discontinuities that are addressed by an international standard were taken as the reference of the sufficiently sound weld joint. Once ranges of the parameters that yield sufficiently sound weld joints were determined, the parameters were then optimized more precisely to get the best weld heat input, which would provide the optimum microstructure in terms of fracture toughness.

The standard ISO 5817 [65] provides quality levels of imperfections in arc-welded joints in steel, nickel and titanium alloys. Three quality levels, which are designated by alphabetic codes B, C and D, are referred for tolerances of imperfection geometries. These quality levels provide three sets of dimensional values from which a selection can be made for a particular application. The choice of the quality level for any application, on the one hand, should take account of design considerations, e.g. mode of stressing and other service conditions. On the other hand, productivity factors are also considered, such as time and cost of the process, inspection, and testing of the as-welded assembly, repairs and reworks.

Table 10. Limits for some imperfections according to ISO 5817 [65].

#	ISO 6520-1	Imperfection	Limits for imperfections for quality level B
1. Surface imperfections			
1.1	100	Crack	Not permitted
1.2	104	Crater crack	Not permitted
1.5	401	Lack of (incomplete) fusion	Not permitted
1.6	4021	Incomplete root penetration	Not permitted
1.7	5011	Undercut	Not permitted
1.14	509	Sagging	Not permitted
	511	Incompletely filled groove	Short imperfections: $h \leq 0,05\ t$ but max. 0,5 mm
2. Volumetric imperfections			
2.1	100	Cracks	Not permitted
2.2	1001	Microcracks	Acceptance depends on type of parent metal with particular reference to crack sensitivity
2.3	2011	Porosity	$d \leq 0,2\ s$, but max. 3 mm $d \leq 0,2\ a$, but max. 3 mm
2.12	4011	Lack of side wall fusion	Not permitted
	4012	Lack of inter-run fusion	Not permitted
	4013	Lack of root fusion	Not permitted

Quality level B corresponds to the highest requirement on the finished weld. Therefore, the level B is generally addressed for the qualification of welding procedures. Imperfections are quoted in terms of their actual dimensions (

Table 10).

Linear or crater cracks, porosity, elongated cavities, wormholes, solid inclusions, lack of (incomplete) fusion, lack of (incomplete) penetration, undercut, excess or incomplete weld metal and overlap are considered to be typical weld imperfections (Figure 44). Their detection and evaluation may require the use of one or more NDT methods.
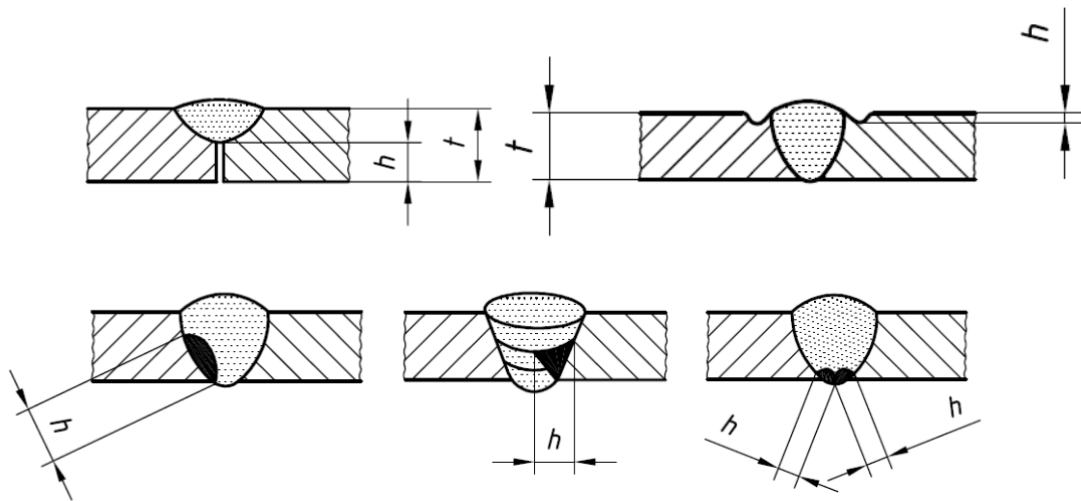
Figure 44. Weld imperfections that were mostly observed during the work.

The welding parameters including weld bevel design had been adjusted based on the experimental results. Before deciding the optimum parameters for each case, the wire feeding speed, linear welding speed, power, corresponding heat input, weld bevel configurations, the diameter of the plasma nozzle, gases and their flow rates were controlled in accordance with EN 10025-1 [66], and the steel grade S235JR for conformity.
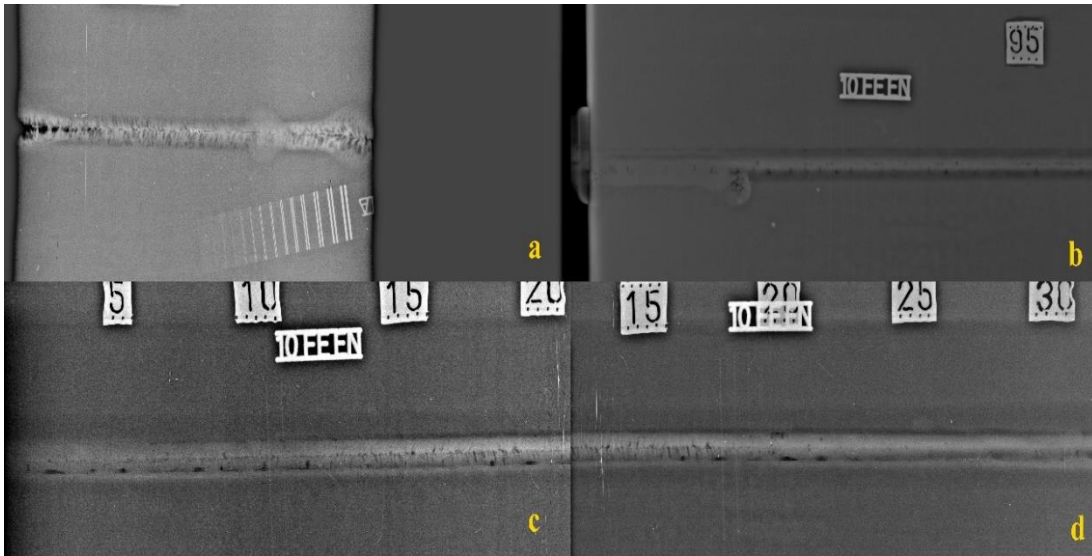
Figure 45. Examples of the lack of fusion problem in the preliminary welds done for process optimization.

During single-side welding operations in the laboratory, the square-butt joint was preferred for HPA and bevel-groove (bevel angle 45°) was preferred for GMA to be able to place the notches properly in the CGHAZ of the CVN and CTOD specimens. WFS was then calculated according to the volume to be filled. Under a constant potential, arc length and WFS determine the arc current amplitude through Ohm relation. As WFS increases and arc length decreases, the current amplitude increases. This yields better side-wall and through-thickness penetrations. Heat inputs were estimated to be 1.4 and 1.0 kJ/mm for the HPAW and GMAW passes, respectively.

Process optimization for double-side welding was more challenging than that for single-side welding. Bevel angle and root face were optimized to 15° and 3.0 (± 1.0) mm for joining of 16 mm-thick plates for both HPAW and SAW operations. The root gap was kept as 0.0 (+ 0.5) mm for SAW due to its high power whereas 1.5 (± 0.2) mm root gap provided the best root penetration for HPAW operations (Figure 15). Heat inputs 1.78, 0.96 and 1.05 kJ/mm were recorded during SAW and HPAW operations with two different wire electrodes, respectively.

In addition to NDT, macro-examination, transverse (cross-weld) tensile and bending tests were carried out to check the soundness of the weldments. The imperfections were recorded and also marked by digital imaging software. Imperfections that were not visible were revealed after bending and tensile tests. The weldments that satisfied ISO 5817 [65] Class B requirements were sectioned for hardness, all-weld tensile and fracture toughness tests (Figure 46).
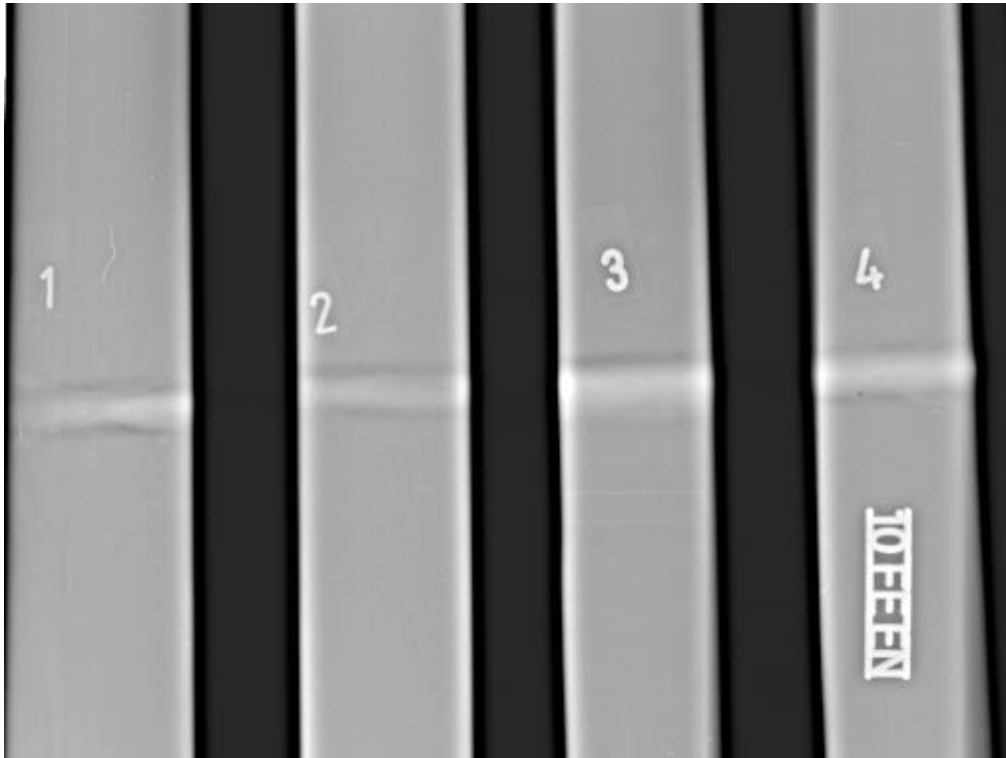
Figure 46. Radiographies of some CTOD testing specimens.

Transverse tensile test specimens, 16x20x200 (t x w x l; mm^3) were tested to ensure the structural integrity of weldments. No imperfections were detected on SL, HS and HC coded 16mm-thick weldments. The results also showed that the tensile strength of the fusion zones is higher than that of the base metal. Moreover, the face bend specimens, which have dimensions of 13x16x200 (t x w x l; mm^3), were tested to reveal sub-surface imperfections. There was no major defect in accordance with API 1104 [51] although some sub-mm imperfections were found at the bevel walls of the HL coded sample series.

Recently, some non-conventional parameter optimization methods have been developed for welding applications. These methods are applied to optimize the input parameters by considering multiple output variables simultaneously. They are supplied by algorithms, which can resolve the mathematical model and select the optimum welding conditions over a wide search space by conducting relatively a smaller number of experiments. Shao et.al. [67] presented a parameter optimization method that employed a multi-objective particle swarm optimization (MOPSO) algorithm to design reasonable values of gas metal arc welding parameters and sequences of Q345D T-joints. Saha et.al. [68] utilized Taguchi's (L25) orthogonal array to perform the trial runs, then a comparative methodology was followed in between two multi-objective hybrid techniques TOPSIS-PCA (a technique for order preference by similarity to the ideal solution - principal component analysis) and TOPSIS-AHP (Analytical hierarchy process). Cao et.al. [69] developed another hybrid methodology by combining radial basis function neural network (RBFNN) and genetic algorithm (GA) to optimize external magnetic field supported Laser welding parameters with respect to the weld bead appearance. Response surface methodology (RSM) [70] and grey relational analysis (GRA) [71-74] have also been used for such process optimizations.

HPAW is a keyhole based hybrid welding technique where two arcs melt the parent metal and the filler metal simultaneously. Process variables such as arc current amplitudes and potentials interact during the operation. Therefore, it is hard to determine their individual effects on weld pool convections and parent to filler metal dilution, consequently the macrostructure and microstructure of the as-welded material. Nonetheless, the studies above consider lean response parameters like weld bead width, depth of penetration, reinforcement and heat affected zone (HAZ) width. Adapting a process optimization algorithm was experienced as complicated for such a complex hybrid welding technique and present response parameter set. Since that, a workmanship - and iteration - based methodology was followed to determine near optimum process parameters where capabilities of the welding manipulator and the

welding power supply unit, the diameter of the filler wire diameter and thickness of the plates were constraints. Spiral welding during line-pipe fabrication and circumferential girth welding in construction field were referred for weld beveling during laboratory works. Double-V groove bevel is preferred in fabrication since it provides high geometrical tolerance to high power and high speed welding operations, whereas narrow-gap welding is preferred for girth welding in construction field where beveling and welding power can be controlled more precisely.

HPAW process variables are listed below and their representations are given in Figure 47:

- Weld bevel parameters;
    - (Root) gap (spacing between the workpieces to be joined) in mm, a,
    - Root face (the face at the edge the workpiece without beveling) in mm, b
    - Bevel angle in degrees, α, and
- Welding parameters;
    - Plasma arc parameters;
        - Stand-off distance (between the plasma nozzle and the workpiece) in mm, S,
        - Arc current amplitude in A, Ip,
        - Arc potential in V, Up,
    - Gas metal arc parameters;
        - Wire feeding speed in m/min, WFS, as independent variable, and
        - Wire arc current amplitude in A, Ig, as a variable that depends on the WFS,
        - Wire arc potential in V, Ug, and

    - Common parameters;

- Level of magnetic shielding between the plasma and the wire arcs (a relative quantity),

- Linear welding speed in mm/min, LWS.
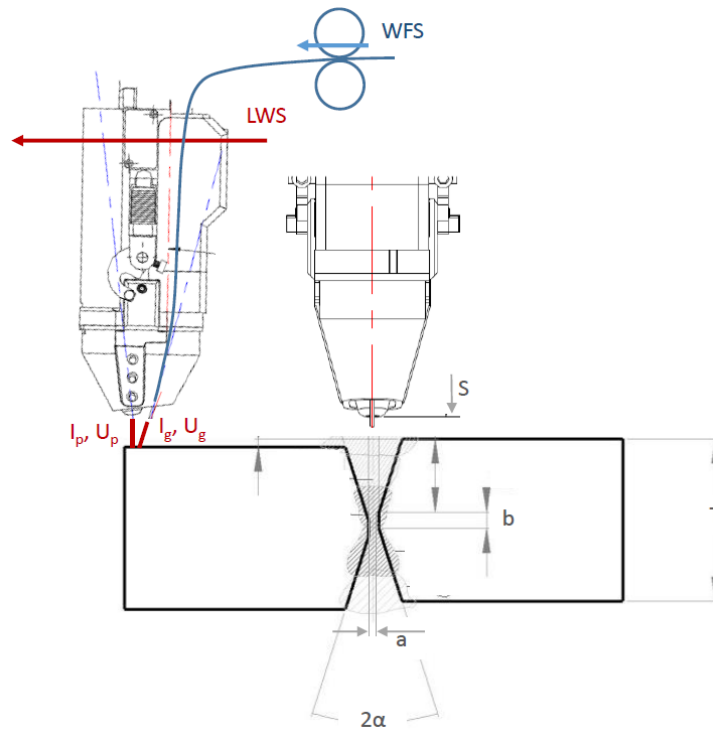
Figure 47. Representation of process variables in HPAW.

Weld bevel parameters were set according to the conventional fabrication and construction applications, and the bevel angles were set as straight as possible to let the notches on the CTOD testing specimens cover the HAZ throughout the thickness. Therefore the bevel angle was set to 0° for single-side welding of 12 mm-thick plates and to 15° for welding operations on 16 mm-thick plates from both sides.

The stand-off distance was set to $3 - 4$ mm in accordance with the previous experiences on other materials. Plasma arc potential and wire arc current amplitude are dependent variables that are controlled by the plasma arc current amplitude and the stand-off distance, and the WFS and wire arc potential, respectively. WFS was

set according to the groove volume to be filled up by filler wire at a specific LWS, and LWS was set in accordance with the conventional use of SAW and GMAW.

Consequently, plasma arc current amplitude and wire arc potential were studied as independent and WFS, root gap and root face were examined as dependent process variables in this present work. Three matrices were constructed and analyzed during the process optimization effort (Table 8).
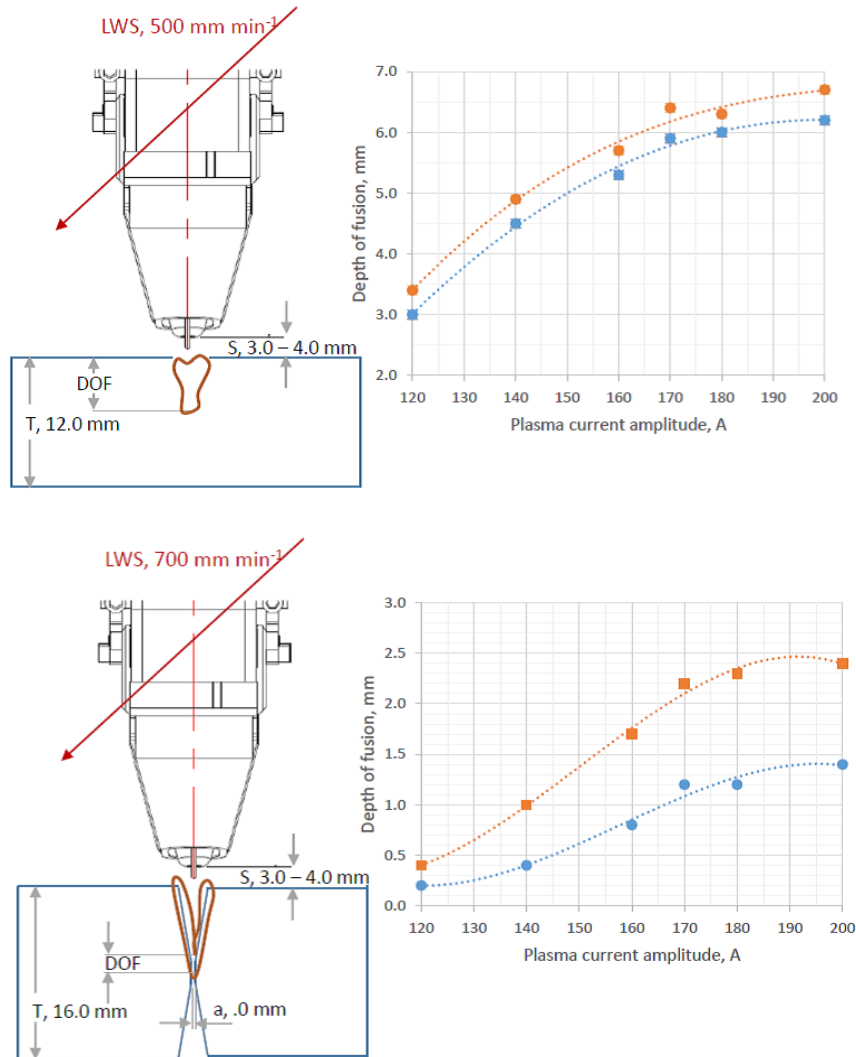
Figure 48. The depth of fusion (DOF) in mm with respect to LWS and I_p, and without root gap.

The first matrix was employed for analysis of the correlation between the plasma arc current and its fusing capability under a specific LWS, which was 500 mm/min for single-side welding of 12 mm-thick plates and 700 mm/min for welding of 16 mm-thick plates from both sides. The depth of fusion with a sufficient side-wall fusion was assumed to be the response parameter of the process. The content of the matrix was then analyzed, and it was concluded that depth of fusion did not significantly change with plasma arc current amplitudes more than 170 A (Figure 48). The amplitudes more than 170 A were employed if higher heat inputs were required for lower cooling rates and consequently better HAZ microstructure.

The plasma arc stability was then examined with respect to the root gap under constant plasma current amplitude, 170 A, and LWS, 500 mm/min. As it can be seen in Figure 49 that, the wider root gap the deeper the fusion up to the root gap of 1.5 – 1.6 mm. However, plasma arc was observed to become unstable with wider spacing between the work pieces.

Once the bevel geometries for the best arc stability, depth of fusion and filler bridging capability were determined, WFS was examined to get sufficient wire arc current amplitude with the optimum arc length under the optimum arc potential. It was observed that magnetic shielding level, wire arc potential, and WFS were indirect, arc length was direct effects on wire arc current amplitude if a specific LWS and stand-off were applied. Magnetic shielding level affects stabilities of the plasma and the wire arcs. However, its effect on current amplitude was not significant, whereas wire arc length and WFS had the maximum effectiveness factor. Therefore, WFS was set to 12 – 17 m/min for welding operations that provided arc current amplitudes between 350 and 400 A.
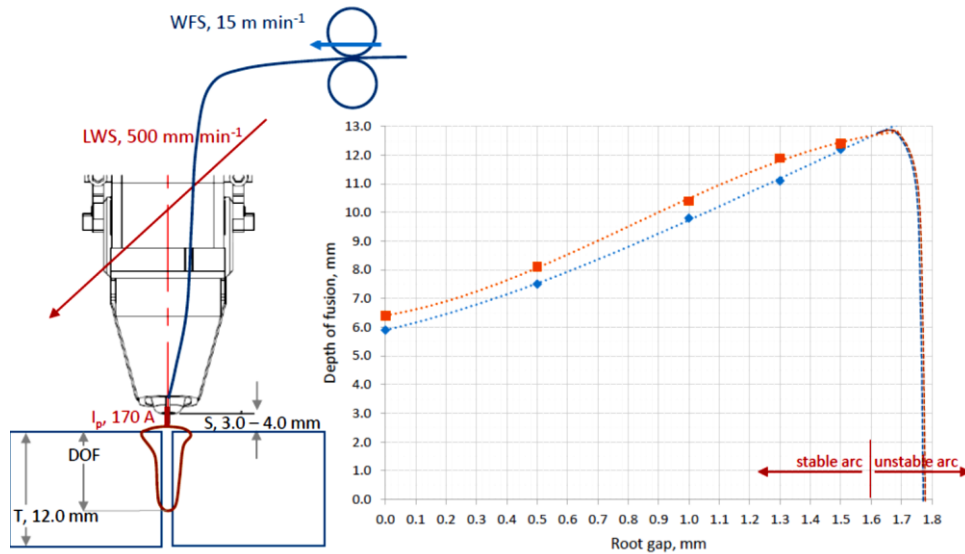
Figure 49. The depth of fusion (DOF) in mm with respect to the root gap, a, with LWS of 500 mm/min.

The purpose of HPAW versus GMAW comparison was to investigate the effect of secondary phases in ICCGHAZ on crack propagation resistance of as-welded X70M line pipe steels (Section 4.3.). Fracture toughness of the as-welded X70M, which was free from IRCGHAZ and welded with moderate heat inputs in a single pass, had never been investigated before. Employing HPAW in the present work, 12 mm-thick X70M plates could be joined in a single pass, in other words without reheating the HAZ.
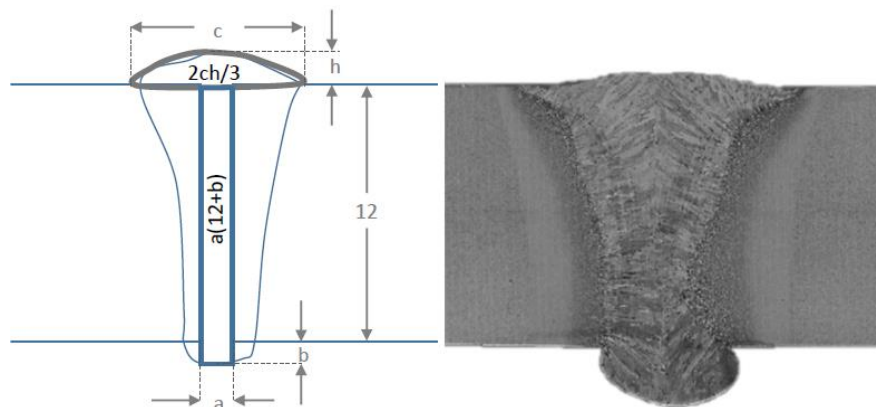
Figure 50. Weld bead parameters in single-pass HPA weldment and calculation of the cross-sectional area.

81

GMAW is usually operated with LWS of 30 – 60 cm/min in partly mechanized applications. Therefore, LWS was selected to be 50 cm/min for HPAW and 40 cm/min for GMAW operations in the laboratory. The cross-sectional area of the weld bead was separated into the area of the groove opening, A_1, and the reinforcement, A_2 (Figure 50) and the total area was calculated as 26 mm^2. When LWS was set to 50 cm/min, WFS was then calculated as 12 m/min for 1.5 mm groove opening. However, this WFS, even with short arc lengths, yielded arc current amplitude of maximum 350 A, which was insufficient to get full-penetration joints. Therefore, WFS was gradually increased until arc current reached to 400 A and full-penetration was obtained.

After single-side and single-pass HPAW applications on 12 mm-thick plates, HPAW parameters were optimized for joining of 16 mm-thick plates from both sides and one pass at each side. The WFS was set to a parameter that would provide sufficient bridging and reinforcement in the weld section.

4.2. As-welded X70M

4.2.1. The Parent Metal

The banded structure was detected in SEM and optical micrographs of the L-S plane specimens of the parent metal. Detailed microstructural investigations showed that there were morphological formations, namely acicular ferrite, polygonal ferrite, globular bainite, and few pearlite (Figure 51 and Figure 52).
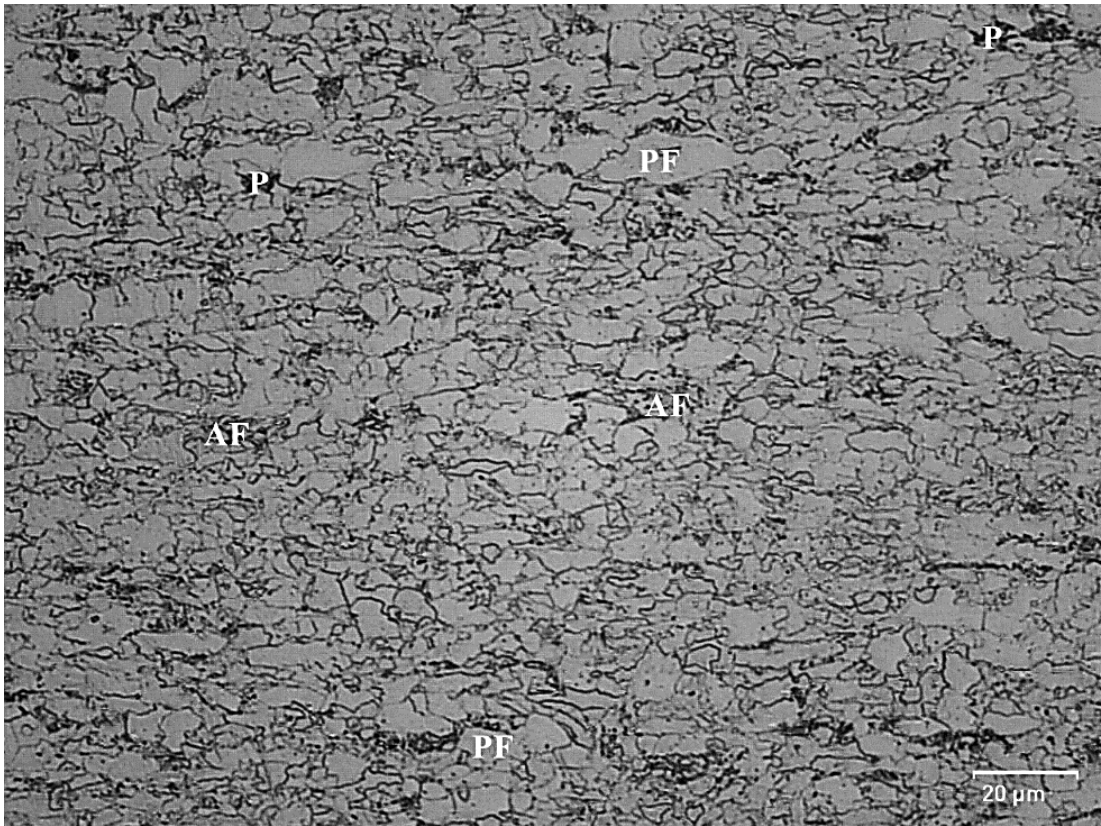
Figure 51. LOM micrograph of the base metal. (AF: acicular ferrite, PF: polygonal ferrite, P: pearlite).
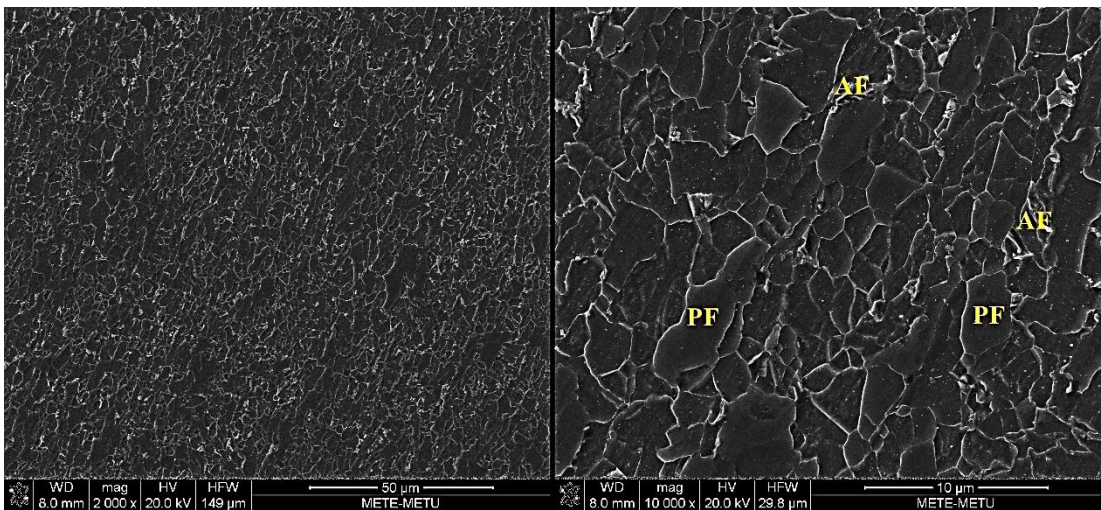
Figure 52. SEM micrographs of the base metal. (AF: acicular ferrite, PF: polygonal ferrite).

The ductile-to-brittle transition behavior of the base metal had been investigated at the target temperatures, which were chosen using the available DBTT data and real service/design temperature. The testing temperatures below -30 °C were set using dry ice and Isopropyl alcohol. The impact toughness values of the parent metal samples satisfied the API 5L requirements.
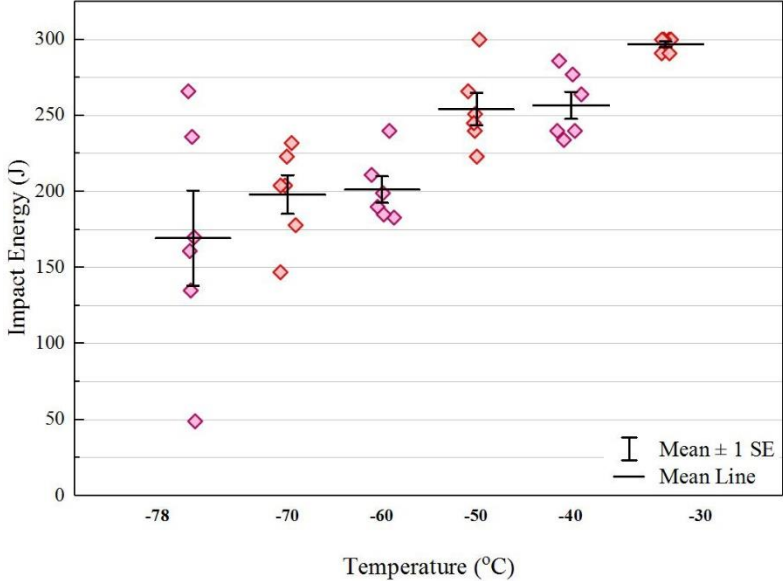
Figure 53. Variation of the impact energy with temperature.

Parent metal CTOD tests were conducted using the B-2B specimens having the cross-section dimensions of 17mm x 34mm. The average δ_{17} of the seven base metal specimens was found as 0.980 mm with 0.073 mm standard deviation at the testing temperature that was -10°C. All specimens presented M-type curves, and they were tested at a speed of 0.6 mm/min.

4.2.2. Kinetics of Microstructural Alterations

Heat Transfer and Cooling Rate

Heat transfer is the basis of all heat included engineering applications. Almost all material properties are changed according to the distribution of existing heat. Heat is introduced by the arc of the welding process to the material to be welded.

The heat transfer through the material might occur by conduction, convection, and radiation. The heat energy, is transferred to a material with molecular agitation by conduction. The transfer rate varies according to the thermal conductivities of the materials. Convection is a combination of fluid motion and conduction simultaneously in which heat is transferred from a fluid (liquid or gas) to a solid surface. The heat can be transferred by radiation, in the infrared region, via electromagnetic wave emission.

The as-welded microstructure is governed by cooling rate during solidification process and subsequent eutectoid transformation. The cooling rate is directly related to the heat transfer phenomenon, which can be analyzed with respect to; the material and the process. Material specific factors would be heat transfer coefficient of the material and its dimensions, whereas process specific factors are pre-heating before welding process, welding power, power density, arc transfer efficiency and linear welding speed (LWS).

Heat transfer coefficient of the material mainly affects the thermal conductivity. The cooling rate increases with higher heat transfer coefficients. The material can remove the specifically induced heat quickly by convection, conduction, and radiation due to low thermal resistance. Dimensions of the material affect the cooling rate in terms of two (2-D) versus three (3-D) dimensional (Figure 54). As material's thickness with

respect to the penetration depth increases, conductive heat flow through the material shifts from 2-D to 3-D, and therefore the cooling rate increases. In laboratory fabrications, two dimensional cooling regimes were observed in the single-pass welded HL specimen and three dimensional cooling regimes were observed in all of the multi-pass welded specimens (Figure 54).
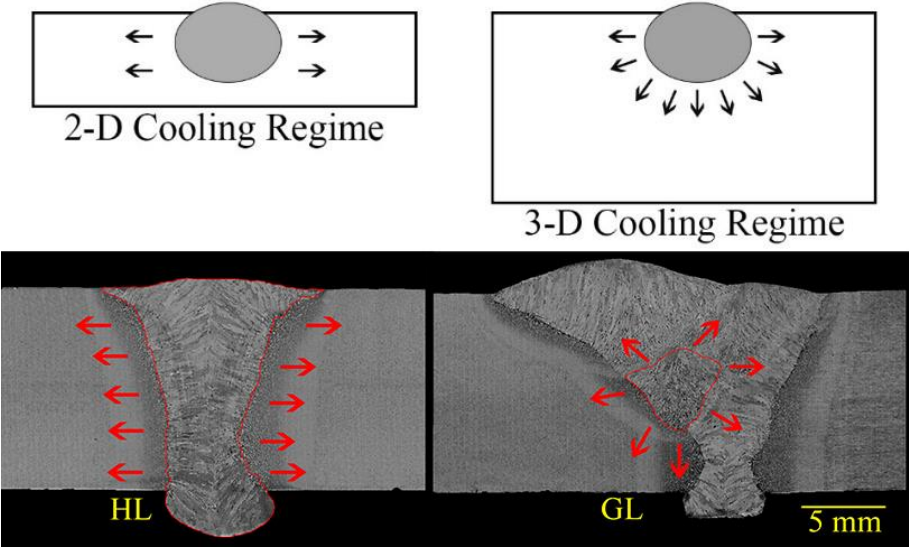
Figure 54. Two- and three-dimensional cooling regimes in HL and GL specimens.

Heat transfer coefficient variations dependent on material were eliminated using the same steel sheets in laboratory fabrications. Only the thicknesses of the X70M plates were different from each other. The 12-mm thick GL weldment has 3-dimensional cooling regimes compared to 12-mm thick HL weldments. The single-pass HL weldments cooled more slowly compered to GL as seen in Figure 54. The cooling effect was revealed by measuring HAZ length and analyzing microstructural constituents. The grain sizes in CGHAZ of the GL weldment are higher than those of the HL weldments.

Assuming the power densities of conventional arc welding techniques are comparable, welding power, arc transfer efficiency and linear welding speed (LWS) are the parameters of heat input definition. Welding power is the product of current

amplitude and potential of the welding arc. The shielding flux in powder form guarantees the arc stability at high current amplitudes. Therefore relatively higher current amplitudes and consequently higher welding powers can be employed during SAW operations. The applied powers are 1.4 and 1.0 kJ/mm for HPAW (HL) and GMAW (GL) operations respectively. Although the welding power in HPAW is lower than GMAW, a deeper penetration was obtained due to the design of HPAW technique, in which PA partially melted the side wall of the coupons. Therefore, 12mm penetration depth can be obtained in the key-hole based HPAW technique, by introducing a heat of 1.4 kJ/mm in a single-pass. However, the same thickness could not be filled by GMAW method due to its lower power density. The same situation is also valid for SAW and HPAW. On the one hand, melt-in welding technique, power density of sub-merged arc is most also high. On the other hand, the flux used generally causes weld pool convection from side to the weld center as in the weld pool obtained by HPAW. Nevertheless, SAW utilize very high power. Therefore, depth of penetration by SAW is comparable to the penetrations that are obtained during HPAW.

Not only welding power but also LWS determines the depth of penetration. The combination of power and LWS yields the definition of line energy or nominal heat input. Involving the arc transfer efficiency, the effective (real) heat input can also be calculated. The arc transfer efficiency of SAW is considered as unity since the arc exists under a flux powder. Heat loss due to convective and radiative heat flow is assumed to be negligible as compared to the open arc welding techniques, such as GMAW and HPAW.

The cooling rate is sensitive to the welding power, LWS, and corresponding heat input. The cooling rate decreases as the heat input increases in each weldment (Figure 55a). The cooling rates in laboratory fabrication were assumed in accordance with the measured and modelled behavior of welded X70 line pipe steel by Cutelnıcu et al. and Kou et al. [75, 76]. The assumed coolling rates stated that the joined SL, HS and HC coupons with a linear welding speed.of 700 mm/min cause a strong

decrease in cooling rates compared to HL and GL coupons. These two coupons were joined with a speed of 400 and 500 mm/min. The strong decrease in cooling rate increased the amount of LBZs in HAZ. The relative MA amount in two-sided SL, HS and HC weldments are directly matched with the literature data, proposed by Zhu et al.[77]. The cooling rate variations can be represented by $t_{8/5}$. The transformation times between 800 to 500 °C were almost 20 sec and 14 sec for SAW and HPAW operations in the laboratory weldments.

The last process-based effective factor is pre-heat which consists of pre-heating temperature and inter-pass temperature. The optimum pre-heat temperature provides good weldability and an optimum cooling rate (Figure 55b). Inter-pass temperature has an important effect on microstructural formations in FZ and CG HAZ, and the final mechanical properties. For example, higher inter-pass temperature causes an increase in the Charpy V-notch toughness, due to finer microstructural constituents and lower strength of the weld metal. The cooling rate is also affected correspondingly to the chosen inter-pass temperature. The cooling rate becomes too low as it increases. In laboratory weldments, the Tz was set to below 300°C due to the parent metal characteristics. The phase transformations occur in the X70M steel above 500°C and a decrease in cooling rate can not possess detrimental effect on microstructural evolutions. Therefore, controlled inter-pass temperature, in a range of 200 and 250 °C, did not cause variations in microstructure and corresponding mechanical properties in welded specimens.
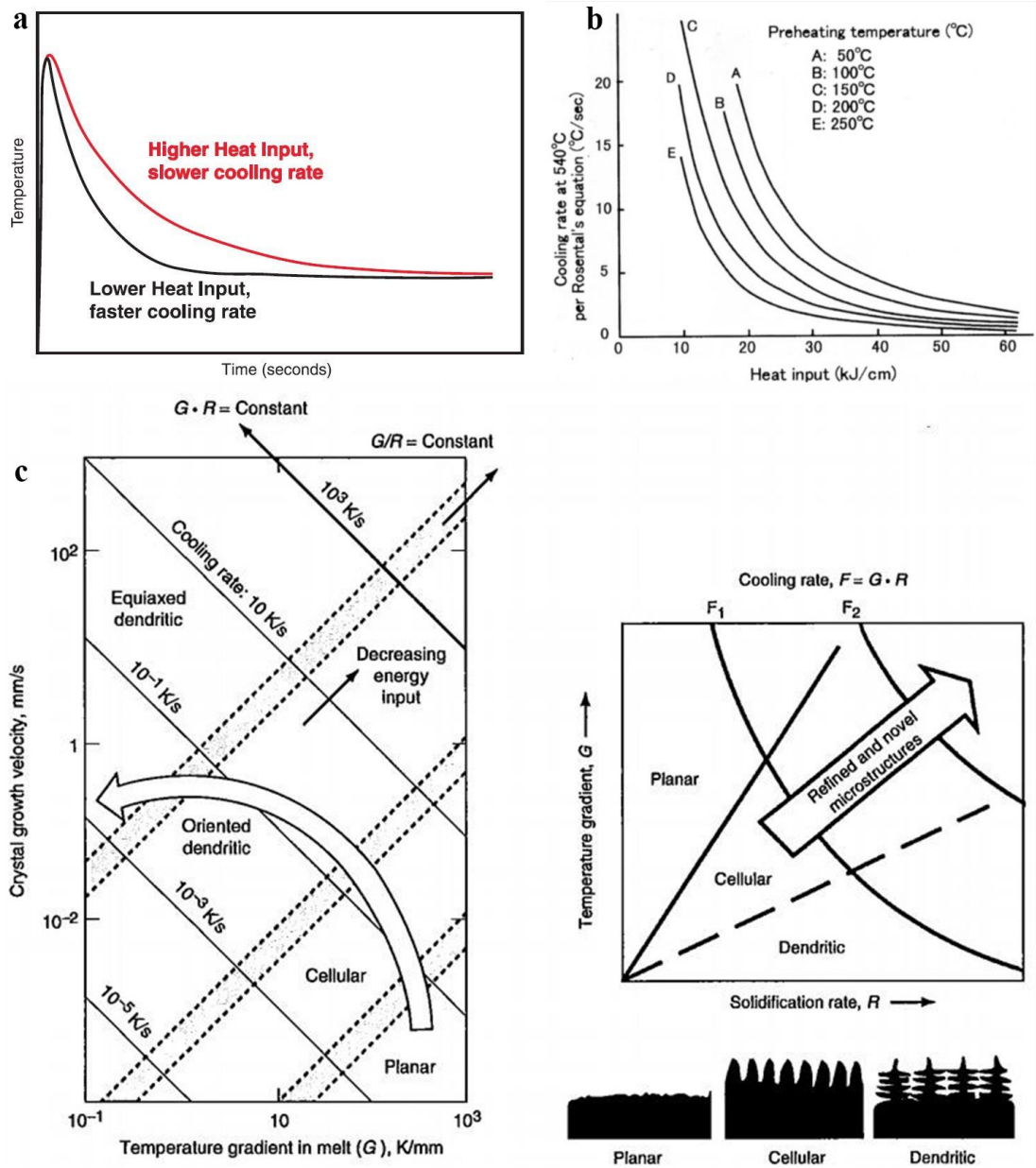
Figure 55. a) Effect of heat input on cooling rate [78]. b) Effect of pre-heating temperature on cooling rate of the 19 mm-thick plates [79]. c) The representation of the effect of the temperature gradient, crystal growth rate, and cooling rate on solidification [80].

The effects of alloying elements on microstructural variations in parent metal are briefly given in Table 2. Elements such as Vanadium, Titanium, Niobium, and Nitrogen lead alterations in microstructure and corresponding mechanical properties. Small amount of vanadium, e.g. 0.1%, promoted second phase and MA formations, and limited acicular and polygonal ferrite formations at lover heat inputs. Although this cause a decrease in toughness of as-welded material, the effective HAZ grain size is decreased by the existence of small amount of vanadium, thus the overall mechanical properties of the material are not altered significantly. The effect of Titanium on the microstructural constituents cannot be observed at small fractions, e.g. 0.02-0.05%, and low heat input. The second phase and MA formations are promoted by Silicon, in a range of 0.1 and 0.5%, Niobium and other secondary phases. Nitrogen also leads a decrease of the MA constituent at low heat input applications.

The introduced effects of alloying elements were investigated in laboratory weldments by LOM and SEM. Additional EDS mapping was employed during micro elemental analysis under SEM. The differences in chemical compositions of the laboratory weldments are given in Table 11. The grain size in as-welded materials decreases as the silicon content increases. The effect of other elements cannot be visualized since the amounts of Ti, Nb and V were almost same.

4.2.3. Solidification Structure and Over-matching

The chemical composition results of the spectral analyses are given in Table 11.

Table 11. Major alloying element constituents in the parent and as-welded metals.
Bolds refer to the maximum permissible values.

	wt %	C	Si	Mn	P	S	Cr	Ni	Mo	Ti	Nb	V
X70M	*Std<*	*.12*	*.45*	*1.70*	*.025*	*.015*	***.50***	***.50***	***.50***		***.15***	
	Lab	*.04*	*.27*	*1.63*	*.006*	*.001*	*.17*	*.10*	*.12*	*.02*	*.06*	*.06*
F8A2-EA2-A4	*Std*	*.05*	*.40*	*1.40*	*.030*	*.030*			*.50*			
	Lab	*.05*	*.37*	*1.38*	*.020*	*.006*	*.08*	*.04*	*.35*	*.01*	*.02*	*.02*
ER70S-6	*Std<*	*.07*	*.95*	*1.68*	*.025*	*.035*	*.15*	*.15*	*.15*			
	Lab	*.08*	*.90*	*1.51*	*.014*	*.014*	*.07*	*.02*	*.01*	*.01*	*.02*	*.01*
E70C-6M	*Std*	*.04*	*.63*	*1.25*	*.030*	*.030*	*.20*	*.50*	*.30*			*.08*
	Lab	*.04*	*.63*	*1.25*	*.010*	*.010*	*.07*	*.35*	*.08*	*.01*	*.02*	*.01*

The effects of elements on weldability and final microstructure were visualized. Consisting relatively higher amounts of Si and C in HS weldment, acicular ferrite formation was observed to be promoted. The HC weldments have better weldability compared to the HS weldments due to the relatively high amount of Ni. Niobium, in SL weldments, advocated ferritic morphologies more than HPA weldments. Almost all ferrite stabilizer elements increased the toughness of the line pipe steel. Therefore, the spectral analysis results supported that all consumables had yielded different microstructural and mechanical characteristics. Microstructure of the parent metal and microstructural variations in fusion zone of as-welded material are represented in three dimensional micrographs (Figure 56).
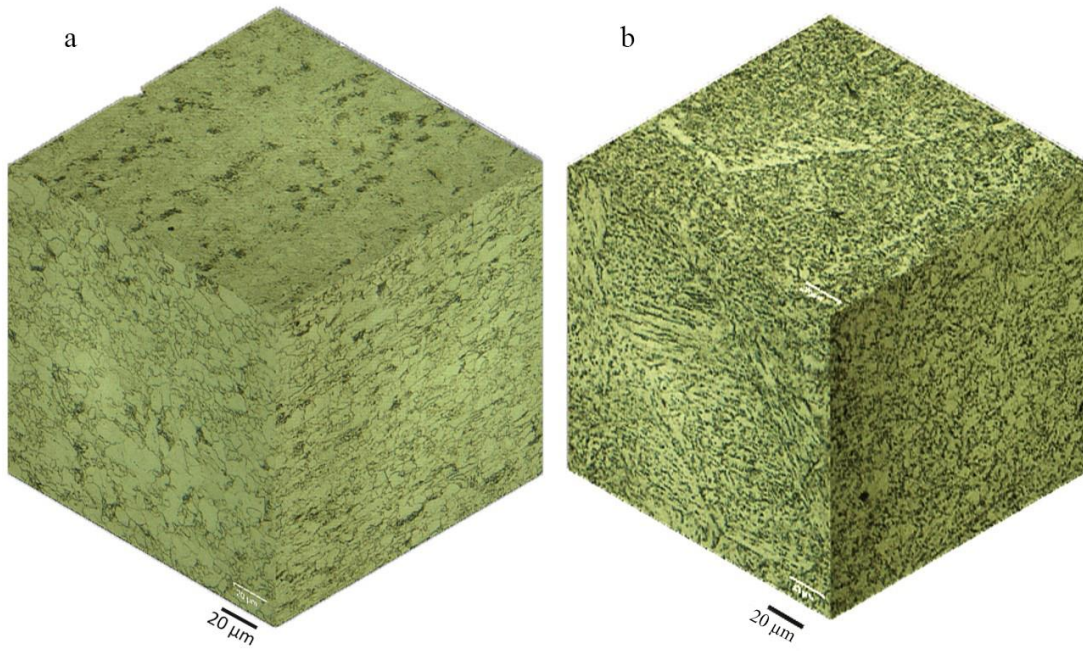
Figure 56. Three dimensional micrographs of a) parent metal and b) as-welded metal (fusion zone).

The alloying elements caused some inclusions during welding operations and their distribution directly affects the morphological and mechanical variations. Titanium - Vanadium – Niobium precipitates lead the formation of fine austenite grains in CGHAZ. One of the HPA weldments includes some inclusions through the FL and the detailed analysis revealed the elemental distributions (Figure 57). Low Silicon, Vanadium, Niobium and Titanium, and high Manganase concentrations were observed in inclusions.
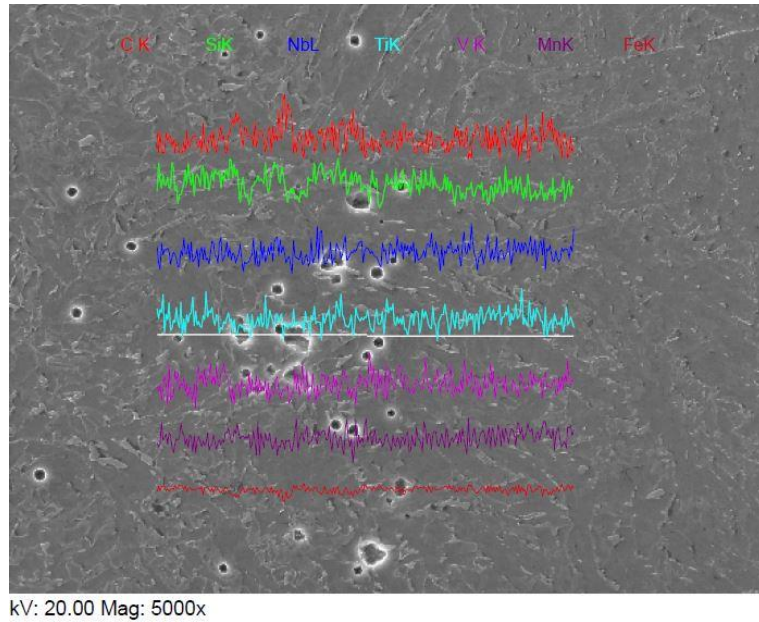
Figure 57. Elemental distributions through the FL of HS weldment.

The weldments, which were examined in terms of integrity and satisfied ISO 5817 Class B requirements, were subjected to tests to determine their hardness and strength properties. Hardness measurements were conducted by nano-, micro- and macro-hardness indentation instruments, CSM NHT nano-indenter, Schimadzu universal micro-indenter and Schimadzu HMV-20 hardness measurement instruments respectively. The hardness variations, in HV10 scale, of HS and HC weldments are given in Figure 58.
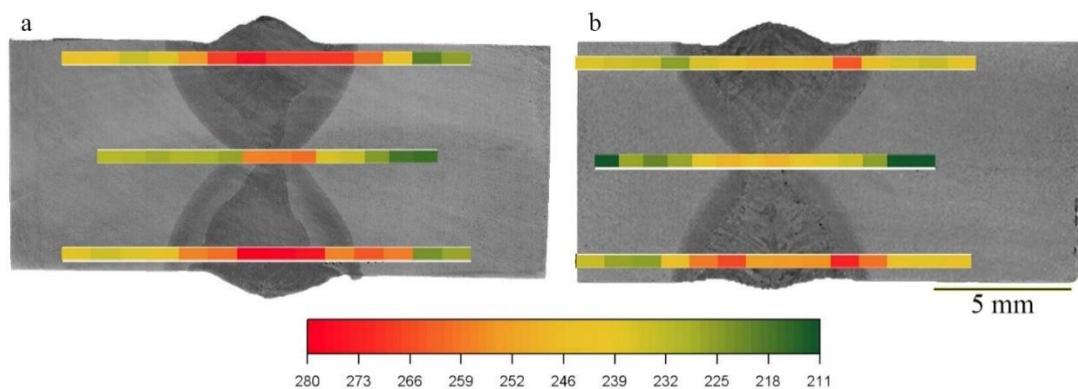
Figure 58. The macro-etched samples of a) HS and b) HC with hardness variations.

Nano-indentation measurements were carried out on the following specimens: FL analysis on the hardness specimens of HL, HAZ analysis on the hardness specimens of HC, and base metal phase analysis on the microstructure evaluation sample of the as-received API 5L X70M plates. The nano-indentation results will be discussed in Section 4.5.

The strength of the materials were investigated by tensile test. The tensile test results are provided in Table 12. The mechanical properties of SL weldments in fusion zone have the highest compatibility with parent metal.

Table 12. Tensile test results of sets of specimens.

	Material / Filler			
	X70M	**X70M** **ER70S-6**	**X70M** **E70C-6M**	**X70M** **F8A2-EA2-A4**
Welding Method	*BM*	*GMAW* *HPAW*	*HPAW*	*SAW*
E (GPa)	205	205	210	203
Rp0.2 (MPa)	582	619	657	603
Rm (MPa)	662	703	729	681
At (%)	21	18	17	22
RA(%)	63	43	26	42

The highest fusion zone strength was obtained by the filler wire, E70C-6M. However, increasing difference between the parent metal and the filler wire caused strong overmatching in terms of strength and ductility. Therefore, larger hardness variations and lower toughness was obtained in HC weldment relatively (Section 4.5.).

4.2.4.   The Heat Affected Zone (HAZ)

HAZ microstructure consists of different morphologies depending upon the welding technique, i.e. multi-pass GMAW, single-pass HPAW, and multi-pass HPAW. Some regions are given in Figure 60. The morphology varies due to the heat input and the cooling rate, which are also supported in sections 4.3., 4.4. and 4.5.

The high heat input caused grain coarsening and HAZ expansion through the base metal. For instance, the heat input of 2.5 kJ/mm is introduced during line pipe fabrications, in the field SA weldments, and the mechanical test results reveal that the average CTOD values of HAZ of the girth welds are lower than 0.2 mm. The following investigations show that high heat input possessed the formation of weakest points, i.e. very coarsened grains and MA formations at the grain boundaries. In other words, the coarsened grains lead to additional phase formations, i.e. upper bainite and MA islands and mechanical property variations in CGHAZ. The toughness of fusion line / HAZ specimens decreased due to the grain coarsening. The micrographs of laboratory- and field-weldments, by SAW, are given in Figure 59. The major difference between SF and SL weldments are the formation of MA at grain boundaries, brighter regions, in CG HAZ.
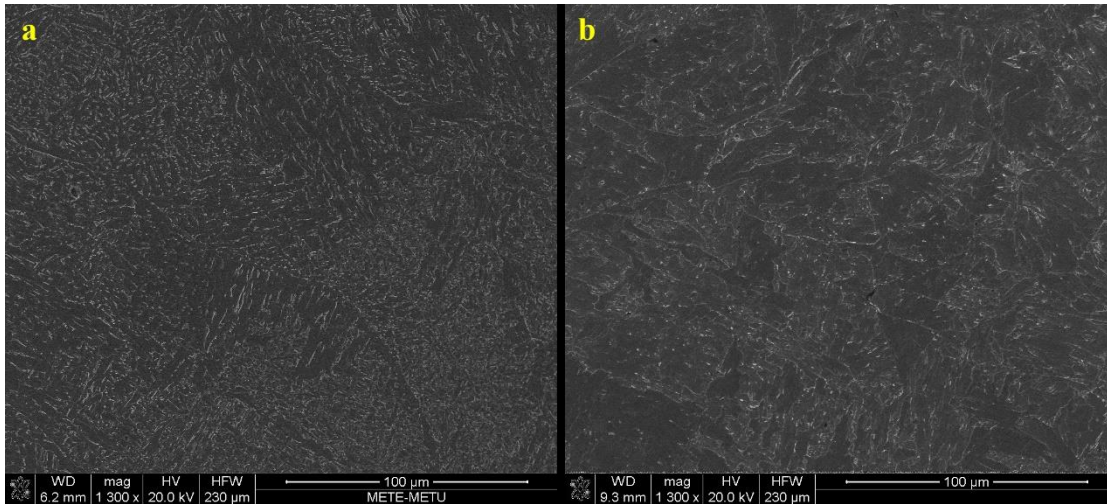
Figure 59. CG HAZ micrographs of different SA weldments. a) SL and b) SF.

The regional analysis according to the shape of morphologies was done in laboratory weldments. The regions in Figure 60 were only observed in multi-pass weldments. The fractions of re-heated HAZ are higher in 12 mm-thick GMA weldments than 16 mm-thick HPA and SA weldments. They include CGHAZ, FGHAZ, ICHAZ, IRCGHAZ, SRCGHAZ, and their tempered formations in HAZ. The identifications of the formations were completed by LOM and SEM. The morphologies and corresponding regions in HAZ were recorded to be used in a part of mechanical tests, such as pre-crack location verification for CVN and CTOD specimens. The marked regions, in IRCGHAZ and CGHAZ, were also used for determining the weakest points along the single-bevel groove weld.
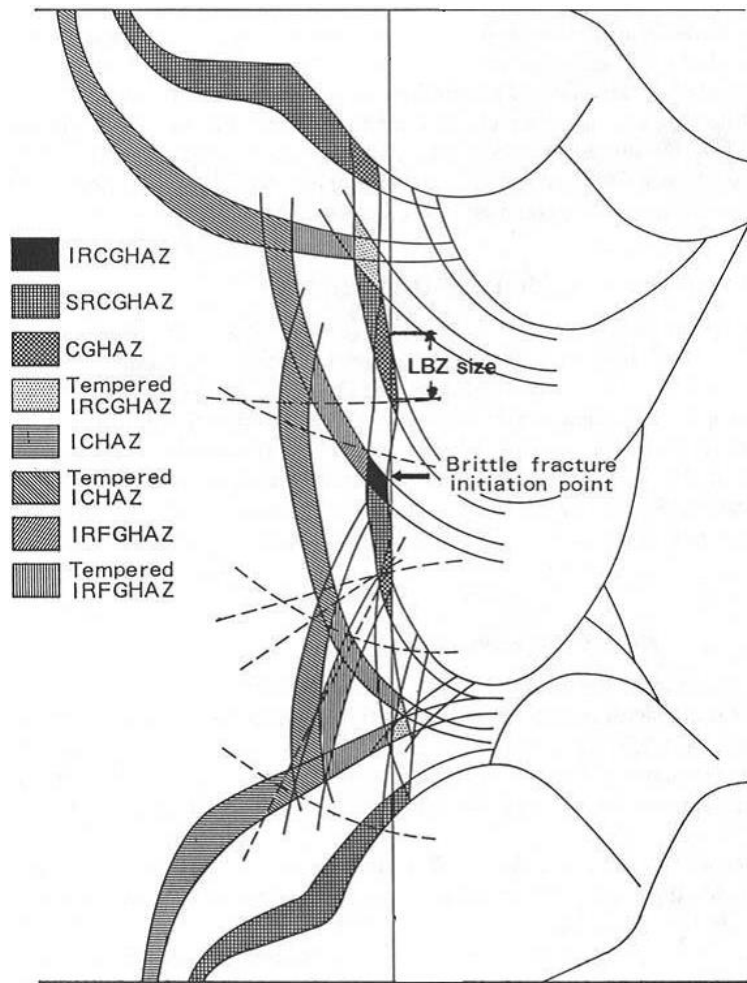
Figure 60. HAZ microstructure in multi-pass weldments [81].

The morphological features were analyzed to find regions, which have detrimental effects on mechanical properties of the material. CGHAZ generally included weakest microstructural formations. For example, local brittle zones were identified in IRCGHAZ by the help of nano-indentation experiments, corresponding results are given in Section 4.5. These regions are formed in the multi-pass weldments due to the secondary heat treatment. The second pass caused MA formations in IRCGHAZ, and the morphologies decreased the material toughness. The effect of the morphologies within IRCGHAZ and CGHAZ are explained in Section 4.5.

Hence, grains are coarsened within HAZ, and relevant toughness decreases. Line energy variations also affect the cooling rate. If the line energy is too high at specific

locations, the weakest points, local hardened and softened zones, are formed due to cooling rate variations. The hardness within high energy induced regions is decreased because of lower cooling rates. To illustrate, the hardness variations, decrease in the region, FZ-HAZ transition, of SL weldment is relatively higher compared to HS and HC weldments.

The microstructure of the parent metal was observed to be altered after welding operations. Applied heat caused a complete change in the microstructure of the fusion line and a part of HAZ, where the material was subjected to temperatures higher than Ac_1. It was also observed that the grain size increased from 8-10 μm to 35-40 μm, as shown in Figure 61.
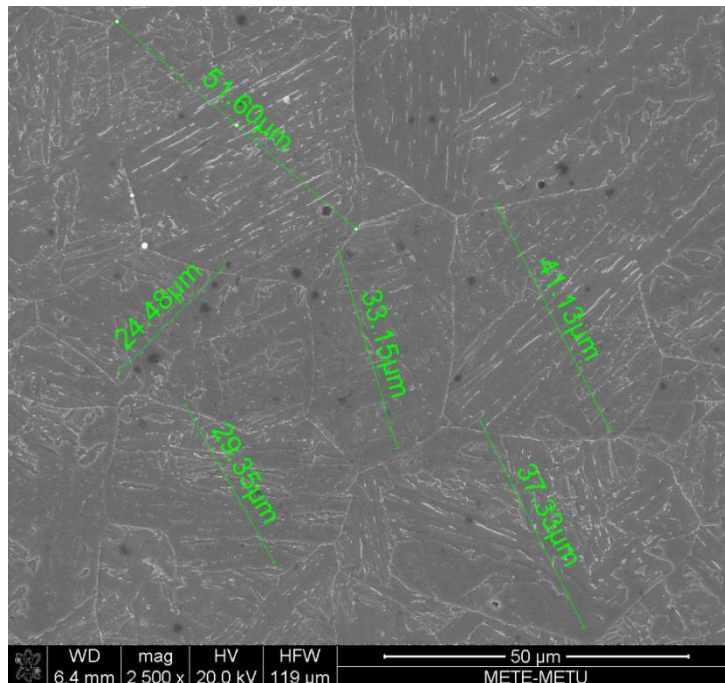
Figure 61. Representative micrographs of the CGHAZ of the SL specimen.

The various morphologies exist in the microstructure after welding, e.g. MA islands with different amounts in the CG HAZ of laboratory weldments. The differences can be noticed in the micrographs of GL and HL weldments (Figure 63).

98

Moreover, the width of the HAZ decreased due to the optimized welding parameters in the order of SA, GMA and HPA welding techniques. The shortest HAZ width was obtained by HPAW due to the lowest heat input and advantage of multi-arc, PA, and GMA. Moreover, these differences caused a decrease in the average grain size at CGHAZ and IRCGHAZ. The smallest grains, with an average size 30 μm, had procured after key-hole based HPAW. The other weldments produced by SA and GMA have average grain sizes of 35 μm and 65 μm at CG HAZ, respectively.

4.3. Single- vs. Multi-pass Welding

12 mm-thick coupons were welded in single- and multi-pass methods by HPAW and GMAW respectively (Figure 62). Same filler wire, SFA/AWS A5.18 ER70S-6, was used. The effect of multi-pass welding was investigated by the help of microstructural evaluations and mechanical tests. The macro view of the specimens shows that the aspect ratio of each weldment is different. HPA weldment has higher aspect ratio than GMA weldment. The calculated ratios are almost 0.5 and 1.4 for HPAW and GMAW respectively (Figure 62).
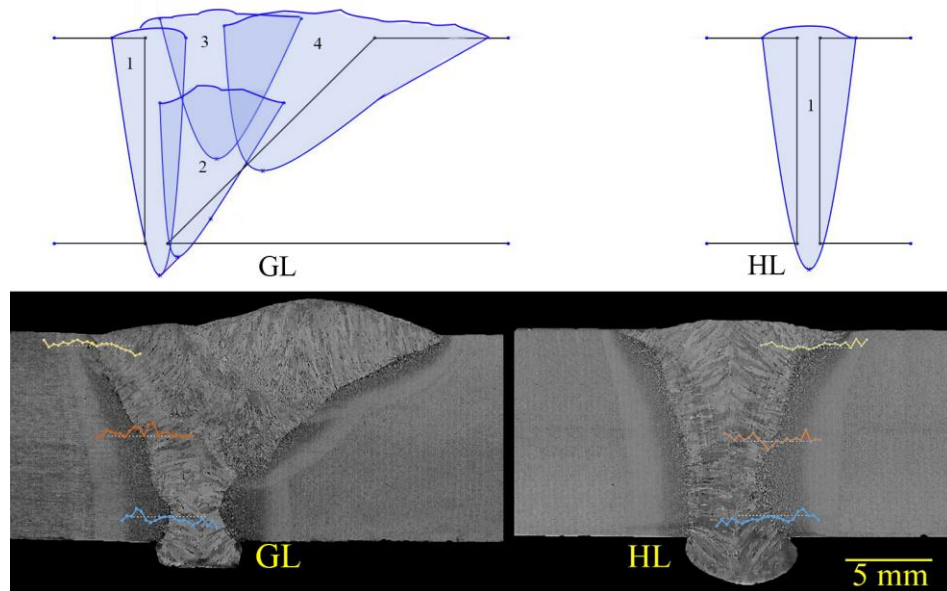
Figure 62. Typical pass sequence and relating macro-etch samples of GL and HL weldments.

Micro-indentations revealed that the hardness change, average value of 255 and 235 Vickers with standard deviations of 12 and 14 Vickers in HL and GL weldments respectively, through the partially melted zone, PMZ, were varied due to the effects of welding. The variations were based on local softening and hardening in this very thin region. The differences in this interval were higher in GL specimens due to the effects of multi-pass welding. On the other hand, the hardness variations at the bottom scanning line are almost same in GL and HL weldments. This similarity is based on the bevel design, in which the weld root is filled by the first weld-pass. The second pass in GL weldment did not affect the mechanical properties of the section which is subjected to micro-indentations.

The microstructural examinations in FZ showed that the solidification structure at the proximity of the successive weld pass was subjected to heat treatment during the multi-pass weld process. The smaller grains were formed at the intersections, and pre-formed dendritic arms were recovered. These microstructural alterations depend on the inter-pass temperature and the initial depth of penetration. The most important parameter for these structural variations was observed to be the inter-pass temperature, T_Z. Although T_Z was set to a temperature that was within the range of 200-250°C during GMAW operation. Local brittle zone (LBZ) and local softening zone in IRCGHAZ could not be eliminated. These zones in CGHAZ due to multi-pass welding yield loss in toughness of the materials. The decrease in toughness values are related with the crack growth behavior of each weldment during CTOD tests. The tests was completed after unstable crack growth in HAZ specimens of GL weldment. The fracture surface analysis under LOM and SEM also showed signs of unstable crack growth. The crack growth could not be slowed down or stopped when they reached LBZs. The fracture surface analysis of HL weldments revealed that the amount of LBZs is lower compared to multi-pass GMA weldments. Therefore, only two of HAZ specimens of the single-pass HL weldments were fractured with existing unstable crack growth. The crack growth in the other specimens were stable and the corresponding CTOD values were higher. The stable crack growth has M-type load (N) vs. CMOD (mm) curves

IRCGHAZ contains secondary phase formations, which could be harder or softer relative to the primary phases. It was observed on fracture surfaces on CTOD specimens that such local hardening and softening zones were the principal reason for pop-ins during CTOD testing. MA phase, as a LBZ, is preferred to be formed at grain boundaries due to the secondary heating by multi-pass welding. Toyoda et al. investigate that such local heterogeneities due to secondary phases have detrimental effects on the fracture behavior of steels. The cooling rates and some of the welding parameters are the sources of the inhomogeneity in the microstructural features and mechanical properties of subjected steels. Toyoda et al. also describe that LBZs are formed at some parts of HAZ, such as IRCGHAZ MA formations are observed within this LBZs [3]. The MA formations are clearly identified by Berkovich nano-indentation during the present work. The results show that MA is formed at grain boundaries of the CGHAZ microstructure and the hardness reached a peak value, 590±75 HVIT, in these regions. The detailed nano-indentation results with micrographs are given in Section 4.5.

In short, the comparison of the toughness values indicates that the multi-pass GMA weldments yield slightly lower toughness results compared to single-pass HPA weldments. The standard deviation in CTOD results is higher in GL specimens compared to HL specimens. The impact toughness variations in HAZ and loading vs. CMOD graphs of each weldment are given in Figure 64 and Figure 65.
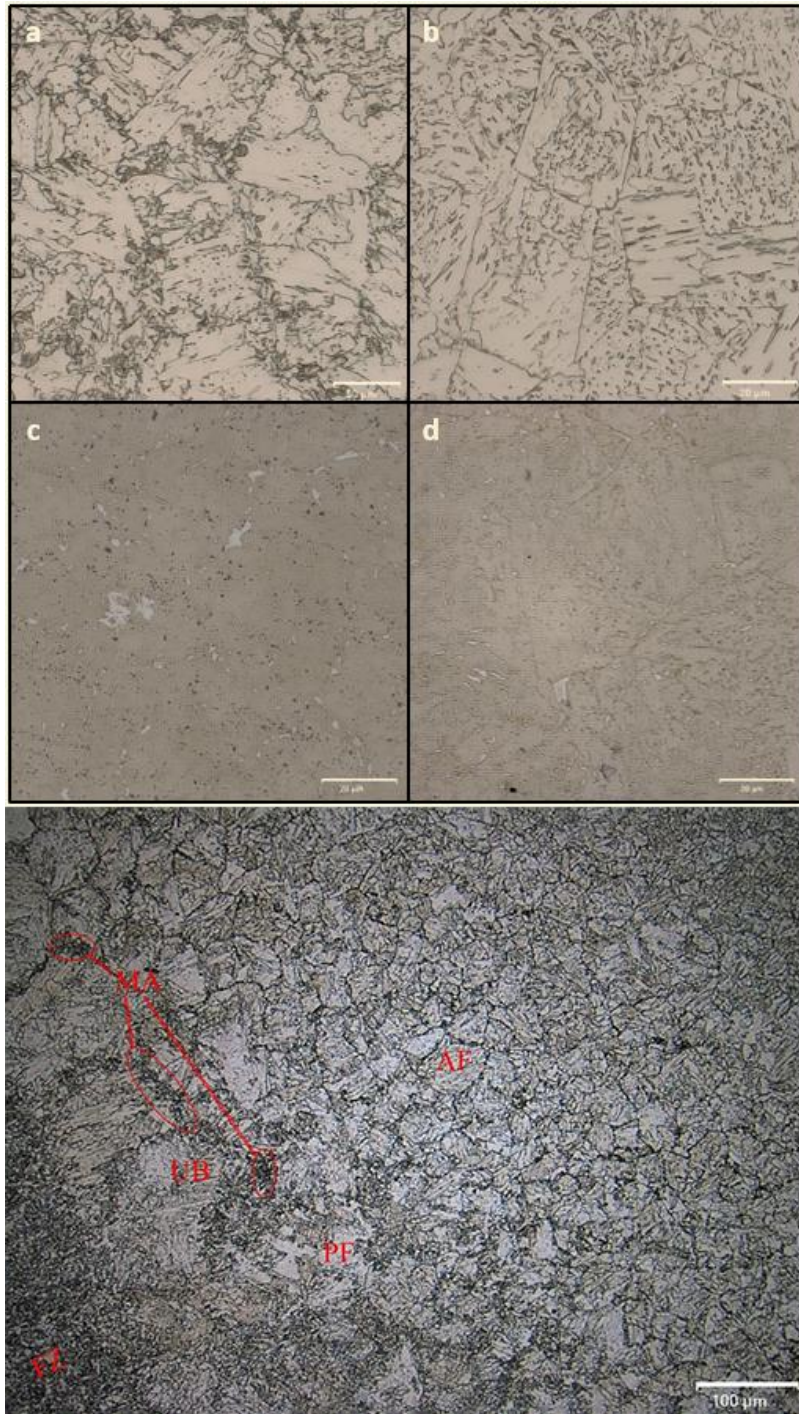
Figure 63. IRCGHAZ microstructures of the GL and HL weldments, column view in a given order. (a and b etched by 2% nital; c and d etched by LaPera). LOM micrograph of GL weldment with observed phases. FZ) fusion zone, and existing phases MA) martensite-austenite island, UB) upper bainite, AF) acicular ferrite, and PF) polygonal ferrite.
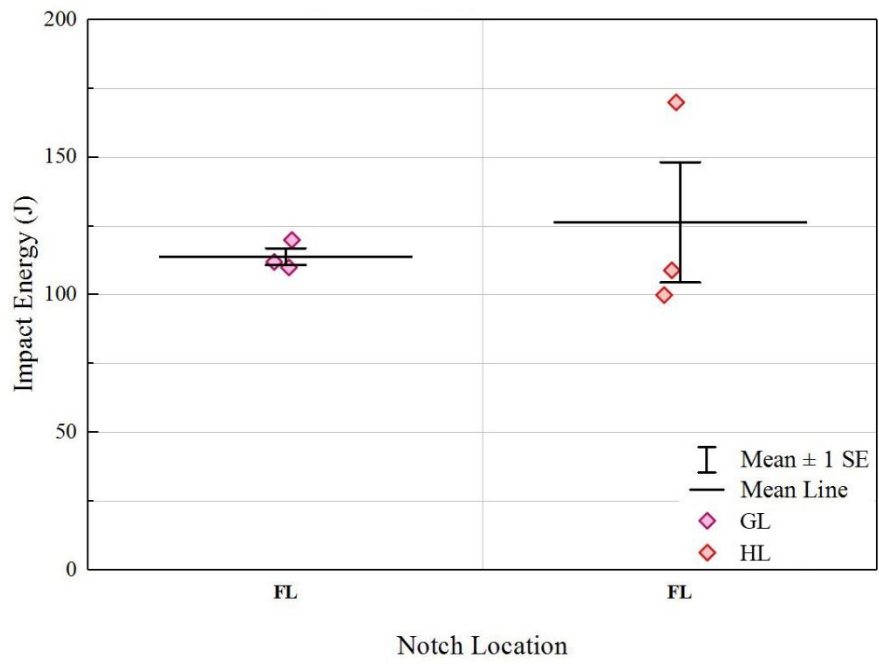
Figure 64. Impact toughness variations of GL and HL specimens.
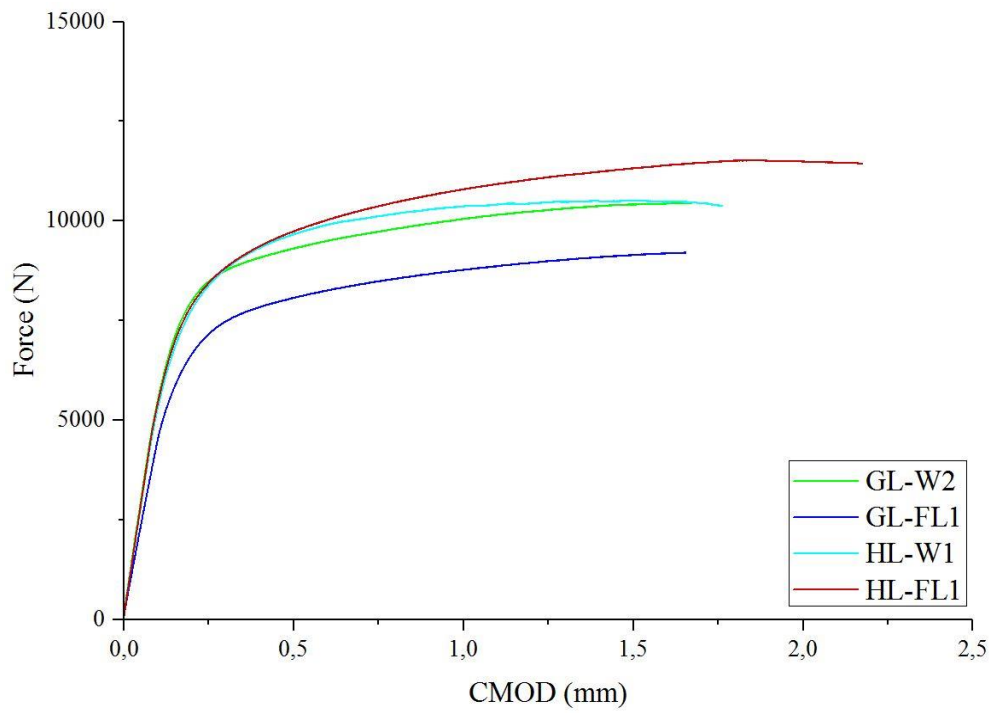
Figure 65. The representative Load vs. CMOD graphs of GL and HL specimens.

The average impact toughness values of each weldment, GL and HL, were 114 and 126 joules with standard deviations 5 and 38 joules respectively. The impact toughness experiment could not reveal any differences due to its macro-level characteristics. The 2 mm-thick notches on specimens were machined with respect to the pre-test markings, which were drawn on specimens after macro-etching. In addition to this small difference in CTOD results, the fracture behavior during the experiments showed that all GL specimens were subjected to unstable crack growth. The reasons for this type of crack growth before failure might be inhomogeneity in HAZ, especially in IRCGHAZ. It was also observed that one of the HAZ specimens of GL coupon had 0.055 mm CTOD value. The lowest value in this weldment showed that the amount of weak points in front of the crack directly decreases the toughness of the material. The crack cannot grow during the experiment and the specimens are subjected to immediate failure. However, half of the HL specimens, in which pre-cracks were located within CGHAZ, reached maximum load values, and stable crack growth was observed. This behavior is due to the prior characteristics of the HPAW. The homogeneous microstructure yields better toughness values in overall.

Further points beyond the differences in single- and multi-pass weldments are given in (Section 4.5.). Comparable results led to investigate the effect of coupon thickness. Therefore, 12 mm- vs. 16 mm-thick plates were joined by HPAW (Section 4.4.).

4.4. Welding from Single Side vs. Both Sides and Coupon Thickness

16 mm-thick line pipe steel plates were joined by the key-hole based HPAW. The optimized weld bevels were machined, and HS weldments were completed using SFA/AWS A5.18 ER70S-6 as a filler wire. Macro-sections of the fabricated coupons are given in Figure 66.
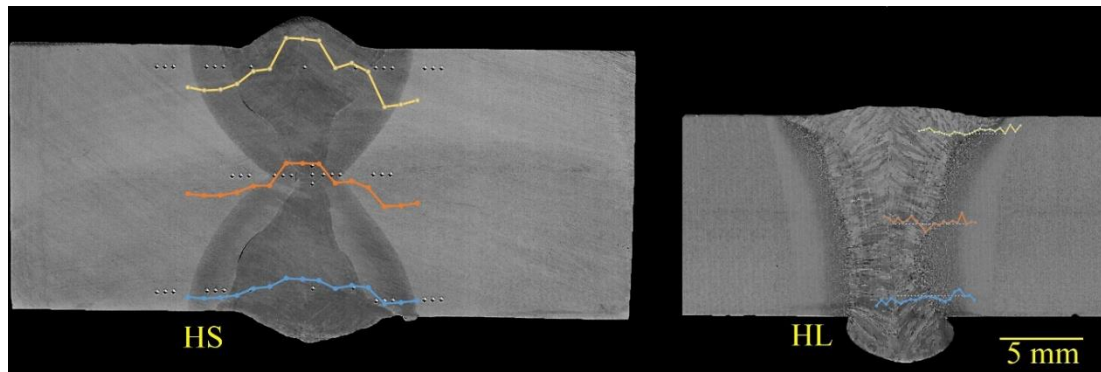
Figure 66. Macro-etch samples of HS and HL weldments with hardness profiles.

The variations in hardness measurements were based on multi-pass welding characteristics, welding power, and corresponding heat input. HS and HL coupons were joined by heat input of 0.96 and 1.4 kJ/mm respectively. In addition to the welding power differences, the cooling regimes in HL and HS weldments were two- and three-dimensional, respectively. Lower heat input caused an increase in weld metal hardness. The specimens had average values 270 and 250 Vickers with standard deviations 20 and 12 Vickers at FZ in a given order. The relative length of HAZ was also smaller in HS specimen due to lower heat input and higher cooling rate compared to HL specimen. The fusion morphologies were not totally different from each weldment because of the length of the weld-pass intersections in HS weldment.

The average impact toughness of HS and HL at HAZ were measured as 148 J and 126 J with standard deviations 90 and 38 joules due to slower cooling rate in the HL weldments. The grains in CGHAZ of HL specimen were larger compared to HS weldment. The enlarged grains decreased impact toughness averages of HL specimen. On the other hand, multi-pass welding effect in HS caused scatter in the impact toughness results. The standard deviation in corresponding test results was higher in HS specimens. Although the impact toughness results showed that thicker coupon was advantageous for high toughness applications, the further CTOD experiments in 16mm-thick weldments confuted this idea.

105

HL weldments yielded higher toughness than HS weldments when the HAZ specific machined CTOD specimens were compared. Therefore, CTOD experiment results stated that critical crack tip openings in CGHAZ were higher in thinner material, although making a comparison between these results was a fault. The reason for this fault is based on the characteristics of fracture mechanics approaches and that of the CTOD experiment. The CTOD value is not a true material property, and it is a path-dependent experiment. Hence, the critical CTOD values vary in accordance with the material thickness.

In addition to these, plain-stress and plain-strain conditions are important for thickness dependent toughness tests, e.g. CTOD. The fracture mechanism of X70M is described in the elastic-plastic regime. Although the fracture mechanism of the line pipe steel is different from totally plastic materials, the plain-stress and plain-strain phenomena can be seen in Figure 67. The formation of the plastic zone at the crack tips was limited as the material thickness decreases. Therefore, the ductile fracture was seen in the thinner CTOD specimens, and the comparison between thin and thick plates became almost meaningless. The fabrication based allowable imperfections and inhomogeneity were distributed randomly in FZ and HAZ. The dimensions of the imperfections were almost constant in each welding operation. The ratio of imperfections on material thickness in the sub-sized or thinner specimens became higher compared to the full-thickness specimens.
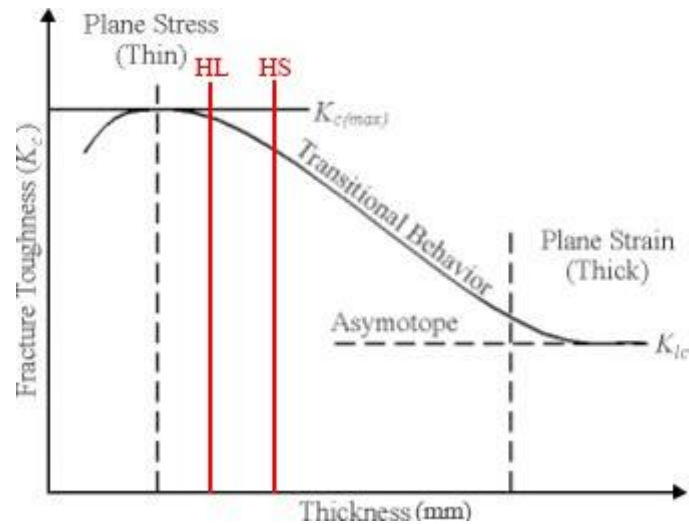
Figure 67. Effect of material thickness on fracture toughness.

The representative load vs. CMOD graphs of HS and HL specimens are given in Figure 68. It is seen that the compressive load on the specimens increases as the specimen thickness increases. The fracture type in the thick material becomes brittle. The full-thickness HS specimens yielded lower toughness due to low heat input and plain-strain condition compared to HL specimens.

The crack plateau analysis and post-test metallography results showed that the effects are not constrained by heat input and material behavior only. The microstructural features observed in FZ and HAZ also affected obtaining lower CTOD values. HS coupons were joined via two-weld pass; local weak points existed in CGHAZ. MA formation was observed in IRCGHAZ, therefore corresponding local brittle zones caused unstable crack growth along grain boundaries (Figure 69). The high amount of metallurgically weakest points were observed in CGHAZ and FGHAZ of 16 mm-thick HS coupons. The hardness variations between these regions and their detrimental effects are explained in Section 4.5.
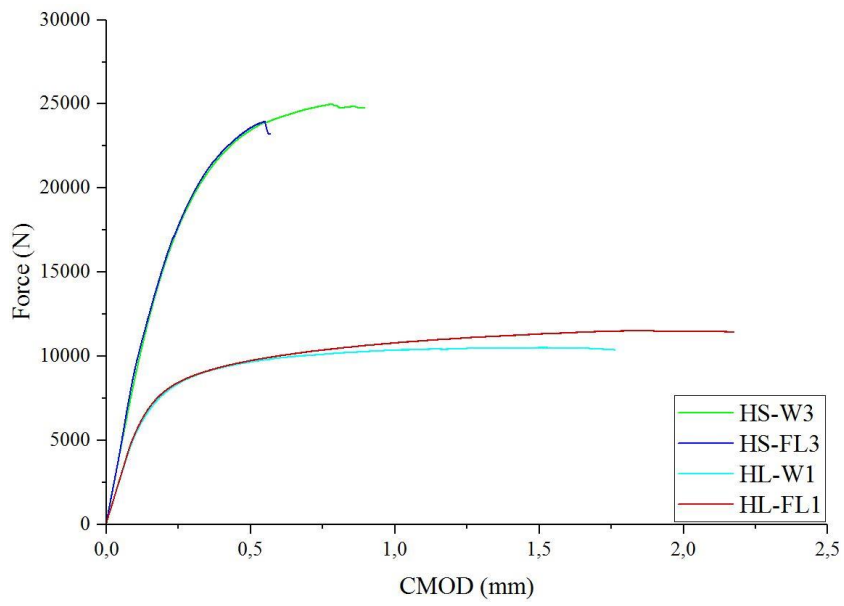
Figure 68. The representative Load vs. CMOD graphs of HS and HL specimens.
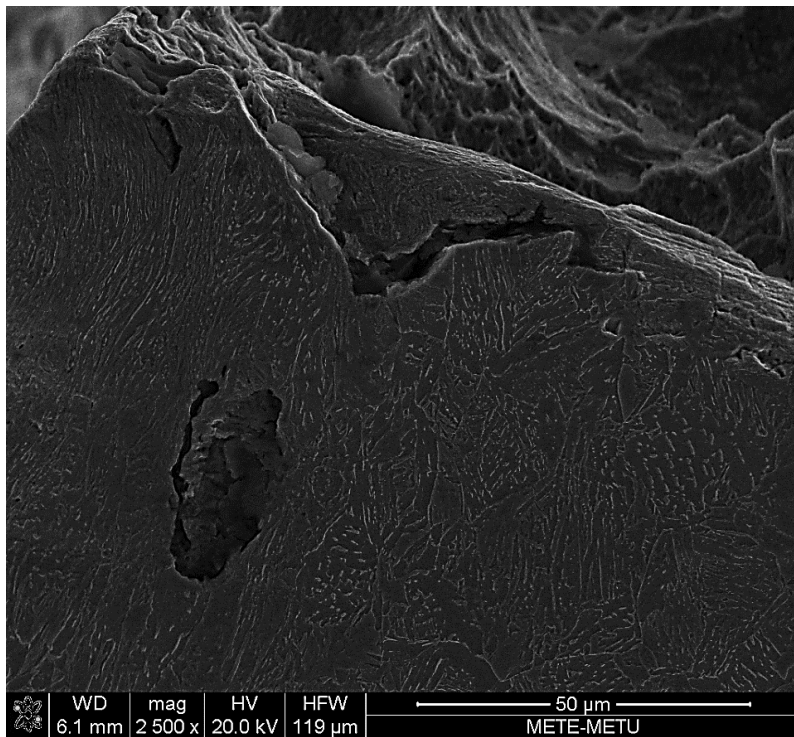
Figure 69. Fractography analysis in HS-FL2 specimen.

4.5. MA Formation

The effects of heat input on microstructure and mechanical properties of material were introduced in previous sections 4.2., 4.3., and 4.4., briefly. The major effect is the formation of LBZs and inclusions through the fusion line and HAZ. The effects were investigated by mechanical tests and metallographic examination via LOM and SEM. The starting point of this investigation is that the X70M grade line pipe steel, 16-19 mm-thick coupons, was fabricated and pipelines were constructed with different welding techniques, in which the heat input was varied in the range of 0.4 and 2.0 kJ/mm. The mechanical properties of the as-welded material are controversially affected if the welding power is chosen without this range. For instance, the formation of MA islands in CG- and IRCG-HAZ is promoted by applying heat input of 2.5 kJ/mm in pipeline fabrication via SAW technique due to the lower cooling rate in SAW compared to GMAW.
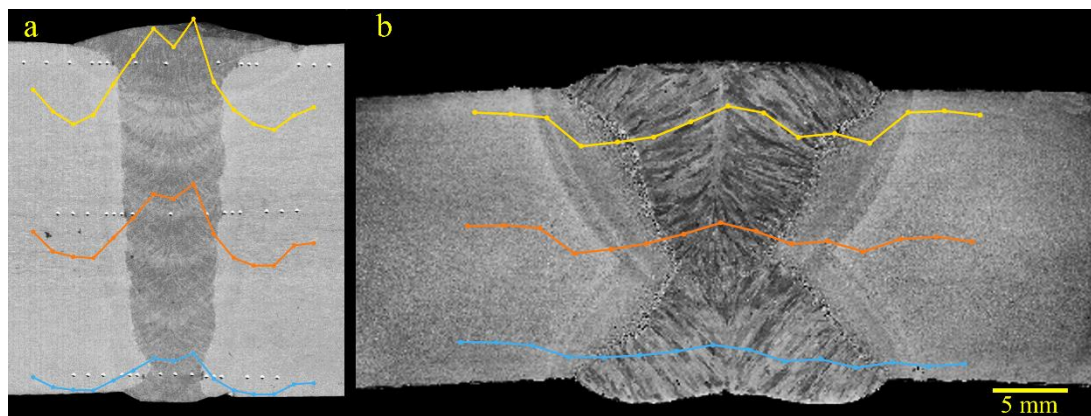
Figure 70. Macro-etch sample of a) GF and b) SF weldments with hardness profiles.

The MA formation is controlled and optimized by applying the heat input of 0.4-0.5 kJ/mm in multi-pass GMA weldments, which is done in the field. It is proved by microstructural observations that the hardness distribution through the fusion line is not varied too much, 240±15 HV (Figure 70). The fusion zone hardness variations, minimum values at the middle of three macro-indent, is due to the equiaxed grain formation (Figure 66). Dendritic arms result relatively higher hardness values due to the solidification characteristic. The toughness tests, both Charpy impact, and

CTOD, conducted on GF weldments reveal that a few number of specimens was subjected to unstable crack growth. In other words, they are fractured without absorbing at least 50 J impact energy. The reasons behind unstable crack propagation are LBZ formation and distribution in IRCGHAZ due to multi-pass welding (Figure 63) and some micro-sized welding imperfections. The local weak points might be promoted due to inaccurate pre-heat or post-weld treatment operations. High inter-pass temperature, i.e. 350-400 °C, and/or inadequate post-weld treatment, which leads to increase in grain size, and decrease in hardness and toughness value through the fusion line of the final weld-pass, might cause poor mechanical properties. The heat input should be controlled and designed according to the specific situations, e.g. ambient temperature in field GMAW operations.

Furthermore, the detrimental effects of high heat input, 2.5-5.0 kJ/mm, was observed in field SA weldments, namely SF specimens. The resulting coarsened grains caused a decrease in hardness and toughness of the as-welded coupons in CGHAZ since the cooling rate is decreased as heat input increases. The lower toughness results were obtained due to coarsened grains and existence of MA constituents at grain boundaries. The high heat input leads to local softening just beyond the fusion line. Average macro-hardness in HAZ of SF weldment is 180±10 HV. This average is lower than the hardness of MA islands. The difference between locally hardened, including MA islands, and softened zones employs a mismatch in the as-welded material. The hardness variations are provided by detailed measurement are given in Figure 76.

In the light of the investigation of the field weldments, welding procedures were conducted in laboratory conditions. The controlled weldments with different parameters revealed the effects of heat input directly. MA islands and LBZs were found in IRCGHAZ of multi-pass GL weldments.

The effect of heat input, 1.0 kJ/mm was determined by microstructural observations (Figure 71) and mechanical tests as

- Increasing size of MA islands,
- Varying shape and distribution of MA islands,
- Increasing relative grain size in CGHAZ,
- Employing similar toughness of as-welded materials.
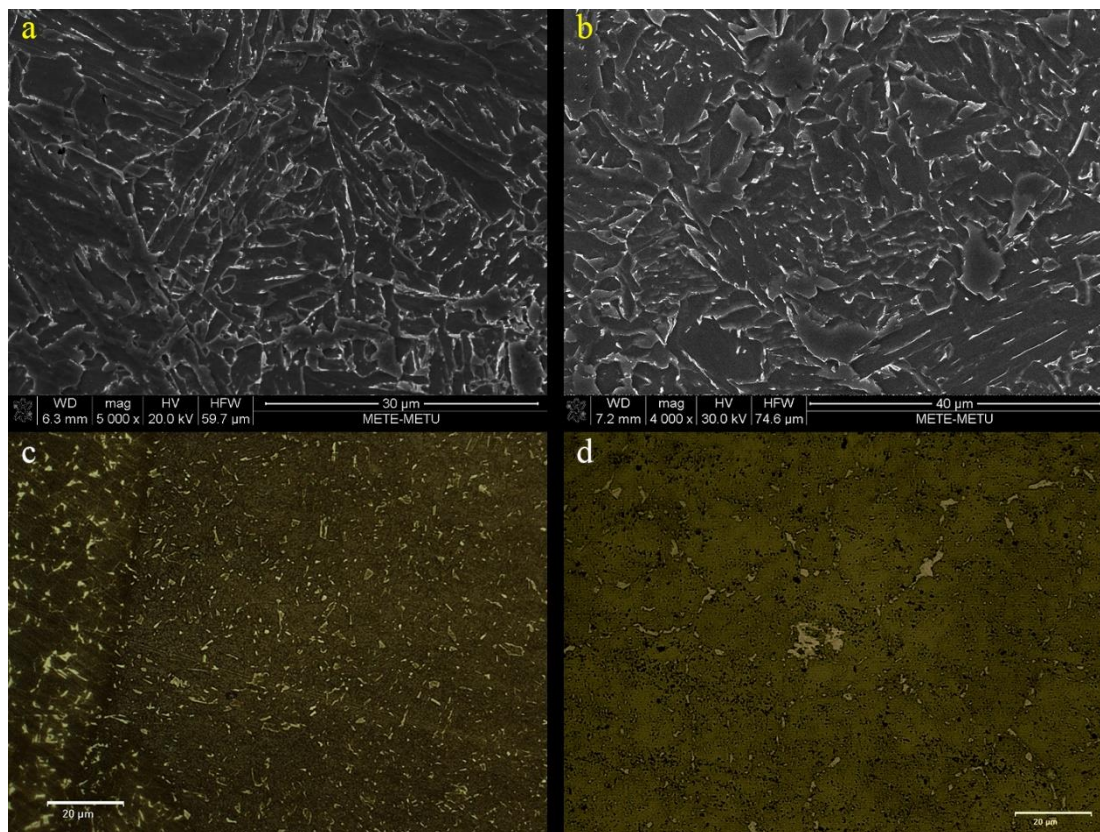
Figure 71. IRCGHAZ microstructures of the GF and GL weldments, column view in a given order. (a and b etched by 2% nital; c and d etched by LaPera).

The controversial effects of heat input, poor mechanical properties, can be eliminated by decreasing it in common SAW applications. The heat input was chosen as 1.78 kJ/mm in SL weldments. The corresponding microstructure of as-welded material seems better in terms of metallurgically weakened points (Figure 72). The amount of MA islands in CG- and IRCG-HAZ is decreased by lowering heat input to 75% of welding parameter applied in field operations. The average grain size in CGHAZ of

SL weldment is reduced by 20% compared to that of SF weldments. The average CTOD values of SL specimens was observed as 0.362 mm with a standard deviation 0.14 mm whereas that of SF specimens was 0.275 mm with a standard deviation 0.11 mm. Therefore, the toughness of SL specimens, in terms of CTOD (mm), becomes better by 30%.
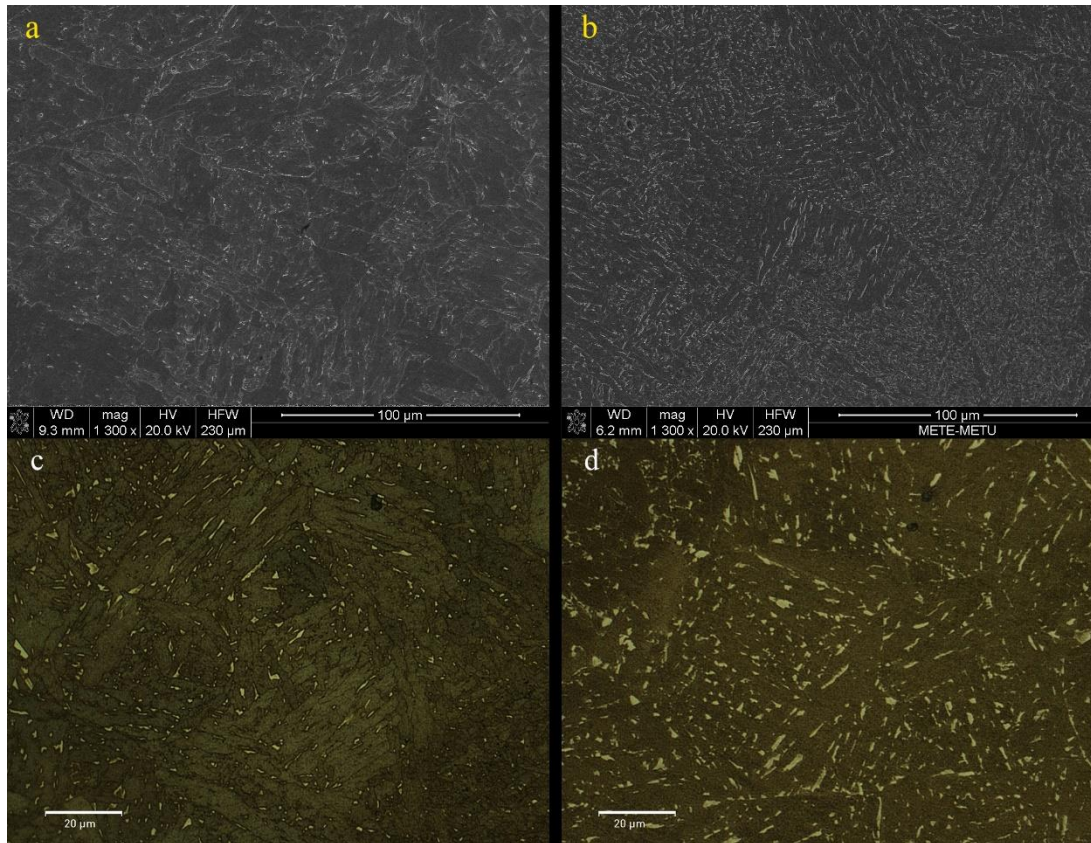
Figure 72. CGHAZ microstructures of the SL and SF weldments, column view in a given order. (a and b etched by 2% nital; c and d etched by LaPera).

Almost 1 kJ/mm was chosen as the heat input for 16 mm-thick HPA weldments, namely HS and HC coupons. The toughness values of HS and HC weldments are relatively lower than other GMA and SA weldments since the heat input could not be sufficient to eliminate undesired morphological formations in HAZ. Reasons behind the poor mechanical properties are LBZ and MA formations and their distribution in IRCGHAZ. The formed brittle zones due to moderate cooling were identified by nano-indentation, which were conducted according to Oliver-Pharr method.

Although average hardness values of HS and HC weldments in CGHAZ are 340±55 and 400±70 HVIT (Vickers), respectively, the average hardness values of MA islands is 590±75 HVIT (Vickers). The hardness distribution through the fusion lines of these weldments and corresponding Load vs. Indentation depth graphs are given in Figure 73 and Figure 74.
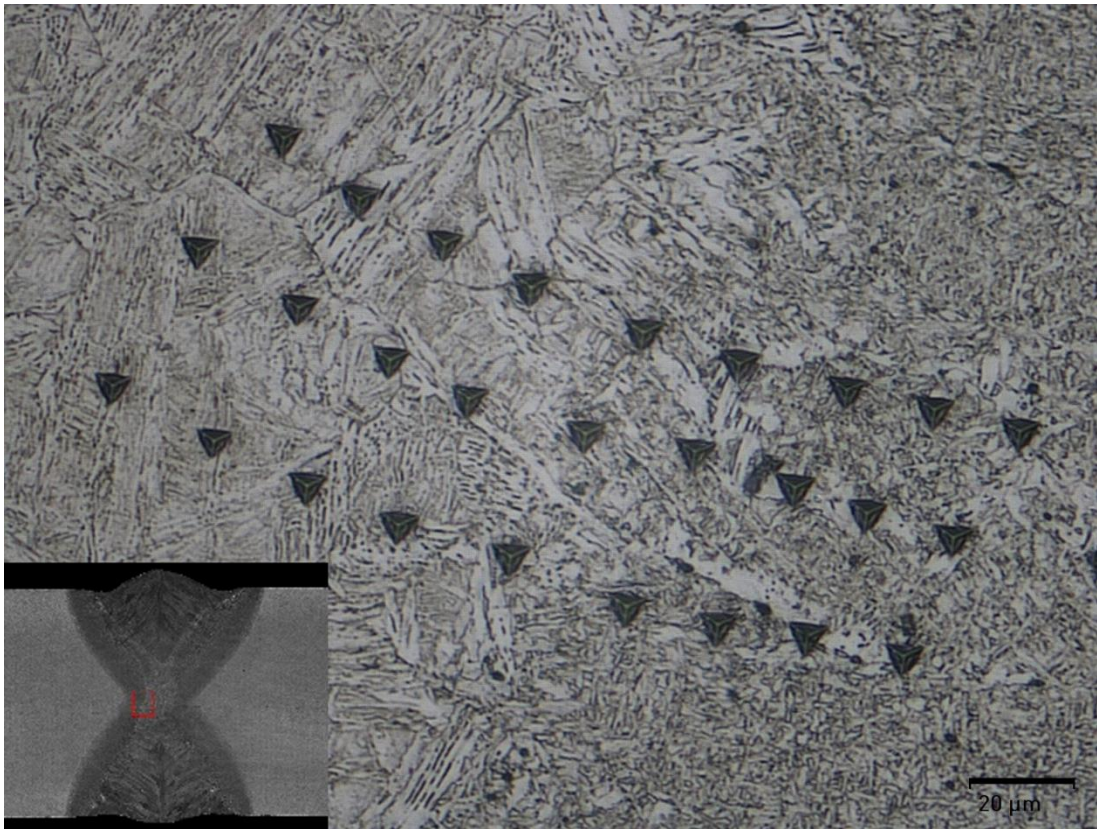
Figure 73. Nano-indentation distribution of HC weldment.
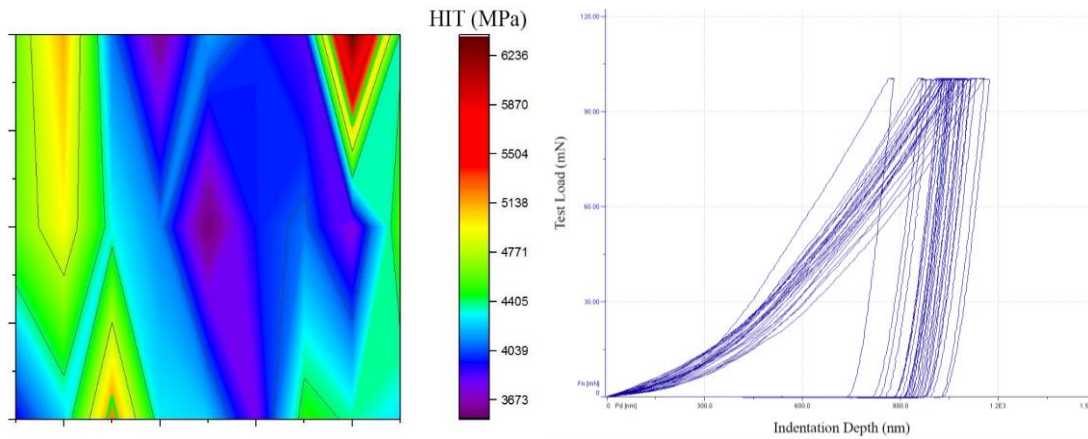
Figure 74. Hardness distribution in FZ and HAZ (marked region in Figure 73), and test load vs. indentation depth graphs of HC weldment.

The load vs. indent depth graph showed that various morphologies have different surface characteristics, which might also be affected by etching during specimen preparation and oxidizing before nano-indentation tests. The etching effect was minimized by homogeneous etching via mechanical apparatus. The oxidation problem on the surfaces was eliminated by transferring specimens in a closed container, including free silica particles. Thus, only phase variations were examined, and MA formations were located in IRCGHAZ as observed in micrographs (Figure 75), which were prepared by LaPera reagent.

MA constituents were localized at grain boundaries in both HS and HC weldments. Therefore, the cracks were propagated along grain boundaries and intergranular fracture was observed (Figure 69). The amount of them is higher in HC weldment, due to the slightly higher heat input, compared to HS weldment. The morphological differences are also observed in IRCGHAZ of these weldments. MA constituents is formed in triangle, quadrangle, and stringer shapes. The stringer type MA caused a slight decrease in toughness values.

114
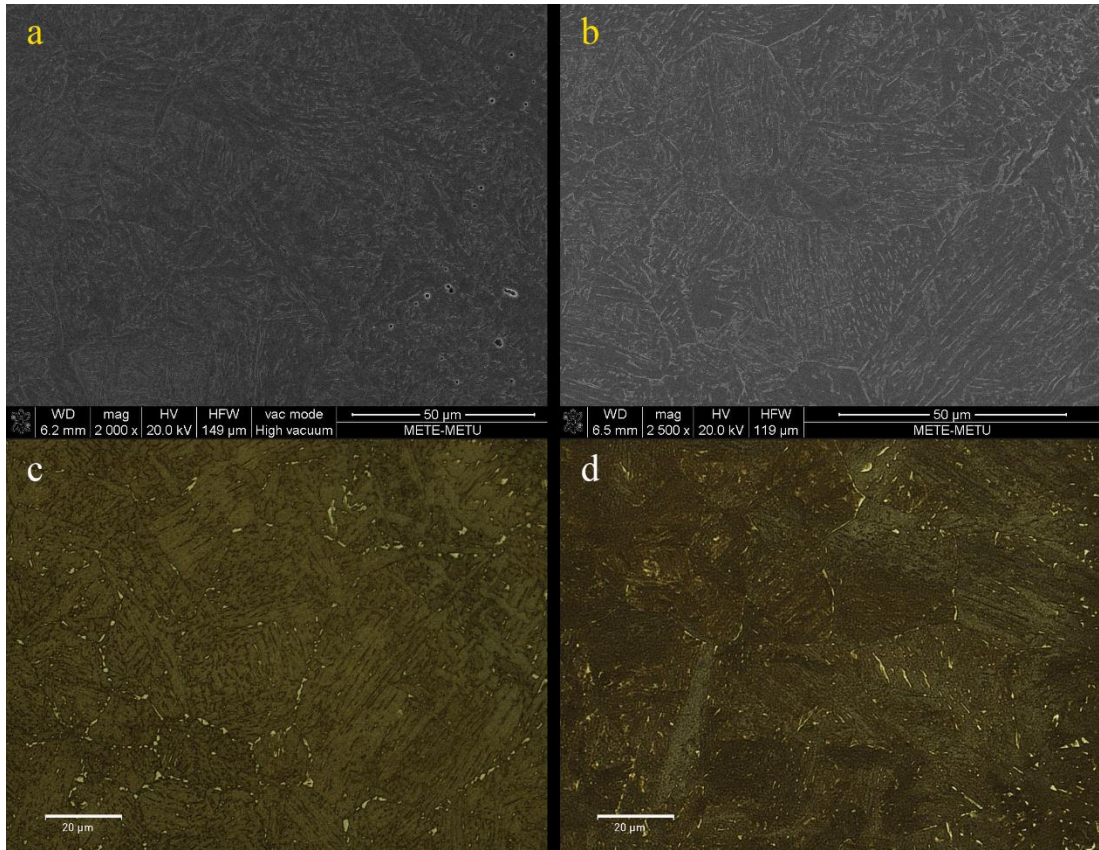
Figure 75. IRCGHAZ microstructures of the HS and HC weldments, column view in a given order. (a and b etched by 2% nital; c and d etched by LaPera).

Impact Toughness

Impact toughness of materials can be measured by Charpy impact, Izod impact and drop-weight tests. In this work, the most common Charpy impact tests were conducted in accordance with ASTM E23 [60]. In addition to given experimental observations, Impact energies of the specimens at different temperatures are shown in Figure 53.

The Charpy–V-Notch specimens, i.e. FL and mid-FZ of each weldment, were tested at -10 °C. The results are given in Figure 76 and Figure 77. Although the fusion line impact toughness values of the HPA weldments yielded high scatter, they were greater than those of the fusion zone and the weld metal of the same weldments. SA

weldments had better impact toughness characteristics compared to GMA and HPA weldments because of high compatibility between the material and flux/wire in terms of mechanical properties.
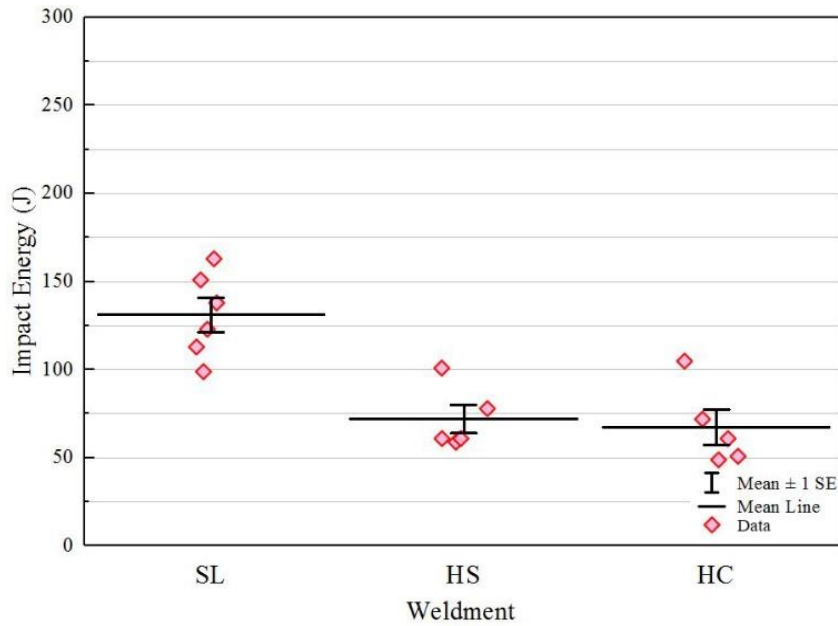
Figure 76. Impact energy distributions in FZ of SL, HS and HC specimens.
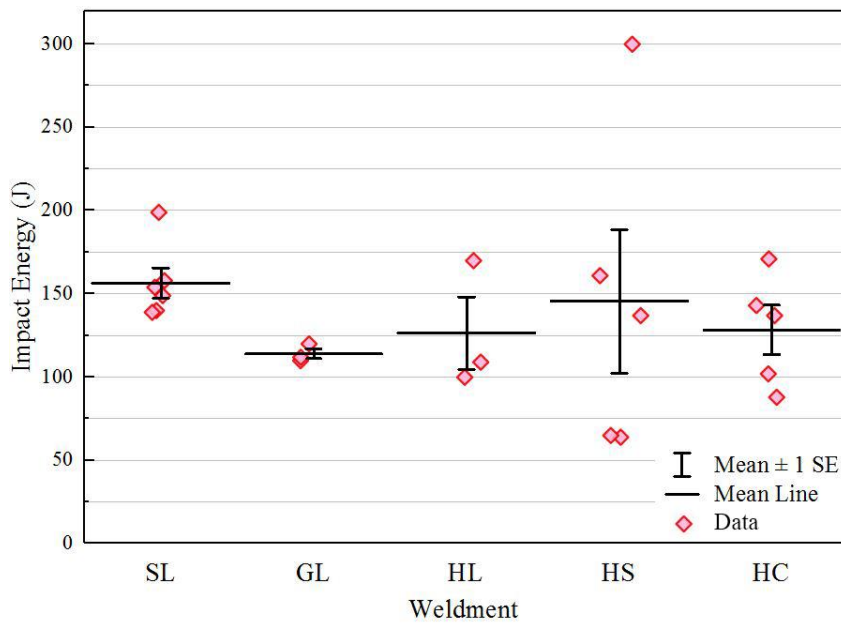
Figure 77. Impact energy distribution in HAZ of SL, GL, HL, HS and HC specimens.

Crack tip opening displacement

The sets of specimens, which had a different number of specimens to obtain representative and statistical results, were tested in accordance with ISO 12135 [61]. The samples prepared by wire-cut electric discharge machining were subjected to fatigue pre-crack operation using the following parameters; stress ratio (R) 0.1, loading frequencies of 40 Hz, 34 Hz and 30 Hz for the 10/20, 15/30 and 17/34 coded specimens, respectively.

The load vs. CMOD graphs for each welding method are given in Figure 78.
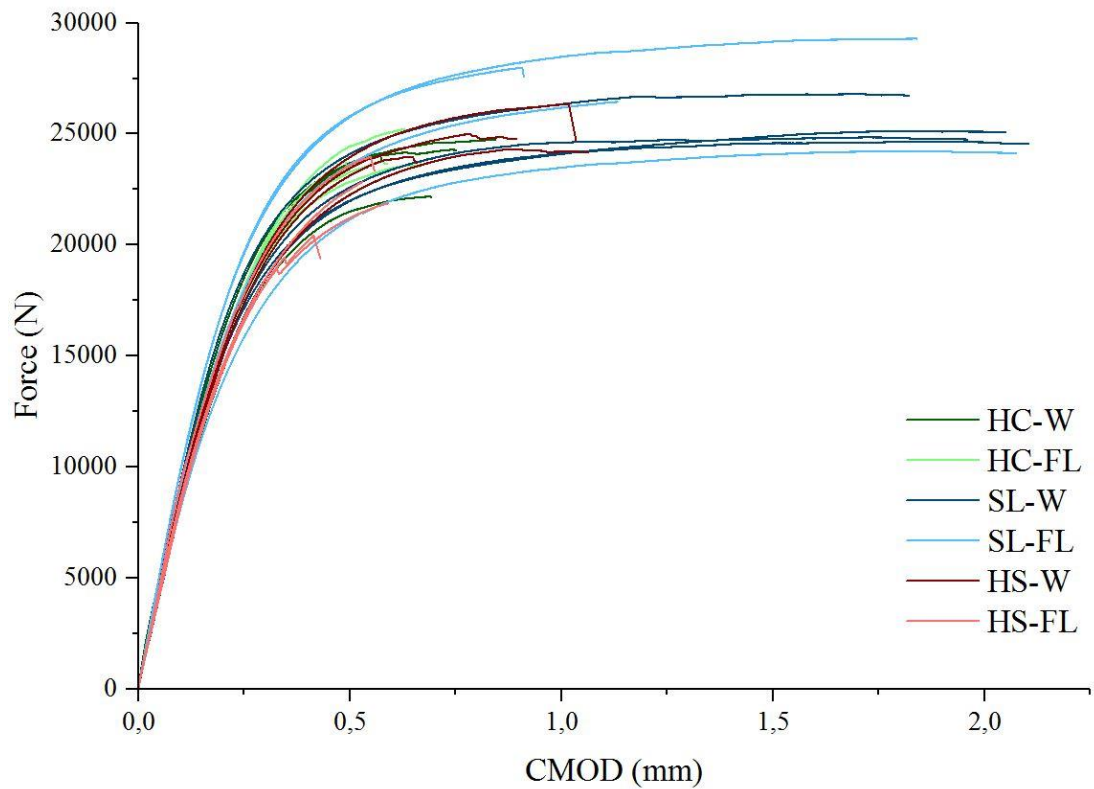
Figure 78. Load vs. CMOD graphs of HS, HC and HL coded CTOD specimens.

The cracks were measured digitally by using ImageJ software [82]. Fractured surface images were calibrated via real caliper and micrometer measurements in accordance

117

with the related standards. The representative surface photographs for each crack growth, unstable and stable, can be seen in Figure 79a and Figure 79b respectively.
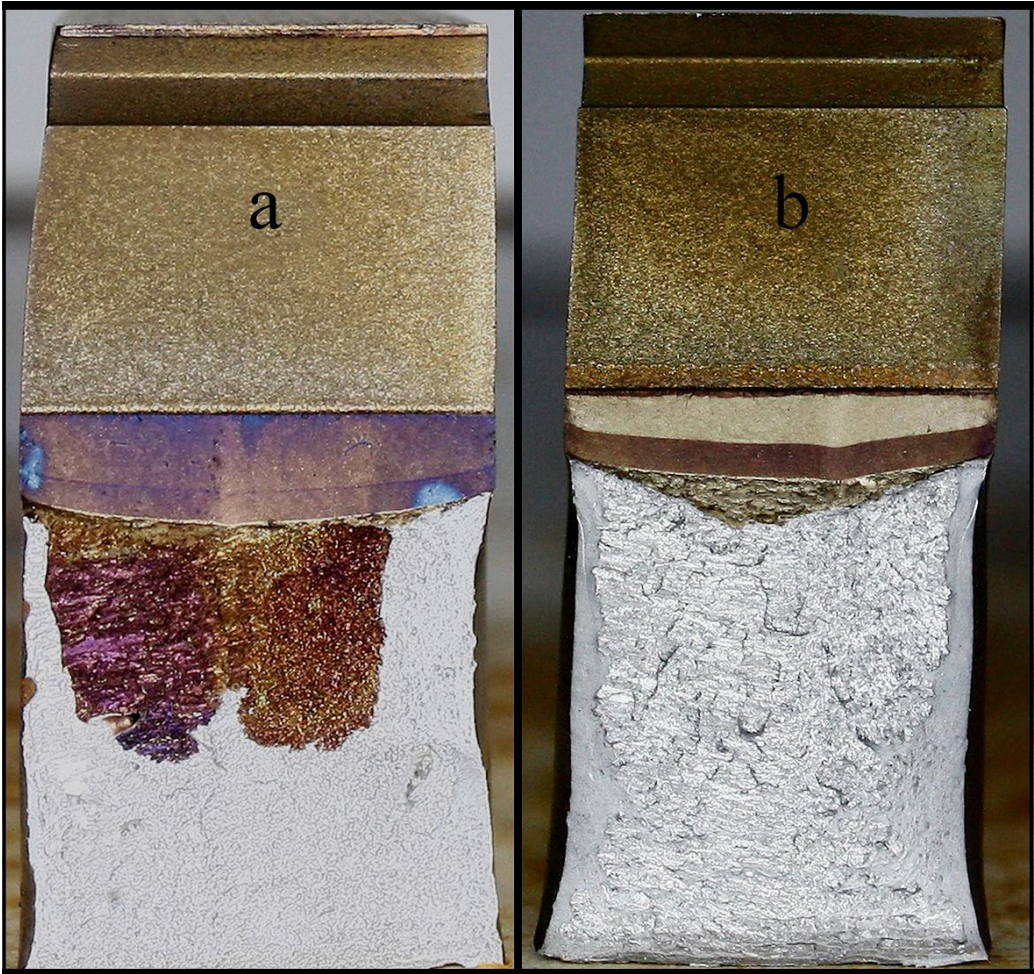
Figure 79. Fracture surface photographs of the weldments: a) HS and b) SL.

The notch locations were also checked. The metallographically prepared pieces were investigated under LOM, and the notch locations passing through the CG HAZ were verified. The representative ones are given in Figure 80.
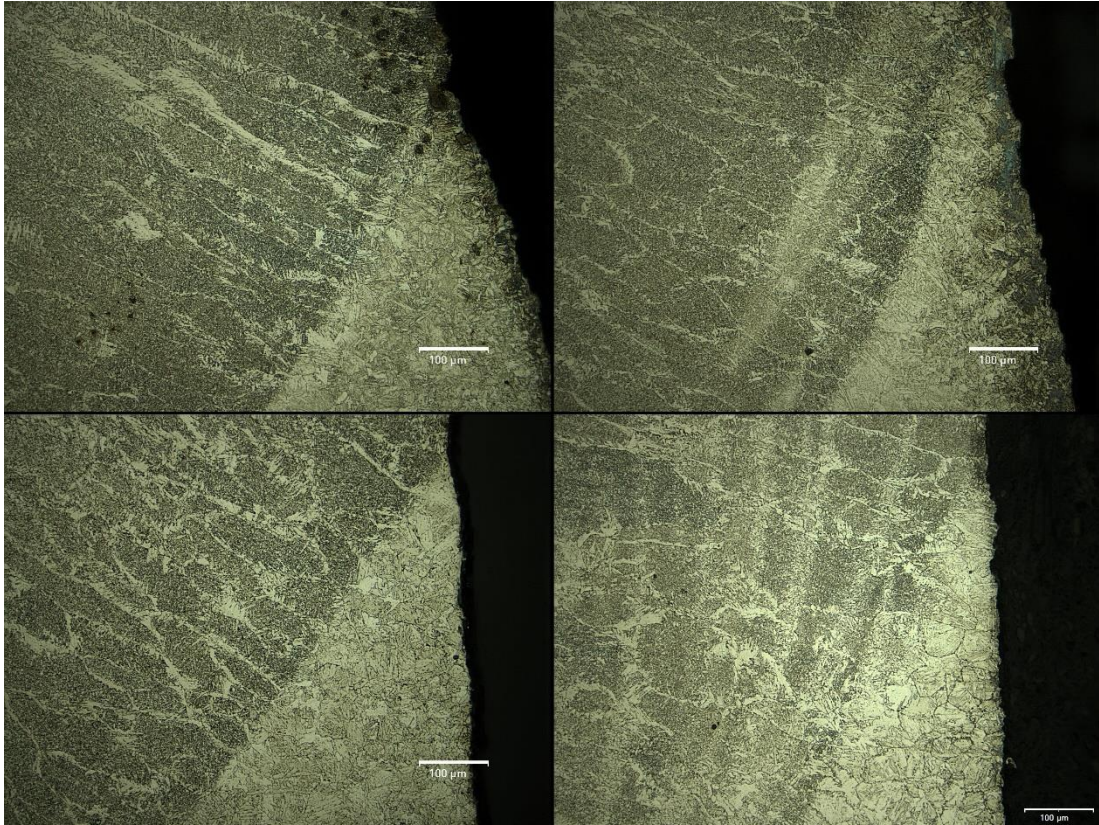
Figure 80. Post-test images of the fusion lines in the CTOD specimens: a) SL, b) HC, c) and d) HS.

As it is mentioned previously, the original microstructure of the parent metal alters due to the heat introduced during welding operations and new primary and secondary phases are formed, as well as grain coarsening. After nucleation on the most potent austenite grain boundaries, bainitic-ferrite laths develop rapidly across the whole Parent grain before nucleation sites on other austenite grain boundaries become potent enough. However, for the larger austenite grains, before the initially nucleated bainitic-ferrite laths expand across the complete austenite grain, other austenite grain boundaries become potent enough, and there is still enough volume of austenite left for the development of these nuclei. The continuous cooled microstructure with different prior austenite grain sizes varying from about 35-40 µm for HAZ of HPA weldments to more than 80 µm for HAZ of SA weldments. It can be seen form the

119

EBSD maps, the effective grain size of the transformed bainitic-ferrite microstructure is larger in HPA weldments than in SA weldments.

As schematically show in Figure 81 the post-transformation carbon content of the BF tends to be significantly higher than the equilibrium concentration, so there are carbon enriched regions around BF laths. However, it was expected weight fraction of the carbon and other austenite promoting elements should be lower in retained austenite during low heat input welding operations than high heat input welding operations due to different cooling rates. That yields MA constituents with higher hardness in SA weldments. Reheating the HAZ, the MA constituents tend to agglomerate and form blocky islands in the grains and along the grain boundaries, which is called LBZs. In other words, cooling rate, consequently, the heat input of the process should be limited during welding operations. Heat inputs more than 2 kJ/mm and less than 1.0 kJ/mm without pre-heating results in local softening and brittle zones in CGHAZ.

In one hand, high heat input processes yield small effective grain size, which is thought to be good for fracture toughness of the material, on the other hand, they also yield MA constituents with high hardness. Contrary to high heat input processes, low heat input ones yield large effective grain size but MA constituents have apparently lower hardness. The outputs of microstructural observations are similar to the results obtained by Zhao et al.
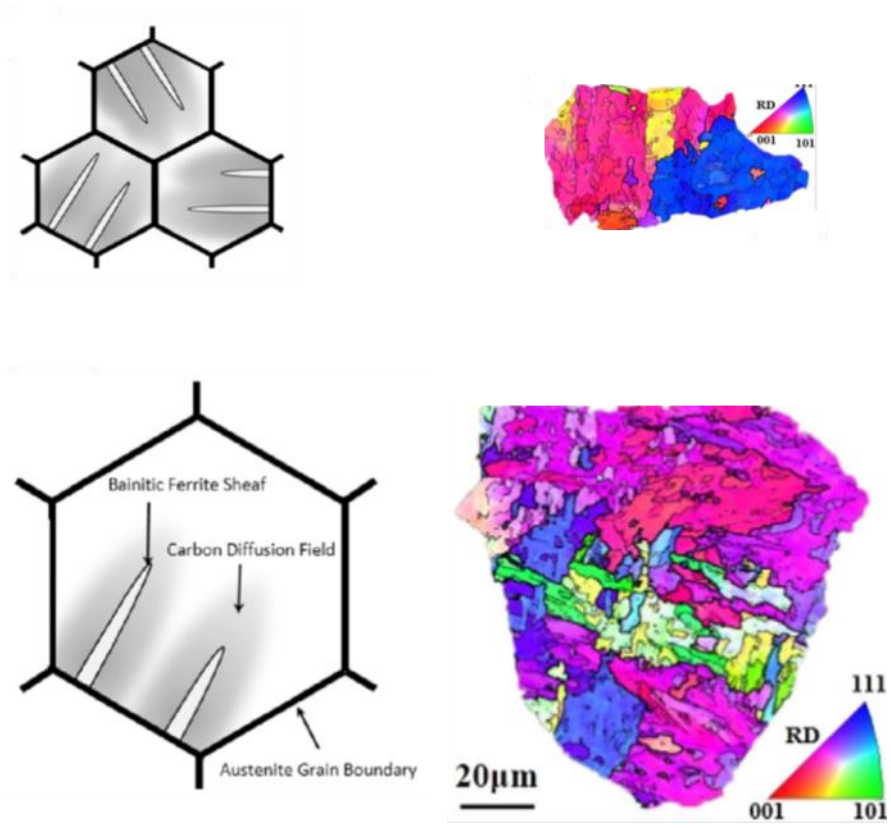
Figure 81. Representation of BF lath formation and corresponding EBSD graphs [83].

CHAPTER 5

CONCLUSION

The key-hole weldability of line pipe steel grade X70M was investigated in terms of fracture toughness, employing the hybrid plasma arc welding (HPAW) process. Conventional Gas metal and submerged arc welding techniques were practiced for benchmarking. Classical structural integrity assessment examinations were done before microstructural and mechanical characterization parts. The welding parameters were optimized to obtain the desired microstructure and mechanical properties. The following conclusions can be drawn from this study:

- Multi-pass welding causes the formation of the local weakest point in HAZ, which controversially affects the mechanical properties.

- The distribution of the local weakest points directly affect the mechanical properties. If they are localized at specific regions, i.e. grain boundaries in IRCGHAZ, material toughness decreases dramatically. Thus, homogeneous distribution of MA constituents in HAZ is required for better material toughness.

- Single-pass HPAW yields comparable results with multi-pass GMAW in terms of CTOD values. Advantages of the HPAW method, i.e. low operational cost, makes it a strong alternative to the conventional welding methods.

- Double-sided HPA weldments have lower toughness compared to double-sided SA weldments due to the challenging during fabrication and microstructural evolutions in HAZ. The amount and distribution of MA islands affect the mechanical properties, i.e. toughness, negatively and

123

created local weak points for crack formation. The hardened regions promote unstable crack propagation.

- Heat input variations detrimentally affect microstructural features and mechanical properties of as-welded materials. X70M weldments should be completed within the range of 0.5 and 2.0 kJ/mm heat input. Heat input values outside this range cause a decrease in material toughness.

- Effective grain size and hardness of MA constituents were observed to be conflicting with respect to amount of the heat introduced by welding processes. An optimum heat input would provide reasonably fine grains with MA constituents that are not cause embrittlement to the material. This combination definitely gives the highest possible fracture toughness for an as-welded material.

- Employing HPAW provided more information about not only effect of LBZ but also the controversial effect of weld heat input on microstructure and toughness of the weld heat affected zone of microalloyed and TM processed HSLA steels.

- Key-hole based HPAW cannot be used in pipe fabrication due to operational difficulties. SAW, the main method for pipe fabrication, yields better mechanical properties compared to HPAW.

Recommendations for future works:

- The difficulties of HPAW should be analyzed in detail. The reasons and possible outcomes can be classified according to the welding parameters. The negative effects should be eliminated or minimized to use this method in the field due to its advantages in terms of welding consumables and operational cost.

- The effect of residual stress on fracture toughness and crack propagation should be investigated.

- The welding techniques; SAW, GMAW, and HPAW should be used to have engineering critical assessment purposes. The additional tests can be conducted with the parameters used in this thesis.

REFERENCES

1. Yurtışık, K., *Kinetics and Microstructural Analysis of Fatigue Fracture Progress in Weld Joints of Duplex Stainless Steel Grade 2205*, in *Metallurgical and Materials Engineering*. 2013, Middle East Technical University.

2. Kim, B.C., *Microstructure and local brittle zone phenomena in high-strength low-alloy steel welds.* Metallurgical Transactions A, 1991. 22: p. 139-149.

3. Toyoda, M., *Crack Tip Opening Displacement (CTOD) Testing Method for Heat-Affected Zone (HAZ) Toughness of Steel Welds with Particular Reference to Local Inhomogeneity.* American Society for Testing and Materials, 1994: p. 291-307.

4. Zhu, Z., Materials Transactions B, 2014. 45B: p. 229-235.

5. American Petroleum Institute, *API 5L Specification for Line Pipe*. July1, 2013, API Publishing Services: 1220 L Street, NW, Washington, DC 20005.

6. Sharma, S.K. and Maheshwari, S., *A review on welding of high strength oil and gas pipeline steels.* Journal of Natural Gas Science and Engineering, 2017. 38: p. 203-217.

7. Zhao, M. C., *Acicular ferrite formation in a pipeline steel with thermo-mechanical control process.* Acta Metallurgica Sinica, 2001. 37.

8. Llewellyn, R.H.D., *Low-carbon Structural Steels*. 3rd ed. Steels: Metallurgy and Applications. 1998: Butterworth-Heinemann.

9. Shin, S., *Correlation of microstructure and charpy impact properties in API X70 and X80 line-pipe steels.* Materials Science and Engineering A, 2007. 458: p. 281-289.

10. Godefroid, L.B., *Microstructure and Mechanical Properties of Two API Steels for Iron Ore Pipelines.* Materials Research, 2014: p. 114-120.

11. Rosado, D.B., *Latest developments in mechanical properties and metallurgical features of high strength line pipe steels.* Sustainable Construction and Design, 2013. 4(1).

12. Hashemi, S., *On the relation of microstructure and impact toughness characteristics of DSAW steel of grade API X70.* Fatigue & Fracture of Engineering Materials & Structures, 2009. 32: p. 33-40.

13. Khalaj, G., *Artificial neural networks application to predict the ultimate tensile strength of X70 pipeline steels.* Neural Comput & Applic, 2013. 23: p. 2301-2308.

14. Kim, Y.M., *Effects of Molybdenum and Vanadium Addition on Tensile and Charpy Impact Properties of API X70 Linepipe Steels.* Metallurgical and Materials Transactions A, 2007. 38: p. 1731-1742.

15. ASM International, *High-Strength Low-Alloy Steels.* 2001, ASM International.

16. Krauss, G. and Thompson, S., *Ferritic microstructures in continuously cooled low- and ultra-low carbon steels.* Iron and Steel Industry of Japan International, 1995. 35: p. 937-945.

17. Shanmugam, S., Misra, R., and Hartmann, J. , *Microstructure of high strength niobium-containing pipeline steel.* Materials Science and Engineering A, 2006. 441: p. 215-229.

18. Mohtadi-Bonab, M.A., Szpunar, J.A., and Razavi-Tousi, S.S., *A comparative study of hydrogen induced cracking behavior in API 5L X60 and X70 pipeline steels.* Engineering Failure Analysis, 2013. 33: p. 163-175.

19. Carneiro, R., Ratnapuli, R., and Lins, V., *The influence of chemical composition and microstructure of API linepipe steels on hydrogen induced cracking and sulfide stress corrosion cracking.* Materials Science and Engineering A, 2003. 357(1-2): p. 104-110.

20. Sente Software Ltd., *JMatPro the Materials Property Simulation Package.* UNITED-KINGDOM.

21. Mills, K. C., *Marangoni effects in welding.* Philosophical Transactions of The Royal Society A, 1998. 356: p. 911-925.

22. Lu, S., Fujii, H., and Nogi, K., *Marangoni convection and gas tungsten arc weld shape variations on pure iron plates.* The Iron and Steel Institute of Japan International, 2006. 46: p. 276-280.

23. Heiple, C. R., and Roper, J. R., *Mechanism of minor element effect on GTA fusion zone geometry.* Welding Journal, 1982. 61: p. 7-102.

24. Nicholas, J. M., and Abson, D. J., *The prediction of maximum HAZ hardness in various regions of multiple pass welds*, in *17th International Conference 'Computer Technology in Welding and Engineering*. 2008: University of Cranfield.

25. Eroglu, M., and Aksoy, M., *Effect of initial grain size on microstructure and toughness of intercritical heat-affected zone of a low carbon steel.* Materials Science and Engineering A - Structural Materials Properties Microstructure and Processing, 2000. 286(2): p. 289-297.

26. Li, Y., *The Effect of Vanadium and Niobium on the Properties and Microstructure of the Intercritically Reheated Coarse Grained Heat Affected Zone in Low Carbon Microalloyed Steels.* ISIJ International, 2001. 41(1): p. 46-55.

27. Haughton, F., *Automatic arc-welding machine*, U.S.P.a.T. Office, Editor. 1928: USA.

28. GSI SLV Duisburg, *The Welding Engineer's Current Knowledge*. 2009.

29. ESAB, *Submerged Arc Welding*. 2008.

30. Kim, Y. S., and Eagar, T., *Analysis of Metal Transfer in Gas Metal Arc Welding.* Welding Journal, 1993: p. 269-278.

31. *Gas metal arc welding*. N.D.

32. Semenov, O., *A dynamic model of droplet formation GMA welding.* Modelling and Simulation in Materials Science and Engineering, 2012. 40(4): p. 1-14.

33. Eckert, E., and Pfender, E., *Plasma Energy Transfer to a Surface With and Without Electric Current.* Welding Journal, 1967. 46(10): p. 471-479.

34. Ludwig, H., *Plasma-Energy Transfer in Gas-Shield Welding Arcs.* Welding Journal, 1959. 38(7): p. 296-300.

35. Tomsic, M., and Jackson, C., *Energy Distribution in Keyhole Mode Plasma Arc Welds.* Welding Journal, 1974(March): p. 109-115.

36. Ayrton, H., *The Electric Arc*. 1902, London: The Electrician.

37.   Assuncao, E., Williams, S., and Yapp, D., *Interaction time and beam diameter effects on the conduction mode limit.* Optics and Lasers in Engineering, 2012. 50: p. 823-828.

38.   Dupont, J. N., and Marder, A. R., *Thermal Efficiency of Arc Welding Processes.* Welding Journal, 1995. 74: p. 406-416.

39.   Fuerschbach, B. W., and Knorovsky, G. A., *A Study of Melting Efficiency in Plasma Arc and Gas Tungsten Arc Welding.* Welding Journal, 1991. 70: p. 287-297.

40.   Smartt, H. B., Stewart, J. A., and Einerson, C. J., *Heat Transfer in Gas Tungsten Arc Welding*, in *ASM ınternational Welding Congress*. 1985: Toronto, Canada.

41.   Okada, A., *Application of Melting Efficiency and its Problems.* Journal of Japan Welding Society, 1977. 46: p. 53-61.

42.   Collings, N., Wong, K. Y., and Guile, A. E., *Efficiency of Tungsten-Inert Gas Arcs in Very High Speed Welding.* Proceedings of the Institution of Electrical Engineers, 1979. 126: p. 276-280.

43.   Dykhno, I., and Ignatchenko, G., *MIG-plasma welding*, U.S.P.a.T. Office, Editor. 2007.

44.   Okan, K., *An Investigation on Fatigue Crack Propagation in Gas Metal and Hybrid Plasma-Gas Metal Arc Weldments of AA5083-H111*, in *Metallurgical and Materials Engineering*. 2015, Middle East Technical University: Ankara.

45.   Tolungüç, B., *Microstructural and Mechanical Characterization of Duplex Stainless Steel Grade 2205 Joined by Hybrid Plasma and Gas Metal Arc Welding*, in *Metallurgical and Materials Engineering*. 2012, Middle East Technical University: Ankara.

46.   Yurtisik, K., et al., *Characterization of Duplex Stainless Steel Weld Metals Obtained by Hybrid Plasma-Gas Metal Arc Welding.* Soldagem & Inspeção, 2013. 18(3).

47.   Yurtisik, K. and Tirkes, S., *Fatigue Cracking of Hybrid Plasma Gas Metal Arc Welded 2205 Duplex Stainless Steel.* Materials Testing, 2014. 56(10): p. 800-805.

48. Zhu, X. and Joyce, J.A., *Review of fracture toughness (G, K, J, CTOD, CTOA) testing and standardization.* Engineering Fracture Mechanics, 2012. 85: p. 1-46.

49. Wells, A.A., *Application of fracture mechanics at and beyond general yielding.* Br Weld Journal, 1963. 563-570.

50. Dugdale, D.S., *Yielding of steel sheets containing slits.* J Mech Phys Solids, 1960. 8: p. 100-108.

51. American Petroleum Institute, *API 1104 Welding of Pipelines and Related Facilities*. November 2005, API Publishing Services: 1220 L Street, N.W., Washington, D.C. 20005.

52. ASTM International, *Standard Practice for Computed Radiography*. 2010, ASTM International: United States.

53. ASTM International, *Standard Practice for Radiographic Examination*. 2012, ASTM International: United States.

54. The American Society of Mechanical Engineers, *Welding, Brazing, and Fusing Qualifications*, in *BPVC Section IX*. 2015.

55. The International Organization for Standardization, *Destructive tests on welds in metallic materials* in *Bend tests*. 2009, The International Organization for Standardization: Switzerland.

56. The International Organization for Standardization, *Destructive tests on welds in metallic materials -- Transverse tensile test*. 2012: Switzerland.

57. The International Organization for Standardization, *ISO 17639 - Destructive tests on welds in metallic materials — Macroscopic and microscopic examination of welds*. 2003, The International Organization for Standardization: Switzerland.

58. The International Organization for Standardization, *ISO 6507-1 - Metallic materials — Vickers hardness test — Part 1: Test method*. 2005, The International Organization for Standardization: Switzerland.

59. The International Organization for Standardization, *Metallic materials — Tensile testing*, in *Part 1: Method of test at room temperature*. 2009, The International Organization for Standardization: Switzerland.

60. ASTM International, *Standard Test Methods for Notched Bar Impact Testing of Metallic Materials*. 2012, ASTM International: United States.

61. The International Organization for Standardization, *Metallic materials in Unified method of test for the determination of quasistatic fracture toughness*. 2015, The International Organization for Standardization: Switzerland.

62. The International Organization for Standardization, *Metallic materials in Method of test for the determination of quasistatic fracture toughness of welds*. 2010, The International Organization for Standardization: Switzerland.

63. ASTM International, *Standard Test Methods for Determining Average Grain Size*. 2013, ASTM International: United States.

64. ASTM International, *Standard Guide for Quantitative Analysis by Energy-Dispersive Spectroscopy*. 2012, ASTM International: United States.

65. The International Organization for Standardization, *Welding -- Fusion-welded joints in steel, nickel, titanium and their alloys (beam welding excluded) -- Quality levels for imperfections*. 2014, The International Organization for Standardization: Switzerland.

66. European Standards, *Hot rolled products of structural steels. General technical delivery conditions*. 2004.

67. Shao, Q., *Multi-objective optimization of gas metal arc welding parameters and sequences for low-carbon steel (Q345D) T-joints.* Journal of Iron and Steel Research, 2017. 24(5): p. 544-555.

68. Saha, A. and Mondal, S.C., *Multi-objective optimization of manual metal arc welding process parameters for nano-structured hardfacing material using hybrid approach.* Measurement, 2017. 102: p. 80-89.

69. Longchao, C., *Optimization of processing parameters of AISI 316L Laser welding influenced by external magnetic field combining RBFNN and GA.* Results in Physics, 2017. 7: p. 1329-1338.

70. Ragavendran, M., Chandrasekhnar, N., and Ravikumar, R., *Optimization of hybrid Laser-TIG welding of 316LN steel using response surface methodology (RSM).* Optics and Lasers in Engineering, 2017. 94: p. 27-36.

71.   Shanmugarajan, B., *Optimization of Laser welding parameters for welding of P92 material using Taguchi based grey relational analysis.* Defense Technology, 2016. 12(4): p. 343-350.

72.   Sahu, P.K. and Pal, S., *Multi-response optimization of process parameters in friction stir welded AM20 magnesium alloy by Taguchi based grey relational analysis.* Journal of Magnesium and Alloys, 2015. 3(1): p. 36-46.

73.   Srirangan, A.K. and Paulraj, S., *Multi-response optimization of process parameters for TIG welding of Incoloy 800HT by Taguchi grey relational analysis.* Engineering Science and Technology, 2016. 19(2): p. 811-817.

74.   Ghosh, N., Pal, P.K., and Nandi, G., *Parametric optimization of MIG welding on 316L Austenitic Stainless Steel by Grey-based Taguchi Method.* Procedia Technology, 2016. 25: p. 1038-1048.

75.   Scutelnicu, E., *Prediction of Cooling Rate in API-5L-X70 Steel Plates welded by Submerged Double-Arc Welding*, in *1st International Conference on Industrial and Manufacturing Technologies*. 2013: Athens, Greece.

76.   Kou, S., *Welding Metallurgy*. Second ed. 2003, New Jersey: John Wiley & Sons, Inc.

77.   Zhixiong, Z., *Effect of inter-critically reheating temperature on microstructure and properties of simulated inter-critically reheated coarse grained heat affected zone in X70 steel.* Materials Science & Engineering A, 2014. 605: p. 8-13.

78.   Funderburk, R. S., *A look at heat input.* Welding Innovation, 1999. 16(1).

79.   Konohira, T., *What Is Heat Input, and How Does It Affect the Quality of Welds?* . Kobelco Welding Today, 2000. 3(4).

80.   Devletian, J. and Wood, W., *Chapter 1-Weld Solidification*, in *Weld Integrity and Performance*. 1997, ASM International.

81.   Fairchild, D.P., *Fracture Toughness Testing of Weld Heat-Affected Zones in Structural Steel.* Fatigue and Fracture Testing of Weldments, 1990: p. 117-141.

82.   The National Institutes of Health, *Image J*. 2014.

83.   Zhao, H., Wynne, B.P., and Palmiere, E.J., *Effect of austenite grain size on the bainitic ferrite morphology and grain refinement of a pipeline steel after continuous cooling.* Materials Characterization, 2017. 123: p. 128-136.